Title	Molecular Dynamics Simulation of SiO2 and SiN Etching for 3D NAND Memory Device Applications
Author(s)	Cagomoc, Donato Charisse Marie
Citation	大阪大学, 2023, 博士論文
Version Type	VoR
URL	https://doi.org/10.18910/91922
rights	
Note	

The University of Osaka Institutional Knowledge Archive : OUKA

https://ir.library.osaka-u.ac.jp/

The University of Osaka

Doctoral Dissertation

Molecular Dynamics Simulation of SiO_2 and SiN Etching for 3D NAND Memory Device Applications

Charisse Marie Donato Cagomoc

December 2022

Applied and Engineering Physics
Division of Precision Engineering and Applied Physics
Graduate School of Engineering
OSAKA UNIVERSITY

Acknowledgments

I would like to acknowledge all of the people who had been instrumental in my journey to obtain my Ph.D. degree.

I give my sincere gratitude to Professor Satoshi Hamaguchi for accepting me in his laboratory as a Master student. I was able to obtain my Master's degree in engineering through his guidance. I thank Professor Hamaguchi for allowing me to continue my graduate studies as a Ph.D student under his tutelage. I truly appreciate all the help and guidance he had given me, as well as, the opportunities to present my research in various international and local conferences. Professor Hamaguchi has truly been a great sensei to me, and has been instrumental in my efforts to obtain a Ph.D. degree.

I would like to acknowledge our collaborators, Drs. Eric Hudson and Leonid Belau of Lam Research Corporation, for the fruitful discussion that help in the progress of this research. I am also thankful for the support provided by the Japan Society for the Promotion of Science (JSPS) Research Fellowship for Young Scientists.

Moreover, I would like to thank Prof. Kazuhiro Karahashi, Dr. Tomoko Ito, and Shouichi Taira for the support with the experiments. I would also like to thank my colleagues in Hamaguchi Laboratory especially Erin, Anjar, Nina, Sarah, Umemura-san, Nagao-san, Nicolas, Enggar, Jomar, Pierre, Abdul, Ikuse-san, Isobe-san, Hojun, Jaber, Ichi-kun, Kita-kun, Kotani-kun, Kawabata-kun and Fujita-kun. You all have made my stay in Hamaguchi Laboratory fun and exciting. I hope that our connections would not be lost after we go our separate ways.

I also thank my family in the Philippines for their unending support in my endeavours to further my education. Even though we are miles apart, your love and support has been a source of strength for me.

Lastly, I thank God for all the blessings and protection He had bestowed upon me as I pursued my Ph.D. degree at Osaka University.

Abstract

As the sizes of semiconductor devices continue to shrink, fabrication of device structures on material surfaces with high accuracy poses unprecedented challenges to process technologies employed in the manufacturing of semiconductor devices such as NAND flash memory devices. NAND flash started as planar or 2D NAND. However, the scaling of 2D NAND was not able to keep up to the demand for higher memory capacity. As such, 2D NAND transitioned to 3D NAND. In 3D NAND, alternating films are deposited and stacked to form the basis of the memory cell. The number of stacked layers dictates the memory capacity. In the fabrication of such devices, hole channels with a high-aspect ratio (HAR) are etched through these layers. The higher the aspect ratio becomes, the more difficulties HAR etching faces. Therefore, the primary goal of this study is to understand the HAR etching process through molecular dynamics (MD) simulations supported by ion beam experiments.

To understand how energetic ions interact with the sidewalls of HAR channels during reactive ion etching (RIE), MD simulations for the scattering of neon, argon, and xenon ions on silicon (Si) and silicon dioxide (SiO_2) surfaces were performed. The simulations were performed at grazing-angle ion incidence to examine how the angular distribution of reflected ions deviates from that of the ideal specular reflection, depending on the ion mass, incident angle, and surface material and its roughness. It is found that, the higher the ion mass is, the less grazing the ion incident angle is, or the rougher the surface is, the larger the angular distribution of reflected ions becomes around the corresponding specular reflection angles. Quantitative information on such reflected ions can be used to predict the profile evolution of HAR channels in RIE processes.

Alternating films of SiO_2 and silicon nitride (SiN) are commonly used in 3D NAND devices. As such, MD simulations were performed to examine the etching of SiO_2, SiN, and oxide-nitride (ON) stacked layers by energetic fluorocarbon ions. Good agreement of etching yields obtained from the simulations and ion beam experiments was observed for

the etching of SiO_2 and SiN by CF_3^+ ions for the incident ion energy ranging from 200eV to 2,000eV. As to the etching of the ON bilayer, the SiO_2 and SiN layers were observed to be etched with their own etch rates at low ion incident energy. However, at sufficiently high incident ion energy, the oxide and nitride layers were mixed by energetic ion impact and the depth of the mixing layer exceeded the thickness of the top SiO_2 layer thickness, resulting in a single etch rate limited by the etch rate of the much deeper underlying SiN material. This suggests that, if the incident ion energy is high enough such that the thicknesses of the multilayers are lower than the ion penetration depth, the ON stacked layer exhibits a single etch rate determined by the mixed material of the oxide and nitride. As such, the etch rates in ONON multilayer etching would be dependent on the thickness of the films and the ion energy used.

Additionally, MD simulations of SiO_2 and SiN etched by CF_3^+ ions and Cl^+ ions were performed to provide insights on the etching with Cl-containing fluorocarbon plasmas. To do this, interatomic potentials for the interaction of chlorine with carbon and fluorine was first developed. Afterwards, the etching yields obtained from MD simulations were compared with ion beam experimental etching yield. Relatively good agreement between the simulation and experimental etching yields were obtained for the etching of Si, SiO_2 and SiN by Cl^+ ions with incident ion energy ranging from 50eV to 3,000eV. To understand the etching with Cl-containing fluorocarbon plasmas, the simulations of the etching of SiO_2 and SiN by CF_3^+ ions with and without Cl^+ injected with incident ion energy ranging from 500eV to 2,000eV at 0° and 60° were compared. It was shown that at 0°, addition of Cl^+ ions has minimal and even negative effect on the etch rate of SiO_2 and SiN. Only when the ions were injected at 60° did an increase in etch rate was observed.

This study also aims to understand the mechanisms of reactive ion etching processes to form nanometer-scale holes (nanoholes) into a SiO_2 surface region with a carbon mask by fluorocarbon plasmas, using MD simulation. The results showed that, in the case of ion beam etching by CF_3^+ ions, the etching yield generally increased with increasing ion energy, and etching at high ion incident energies was dominated by physical sputtering.

Preferential removal of oxygen was also observed, which resulted in Si-rich etched hole channel inner walls. Tapered etched hole channels were formed due to the re-deposition of sputtered atoms. The effects of the simultaneous irradiation of CF_3 radicals with CF_3^+) ion injection on the etching process were also investigated. It was shown that there was an optimum ratio of the radical to ion fluxes to maximize the etching yields.

Contents

Acknowledgments **iii**

Abstract **v**

Contents **vii**

Abbreviations **xiii**

1 Introduction **1**

1.1 Flash Memory Technology 1

1.1.1 3D NAND Flash Memory Technology 2

1.2 Etching Process 4

1.2.1 Reactive Ion Etching 5

1.2.2 High Aspect Ratio Etching 7

1.2.3 Mass-Selected Ion Beam System 8

1.3 Classical Molecular Dynamics 10

1.3.1 Interatomic Potential Function 11

1.3.2 Integration Algorithm of Newton's Equations of Motion 14

1.3.3 Statistical Mechanical Ensembles and Thermostat Algorithms . . . 16

1.3.4 MD Simulation Conditions 17

1.4 Objectives 20

2 Inert-gas Ion Scattering at Grazing Angle Incidence on Si and SiO_2 Surfaces **21**

2.1 Introduction 21

2.2 MD Simulation 23

2.3 Results and Discussion 27

2.3.1 Angular distributions of reflected ions 27

2.3.2 Reflection probabilities 32

2.4 Conclusions 36

3 Molecular Dynamics Simulation of Oxide-Nitride Bilayer Etching with Energetic Fluorocarbon Ions **39**

3.1 Introduction 39

3.2 Methodology 41

3.3 Results and Discussions 45

3.3.1 Etching of SiO_2 and SiN 45
3.3.2 Etching of an Oxide-Nitride Bilayer 56
3.3.2.1 Etching Yields and Etch Rates 56
3.3.2.2 Desorbed Species from the ON bilayer Etching 60
3.4 Conclusions 62

4 Molecular Dynamics Simulation of Oxide and Nitride Etching by CF_3^+ and Cl^+ 65
4.1 Introduction 65
4.2 MD Simulation 66
4.3 Interatomic Potential Model for Fluorocarbon and Chlorine Interaction . . 69
4.4 Results and Discussion 75
4.4.1 Simulation and Experimental Etch Yield Comparison 75
4.4.2 Etching of SiO_2 and SiN by CF_3^+ ions with Cl^+ ions 76
4.4.3 Desorbed Species from the Etching of SiO_2 and SiN by CF_3^+ and Cl^+ 82
4.5 Conclusion 85

5 Molecular Dynamics Study of SiO_2 Nanohole Etching by Fluorocarbon Plasmas 87
5.1 Introduction 87
5.2 MD Simulation 90
5.3 Results and Discussion 95
5.3.1 Etched Hole Profiles of SiO_2 with Carbon Masks by CF_3^+ Ion beams 95
5.3.2 SiO_2 Nanohole Etching with an Ideal Mask 100
5.3.3 SiO_2 Etching by Simultaneous FC Radical and Ion Irradiation . . . 105
5.4 Conclusions 107

6 General Conclusion 109

A Inert-gas Ion Scattering at Grazing Angle Incidence on Si and SiO_2 Surfaces – Supporting Results 113

B Etching of ONON Multilayer by CF_3^+ Ions 117

C MD Simulation of Oxide and Nitride Etching by CF_3^+ and Cl^+ – Supporting Results 119
C.1 Fluorocarbon and Chlorine Interatomic Potential Model 119
C.2 Depth Profiles of SiO_2 and SiN Etched by CF_3^+ and Cl^+ 125
C.3 Etch Rate of SiO_2 and SiN Etched by CF_3^+ and Ar^+ 128
C.4 Desorbed Species from the Etching of SiN by CF_3^+ and Cl^+ 129

D MD Study of SiO_2 Nanohole Etching by FC Plasmas – Supplementary Material 131
D.1 Interatomic Potential Functions 131

D.2 Deposition of CF_3 Radicals 135

Bibliography **137**

Research Achievements **155**

Abbreviations

Ar	Argon
AR	Aspect Ratio
ARDE	Aspect-Ratio Dependent Etching
BiCS	Bit-Cost Scalable
C	Carbon
CF_3	Trifluorocarbon
Cl	Chlorine
CTF	Charge-Trap Flash
DFT	Density Functional Theory
EEPROM	Electrically Erasable Programmable Read-only Memory
F	Fluorine
FC	Fluorocarbon
FG	Floating-Gate
HAR	High Aspect Ratio
LJ	Lennard-Jones
MD	Molecular Dynamics
NAND	Not And
Ne	Neon
ONO	Oxide-Nitride-Oxide
ONON	Oxide-Nitride-Oxide-Nitride
RIE	Reactive Ion Etching
RF	Radio Frequency
Si	Silicon

SiO_2	Silicon Dioxide
SiN	Silicon Nitride
SRIM	Stopping and Range of Ions in Matter
SW	Stillinger-Weber
TCAT	Terabit Cell Array Transistor
vdW	Van der Waals
WL	World Lines
Xe	Xenon
2D NAND	Two-dimensional NAND
3D NAND	Three-dimensional NAND

Chapter 1

Introduction

1.1 Flash Memory Technology

Flash memory is a non-volatile memory technology commonly used in electronic devices, and was first introduced by Toshiba in 1980's. The name came from the fact that the contents of the memory cells can be erased in a flash. During this time, memory devices were based on two different logic gates: NOR and NAND. NOR flash is generally used for low-density, high-speed read applications. On the other hand, NAND flash is for low-cost, high-density, data storage applications [1–3]. NAND flash memory technology was also first developed by Toshiba to address the memory density limitation of their Electrically Erasable Programmable Read-only Memory (EEPROM) technology [4]. Due to its cost effectiveness, NAND flash has become the primary solution to any platforms (e.g. smartphones, laptops, digital cameras, etc.) that requires data storage [3, 5, 6].

The structure of NAND flash was initially made by connecting floating-gate (FG) transistors to form planar array of memory-cells (2D NAND). In such design, the memory capacity would be limited by the number of transistors that can be integrated planarly in a single-chip. To increase the memory capacity, the node size of transistors was continuously miniaturized [5, 6]. Both Micron [7] and SK Hynix [8] has shown the feasibility of a

NAND flash with 16nm node, while Samsung Electronics [9] was able to push to 14nm node. Though major manufacturers of NAND flash has shown the feasibility of reaching $\leq$ 16nm planar node, it was no longer economically viable. The fundamental limitation in integration of transistors to increase the memory capacity of 2D NAND has already been reached. This led to the scaling of NAND flash memory technology to transition from 2D to 3D [5, 6, 10].

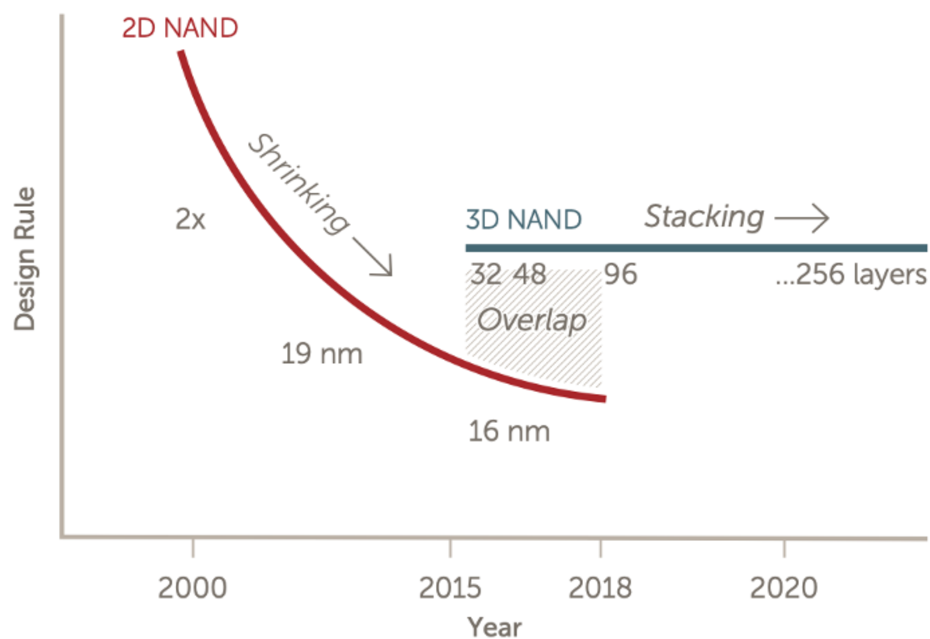

Figure 1.1: Design rule trend: 2D NAND vs 3D NAND [10].

1.1.1 3D NAND Flash Memory Technology

When the scaling of 2D NAND was no longer economically viable, the research and development on 3D NAND emerged to address the demand for higher memory capacity. The thought behind 3D NAND is similar to the thought behind the construction of high-rise apartments and condominiums, i.e. increase capacity vertically. By stacking memory cells vertically, the memory density per area would increase in proportion to the number of stacked cells [5, 6, 11]. The pioneering work on 3D NAND started with a 2 stacked

memory cells [12] which culminated to the first cost-effective 3D NAND proposed by Toshiba called the Bit-Cost Scalable (BiCS) shown in Fig. 1.2 [6, 13].

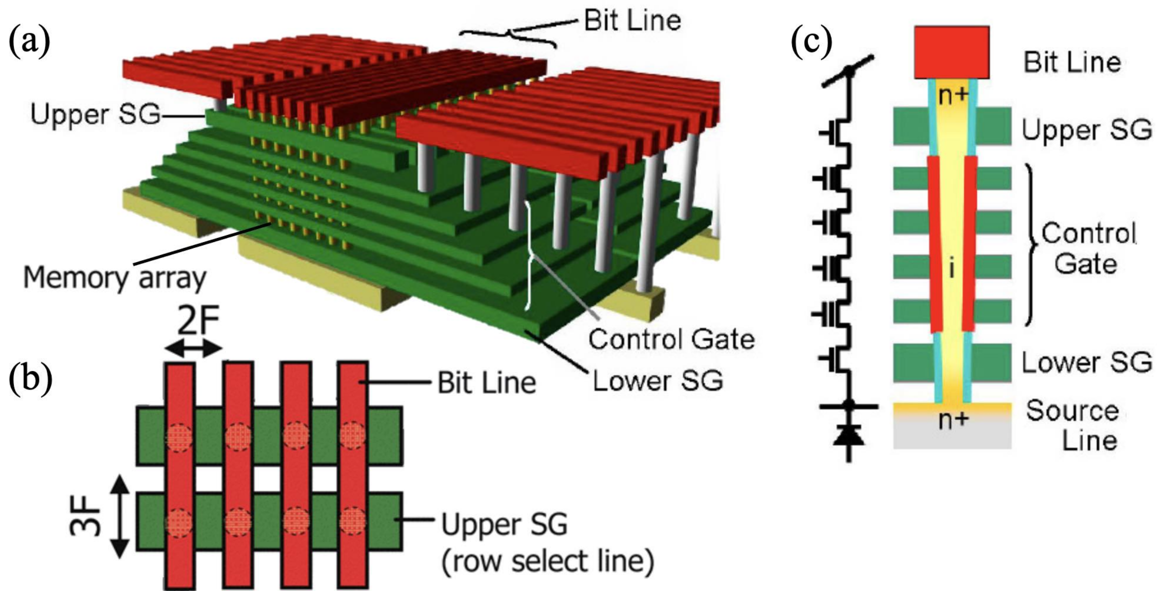

Figure 1.2: (a) Bird's-eye view of BiCS Flash memory; (b) Top-down view of BiCS Flash memory array; (c) Cross section of BiCS flash memory string [13].

There are two different mainstream memory cell technology in 3D NAND: the conventional FG cell and the charge-trap flash (CTF) cell shown in Fig. 1.3. In general, a memory cell is comprised of a control gate, blocking layer, storage layer, tunneling layer on the substrate. In conventional FG cell, the storage layer is called the floating-gate made up of a conducting material. In contrast, the storage layer in CTF cell is a dielectric. The control gates in these memory cells are connected by the world lines (WL). 3D NAND with FG cells typically use polysilicon WL, while 3D NAND with CTF cells uses tungsten WL. The drain of the memory cells are connected by the bit lines. Currently, most 3D NAND structures uses CTF cells due to a thinner storage layer, and simpler fabrication processes in contrast to conventional FG cells [2, 6, 11, 14, 15].

The fabrication process of 3D NAND is dependent on its structure which varies depending on the manufacturer. However, key steps in the fabrication process remains the same. The fabrication process starts with film stack deposition step wherein alternating films (e.g. SiO_2 and SiN) are deposited on the the substrate. This step can be referred to

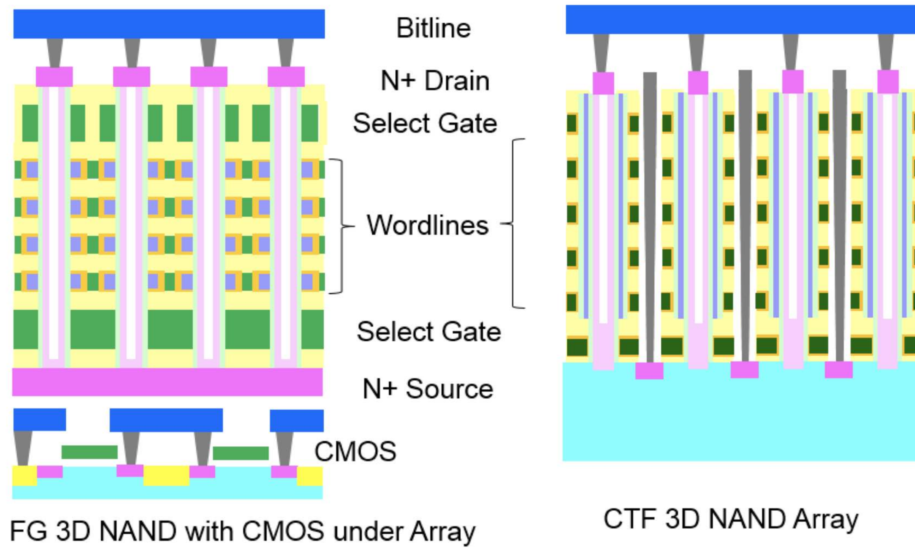

FIGURE 1.3: FG Flash 3D NAND (left); CTF 3D NAND (right) [14].

as WL stacking and has been the primary scaling path of 3D NAND since the memory capacity can be increased by increasing the number of stacked layers. The film stack deposition is followed by the formation of the vertical channels. This is done by first depositing a mask and creating hole openings to proceed with the high-aspect ratio (HAR) channel etch step. In HAR etching, the hole channels are etched through all layers of deposited films. The next key step is the stair etch wherein the staircase shape structure of 3D NAND is formed to create the contact pads for the WL's. This is then followed by the slit etch step. In this step, a hardmask is first deposited and patterned with openings. The memory cell arrays are then formed by separating the hole channels with the slit etch step. The last key step would be the formation of the bit lines that are usually perpendicular to the WL's [14, 16–19]. The focus in this study is the HAR etching step in the fabrication of 3D NAND flash memory devices.

1.2 Etching Process

The fabrication process of 3D NAND discussed in the previous section showed how crucial the etching process is in the semiconductor industry. The etching process is usually

preceded by the lithography process. In lithography, resist or mask are deposited on top of the films on the wafers. The desired patterns are then made on the mask. Etching would then transfer these patterns on films by selectively removing parts of the deposited films to create the desired circuit design. Etching is categorized as wet etching and dry etching. In wet etching, the films or material to be etched are removed isotropically by chemical solutions. On the other hand, dry etching removes the films anisotropically using reactive ions or vapor phase etchant. Dry etching can generally be categorized into three types: (1) reactive ion etching (RIE); (2) sputter etching; and (3) vapor phase etching. This study would only focus on RIE as it is the process involve in 3D NAND fabrication [20–22].

1.2.1 Reactive Ion Etching

RIE is a type of dry etching process that uses plasma to generate reactive ions that would etch the material. Chen defines plasma as *"a quasineutral gas of charged and neutral particles which exhibits collective behavior"* [23]. In RIE, a parallel-plate system is generally used as shown in Fig. 1.4. In such system, the wafer is placed on the bottom electrode, after which the entire chamber is pumped down to high vacuum conditions. The gas with the desired chemistry would be introduced. In general, plasma is generated by applying 13.56MHz RF power to the electrodes in the chamber containing process gas. The gas would be ionized, and the plasma comprising of a quasineutral mixture of ions, electrons, photons, neutrals, molecules, and atoms would be generated. Reactive species such as radicals could react with the surface atoms on the wafer to form volatile byproducts that would then be removed via the exhaust. This process could be referred to as "chemical sputtering" since the reactive species induces chemical reactions that would lead to desorption of volatile byproducts. In RIE, surface atoms could also be etched if the generated ions have a high kinetic energy that can sputter the surface atoms without reacting. This process could be referred to as "physical sputtering". In RIE, chemical sputtering is isotropic while physical sputtering is highly anisotropic. As such,

etch channels could have a non-uniform profile. It is therefore necessary to balance the chemical and the physical aspect of RIE to have a uniform etch. In some cases, a bias voltage is applied to the bottom electrode that hold the wafer. By applying a bias voltage, the ions from the plasma could be directed towards the wafer which would make the RIE highly directional and anisotropic. As such, RIE is the widely used etching process in semiconductor industries [20–26].

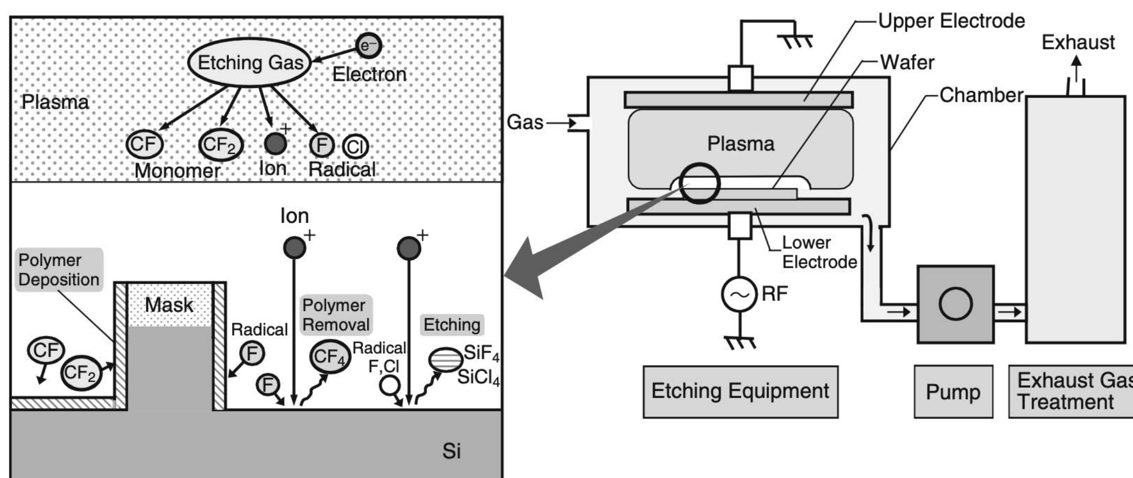

FIGURE 1.4: Schematic Diagram of RIE [20].

Fluorocarbon (FC) plasma is one of the most commonly used plasma in RIE of Si-based materials in semiconductor industries. The basis in using FC plasma in the etching of Si-based materials is the reaction of silicon with fluorine to form volatile by products such as SiF_4. Examples of etching gases for FC plasma are CF_4, C_2F_4, and C_2F_6. In CF_4 plasma, the dissociation of the gas would primarily produce CF_3^+, CF_3, F, CF_3^-, and F^- [27–29]. As such, the main species of interest in this research is CF_3. Due to the negative bias applied to the bottom electrode that holds the wafer, negative ions do not contribute to the etching. On the other hand, studies have shown that the ions and radicals are the primary contributors to the etching. However, carbon deposition on the wafer and RIE chamber has been observed for FC plasma etching. This led to the fluorine to carbon (F/C) ratio concept in FC plasma etching. The F/C ratio has become an important process parameter in determining whether etching or deposition

of a CF film would dominate the process. In general, at high F/C ratio, etching would proceed due to the high flux of fluorine that would react with Si-based material. At low F/C, the plasma would become fluorine-deficient and carbon would deposit. At a certain point, the deposition of carbon would dominate over etching and lead to polymerization. In the etching of SiO_2 by CF_4 plasma, Si atoms could be etched by F atoms as SiF_x species, while O atoms could be etched as CO_x or COF_2 species. As such, in the presence of oxygen, the carbon deposition could be decreased. The role of the F/C ratio in FC plasma etching has been qualitatively illustrated by Coburn and Winters as shown in Fig. 1.5 [27, 29–34].

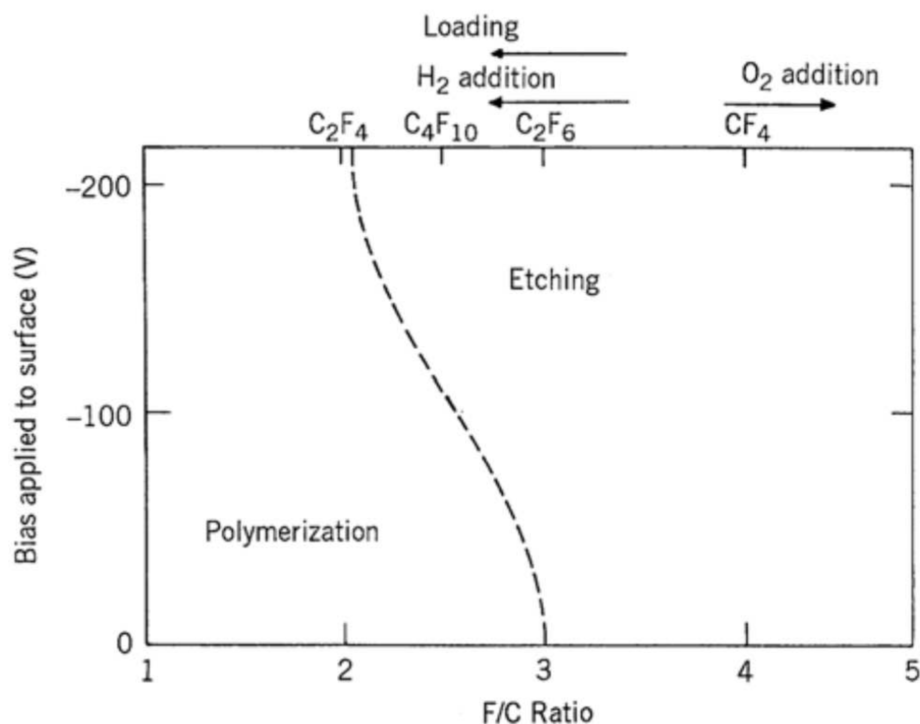

FIGURE 1.5: The qualitative effect of the fluorine to carbon (F/C) ratio on etching and polymerization processes in a FC plasma [32].

1.2.2 High Aspect Ratio Etching

As discussed previously, HAR etching is one of the key processes in the fabrication of 3D NAND. In this step, hole channels are etched through all the deposited films. This

step is the focus in this study as it is the main roadblock in further scaling of 3D NAND devices to increase its memory capacity. When the number of layers is increased, etching a hole channel with a straight and smooth profile becomes more difficult [14, 16]. Ideally, a straight and smooth channel is needed to have a well fabricated 3D NAND device. However, deviations from the ideal profile could occur and these deviations fall under the umbrella term aspect-ratio dependent etching (ARDE) phenomena. ARDE happens in all etching process but is much more of a concern in HAR etching. In ARDE, the etch rate decreases as the aspect-ratio increases. As the aspect-ratio increases, the flux of reactive species reaching the bottom of the etched channel decreases, and it becomes more difficult for the byproducts to escape. This is also referred to as RIE lag. In some cases, etch stop could occur wherein the etched channel does not reach the substrate [24, 25]. Incoming ions could be deflected by the mask, the sidewalls, and/or by other species in the plasma. The deflected ions could change the direction of the etch front, thus causing the etch channels to have non-ideal profiles such as tapered, twisted or bowed. In a channel with HAR, the sputtered or etched atoms could have difficulty in escaping the channel. In such cases, re-deposition of the etched or sputtered atoms onto the channel sidewalls could occur which contributes to formation of non-ideal profiles as shown in Fig. 1.6 [24, 25, 35–37].

1.2.3 Mass-Selected Ion Beam System

As discussed previously, parallel-plate system containing several different gas admixtures is generally used to ignite the plasma in RIE. In such a process, the plasma would contain various ions that would participate in etching. However, understanding the interactions of all the ions in such a system is extremely difficult. As such, a mass-selected ion beam system wherein the etching of a material with one type of ion has been developed (Fig. 1.7). The details of the beam system were discussed in Ref. 38 and would not be discussed here.

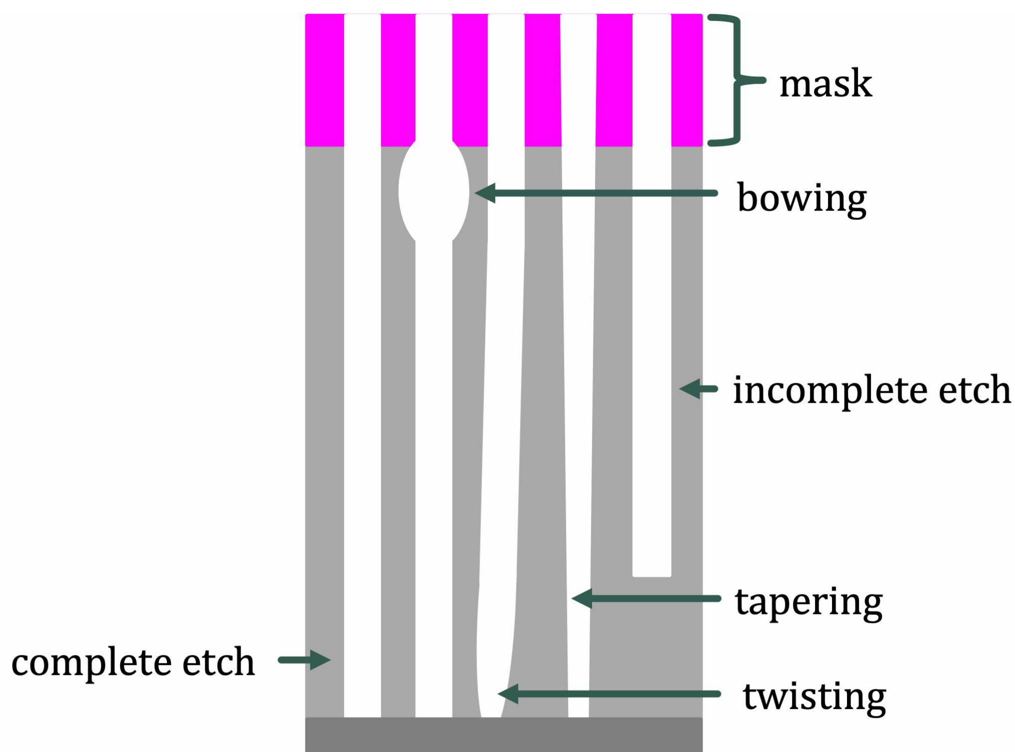

FIGURE 1.6: HAR Etching Profiles

.

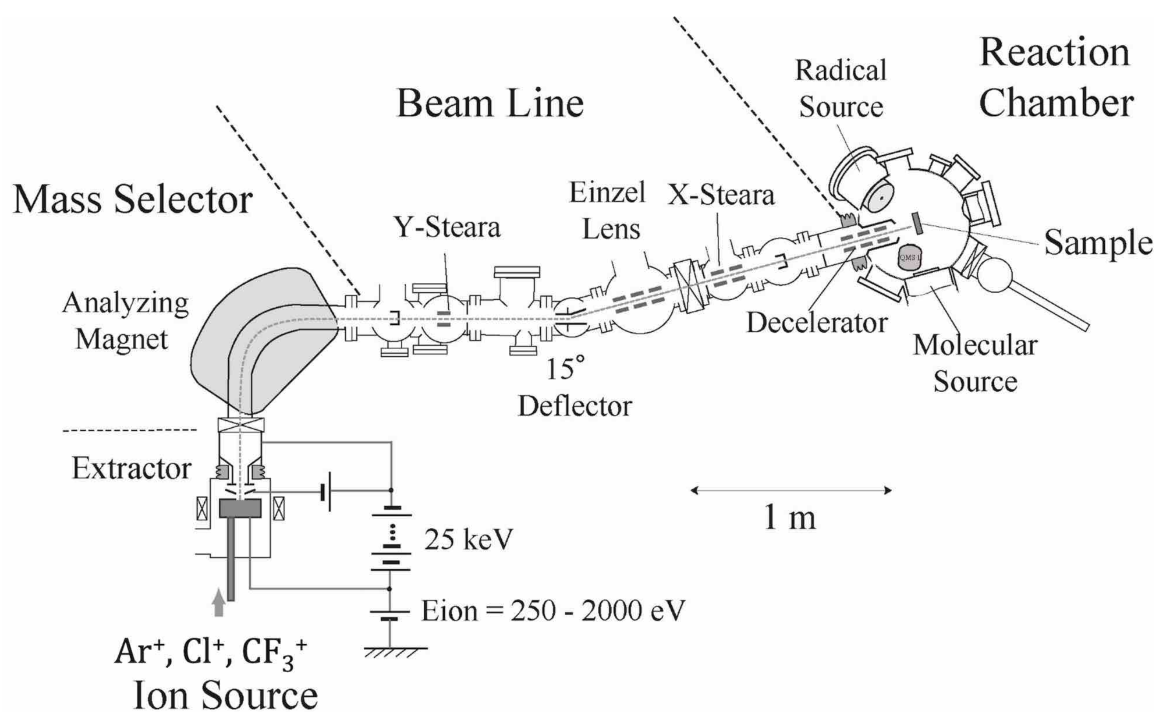

FIGURE 1.7: Schematic diagram of the mass-selected ion beam system.

Etching is done by directing the mass-selected ion beam towards the sample with a metal stencil mask. After ion bombardment, the difference in the height of the unetched

(i.e. covered by the mask) and etched part of the material would be measured *ex-situ* by either a contact profilometer or an inference film thickness gauge. The ion beam experimental yield Y could then be calculated with

$$Y = \frac{dn}{D} \tag{1.1}$$

where d is the etched depth in cm, n is the density of the etched material in atom/cm^3, and D is the dose in ion/cm^2. The dose D is given by

$$D = \frac{It}{eS} \tag{1.2}$$

where I is the ion current in ampere, t is the beam irradiation time in seconds, e is the elementary charge, and S is the beam irradiation surface area in cm^2.

1.3 Classical Molecular Dynamics

The properties and behaviour of a real physical system, and reaction dynamics of various process can be studied by molecular dynamics (MD) [39, 40]. In MD, the nucleus and the electron of an atom can be treated as one particle due to the Born-Oppenheimer approximation. The Born-Oppenheimer approximation approximates the motion of the atom as the motion of the nucleus since neutrons move significantly slower than the electrons due to the large difference in their masses [41, 42]. As such, MD is a numerical simulation method that treats the system to be simulated as a combination of mass-point particles interacting with each other through a defined interatomic potential function. The interatomic potential function would define the forces that acts on any given atom given the position of other atoms. By numerically solving Newton's equations of motion, how the forces calculated from the interatomic potential function affects the motion of the atoms can be determined [39, 40, 42–44].

The accuracy of the MD simulation is highly dependent on the interatomic potential functions as these functions describes the atomic interactions. Atomic interactions could be short-range, bonded interaction such a bond stretching, or long-range, non-bonded interaction such as Van der Waals [45]. Interatomic potential functions provides only a good approximation of true atomic interactions since atomic interactions are governed by quantum mechanics [39, 43, 46]. Short-range interaction between two atoms is shown in Fig. 1.8 wherein the interactions between two atoms switches from repulsive to attractive at an equilibrium distance r_0. There are many interatomic potential functions that have been developed as the use of simulations in research has expanded. However, we would only discuss the Stillinger-Weber potential, Molière repulsive pair potential, and the Van der Waals (VdW) potential as they are the basis of the potential functions used in this study.

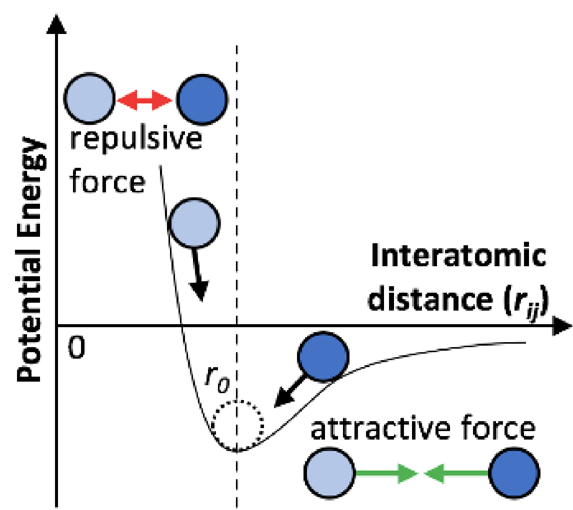

FIGURE 1.8: Short-range Atomic Interaction Diagram [47]

.

1.3.1 Interatomic Potential Function

The Stillinger-Weber (SW) potential is a many-body potential energy function developed by Stillinger and Weber [48] to describe the interactions in solid and liquid forms of Si. In a system containing N particles, the potential-energy function Φ describing the interactions

among the particles can be separated into one-body V_1, two-body V_2, three-body V_3, until N-body V_N contributions as shown in Eq. 1.3.

$$\Phi(1, ..., N) = \sum_{i} V_1(i) + \sum_{\substack{i,j \\ i<j}} V_2(i, j) + \sum_{\substack{i,j,k \\ i<j<k}} V_3(i, j, k) + ... + V_N(1, ..., \mathrm{N}) \tag{1.3}$$

Eq. 1.3 is simplified by assuming that the one-body V_1 contribution that describes the external forces acting on the system is zero. Additionally, the V_N contribution is also assumed to converge to zero with increasing number of N for Eq. 1.3 to be useful in computational simulation. The total potential Φ can therefore be assumed as a linear combination of the two-body V_2 and three-body V_3 interactions as shown in Eq. 1.4 [48, 49].

$$\Phi(r_1, \cdots r_N) \cong \sum_{i<j} V_2(i, j) + \sum_{i<j<k} V_3(i, j, k) \tag{1.4}$$

SW-type potential functions for Si-O-Cl and Si-O-F systems were derived by Ohta and Hamaguchi [45, 50]. In this SW-type potential, all atoms are considered charge-neutral. Eq. 1.4 was parameterized by first defining the two-body V_2 contribution into the repulsive V_R and attractive or bonding V_B interaction between two atoms.

$$\begin{aligned} V_R &= ar^{-p} \exp\left(\frac{c}{r - r_c}\right) \\ V_B &= -br^{-q} \exp\left(\frac{d}{r - r_c}\right) \end{aligned} \tag{1.5}$$

If we assume that V_R is linearly dependent on the square of V_B ($p = 2q$ and $c = 2d$), the two-body V_2 interaction for the ith and j^{th} atoms would be

$$V_2(i, j) = \begin{cases} ar^{-2q} \exp\left(\frac{2d}{r_{ij} - r_c}\right) - br^{-q} \exp\left(\frac{d}{r_{ij} - r_c}\right), & \text{if } r_{ij} < r_c \\ 0, & \text{if } r_{ij} \geq r_c \end{cases} \tag{1.6}$$

where a, b, d, q, and r_c are parameters with r_c being the interatomic cutoff distance [45, 50, 51].

The three-body V_3 interaction describes the angular dependencies of the ith, j^{th}, and k^{th} atoms given by

$$V_3(i,j,k) = h_{jik}(r_{ij}, r_{ik}, \theta_{jik}) + h_{ijk}(r_{ji}, r_{jk}, \theta_{ijk}) + h_{ikj}(r_{ki}, r_{kj}, \theta_{ikj}). \tag{1.7}$$

The h function in Eq. 1.7 is dependent on the angle between three atoms θ (the vertex atom is denoted by the center subscript), and the distances r of the two atoms from the vertex atom given by

$$h_{ijk}(r_{ji}, r_{jk}, \theta_{ijk}) = k_{ijk}|\cos\theta_{ijk} - \Theta_{ijk}|^{\gamma_{ijk}} f_{ij}(r_{ij}) f_{jk}(r_{jk}). \tag{1.8}$$

where k, Θ, and γ are parameters. The f function in Eq. 1.8 prevents the overestimation of the angular dependency, and is dependent on V_2 given by

$$f_{ij}(r) = \begin{cases} 1, & r \le r_{min}, \\ \frac{V_2(r)}{V_{2min}}, & r_{min} < r < r_c, \\ 0, & r > r_c, \end{cases} \tag{1.9}$$

where r_{min} is the distance between the ith and jth at the minimum two-body interaction energy V_{2min} [45, 50, 51].

The parameters for two-body V_2 and three-body V_3 potential functions are determined by Levenberg-Marquardt nonlinear fitting of the potential energy curve of various atomic configurations. The potential energy curves are obtained from *ab initio* quantum mechanical calculations based on density functional theory (DFT) using the software *Gaussian* [52].

The interatomic potential function used in this study to describe the short-range interactions of the system of interest excluding interactions with noble gases is based on this parameterized SW potential function. The short-range interactions with noble gases

are described by the Molière [42] repulsive pair potential given by

$$V(r_{ij}) = \frac{Z_i Z_j e^2}{4\pi\epsilon_0 r_{ij}} \left(0.35 \exp\left(\frac{-0.3 r_{ij}}{a}\right) + 0.55 \exp\left(\frac{-1.2 r_{ij}}{a}\right) + 0.10 \exp\left(\frac{-6.0 r_{ij}}{a}\right)\right) \tag{1.10}$$

with

$$a = 0.885 a_0 (Z_i^{1/2} + Z_j^{1/2})^{-2/3}$$

where Z_i and Z_j are the atomic numbers, and $a_0 = 5.29177249 \text{ x } 10^{-11}$ is the Forsov screening length and Bohr radius [42, 50].

Long-range interactions among the atoms are also considered in the simulation, and are described by Van der Waals potential given by

$$V_{VdW}(r) = \begin{cases} 4\epsilon \left\{ \left(\frac{\sigma}{r}\right)^{12} - \left(\frac{\sigma}{r}\right)^{6} \right\} \exp\left(\frac{d_1}{r-c_1} - \frac{d_2}{r-c_2}\right) & \text{if } c_2 < r < c_1, \\ 0, & \text{otherwise} \end{cases} \tag{1.11}$$

where $\epsilon = 0.0108$ eV, $\sigma = 3.5$ Å, $d_1 = d_2 = 0.1$ Å, $c_1 = 8.0$ Åand $c_2 = 3.5$ Å. The repulsive interaction of the Van der Waals is not included since the repulsive interaction of the atoms is already accounted by the two-body V_2 potential that describes covalent bonding. Also, the minimum bond energy in Van der Waals interactions is extremely small ($\backsimeq 10^{-2}$ eV) in comparison to typical covalent bonds (several eV) [50, 53].

1.3.2 Integration Algorithm of Newton's Equations of Motion

With a relatively accurate interatomic potential, the motion of the atoms that are treated as classical particles can be determined by numerically solving Newton's equations of motion. For a system containing N particles interacting by a potential $\Phi(\vec{r}_i)$, Newton's equation of motion is given by

$$\vec{F}_i = m_i \ddot{\vec{r}}_i = -\frac{\partial \Phi(\vec{r}_i)}{\partial \vec{r}_i} \tag{1.12}$$

with

$$\vec{p_i} = m_i \dot{\vec{r_i}}$$

where $i = 1, 2 \ldots$ N, m_i is the mass of particle i, and $\dot{\vec{r_i}}$ and $\ddot{\vec{r_i}}$ are the first and second derivative respectively at position $\vec{r_i}$ with respect to time t. To have an accurate representation of the interactions of the atoms in the system, $\vec{r_i}$ should be evaluated at small time steps Δt [44]. The differential equations to be solved would increases as the system to be simulated gets larger. As such, various integration algorithms has been developed to integrate Newton's equations of motion. One of the common integration algorithm is the Verlet algorithm [44, 54] given by

$$\vec{r_i}(t + \Delta t) = 2\vec{r_i}(t) - \vec{r_i}(t - \Delta t) + \frac{1}{m_i}\vec{F_i}(t)(\Delta t)^2 \tag{1.13}$$

where the new position at time $(t + \Delta t)$ is calculated from the position and force at time t, and the position at time $(t - \Delta t)$. The velocity can be derived from Eq. 1.13 and is given by

$$\vec{v_i} = \frac{\vec{r_i}(t + \Delta t) - \vec{r_i}(t - \Delta t)}{2\Delta t} \tag{1.14}$$

Another integration algorithm is the Leapfrog algorithm. This algorithm is a modification of the Verlet algorithm wherein the new particle position is calculated from the next half-step $\Delta t/2$ velocity given by the velocity the leaps over the coordinate, thus the name *leapfrog* [44].

$$\begin{aligned} \vec{v_i}\left(t + \frac{\Delta t}{2}\right) &= \vec{v_i}\left(t - \frac{\Delta t}{2}\right) + \frac{1}{m_i}\vec{F_i}(t)(\Delta t) \\ \vec{r_i}(t + \Delta t) &= \vec{r_i}(t) + \vec{r_i}\left(t + \frac{\Delta t}{2}\right)\Delta t \end{aligned} \tag{1.15}$$

The velocity can be derived from Eq. 1.15 and is given by

$$\vec{v_i} = \frac{v_i\left(t + \frac{\Delta t}{2}\right) + v_i\left(t - \frac{\Delta t}{2}\right)}{2}. \tag{1.16}$$

1.3.3 Statistical Mechanical Ensembles and Thermostat Algorithms

The instantaneous positions and velocities of all particles in the system can be obtained by integrating Newton's equations of motions. However, properties of the system cannot be determined with just the positions and velocities of the particles. Statistical mechanics must be used to obtain relevant macroscopic properties from MD simulation [39].

In this study, the microcanonical NVE ensemble is used. An NVE ensemble describes an adiabatic process wherein the total energy of the system $E_{Total} = E_{Potential} + E_{Kinetic}$ is conserved in which the number of the atoms / particles N and the volume of the system V are constant. With an NVE ensemble, the system is allowed to evolve under microcanonical conditions. Other statistical ensemble are NPT and NVT. An NPT ensemble describes an isothermal-isobaric system wherein the number of particles N, the pressure P and temperature T are kept constant. On the other hand, NVT is an ensemble with the number of particles N, the volume of the system V, and the temperature T are kept constant [39, 44, 45].

In MD simulations, the system is first allowed to evolve under microcanonical NVE ensemble. After which, the system would be cooled down to room temperature (300 K) through thermostat algorithms. One of the most common thermostat algorithms is the Nose-Hoover thermostat algorithm. The Nose-Hoover thermostat was proposed by Nose and extended by Hoover wherein the temperature of the system is controlled by coupling it to a heat bath [55, 56].

For the simulations done in this study, the temperature of the system is cooled down by decreasing the velocities of all atoms through Langevin thermostat [44, 57]. In Langevin dynamics, the Newton's equation of motion is modified to describe the movement of a particle in a viscous system. This is done by adding the noise term $\vec{\xi_i}$ that describes Brownian motion, and a friction constant Γ_i that determines the rate of temperature

relaxation given by

$$m_i \ddot{\vec{r}}_i = \vec{F}_i - m_i \Gamma_i \dot{\vec{r}}_i + \vec{\xi}_i(t). \quad (1.17)$$

Aside from Langevin thermostat, another thermostat algorithm called Berendsen Weak-Coupling algorithm was employed in the MD simulations. In the Berendsen thermostat [58], a heat bath with a predefined temperature T_d is weakly coupled to the system. When the temperature of the system T fluctuates from T_d, T is corrected by re-scaling the velocities of all particles at the rate of the time constant τ_T by the scaling factor χ where Δt is the defined time step. Continuous velocity scaling causes the kinetic energy from high-frequency motion (i.e. bond stretching, angle bending) to be repressed, while kinetic energy from low-frequency motion (i.e. global translation, global rotation) are increased. This causes the system to exhibit an unphysical phenomenon called the 'flying ice cube' wherein the system is frozen in a single conformation that translates or rotates in space [44, 58, 59]. As such, Berendsen thermostat is only employed for the last 100fs in all simulations.

$$\frac{dT}{dt} = \frac{T_d - T}{\tau_T} \quad (1.18)$$

$$\chi = \left[1 + \frac{\Delta t}{\tau_T}\left(\frac{T_d}{T} - 1\right)\right]^{1/2}$$

1.3.4 MD Simulation Conditions

The etching process is simulated in MD by injecting a predefined impact particle referred to as 'ion' on the material to be etched referred to as substrate. All simulations in this study was done with MDsurf simulation code developed in the Hamaguchi Laboratory that has been used in several studies [45, 53, 60–72].

In the beginning of the MD simulation, the substrate is first created by replicating its defined unit cell in all directions until the desired initial dimensions of the substrate is attained. The initial velocities of the particles were randomly assigned based on the

relation

$$v = \frac{k_b T_i}{m} \tag{1.19}$$

where T_i is the initial temperature at 300 K, k_b is the Boltzmann constant, and m is the particle mass [39, 45]. Periodic boundary conditions are applied in the horizontal directions. As such, an actual surface can be simulated. A 0.5 nm layer of atoms at the bottom of the substrate are fixed ($v = 0$) to prevent lateral displacement of the simulation box. This layer is referred to as 'anchor'. The anchor is continuously added under two conditions: (1) atoms reached passed the bottom; and (2) the volume-averaged temperature T_{total} of the substrate exceeds the defined maximum temperature T_{max} (usually 1,700 K). With such conditions, the height of the substrate is theoretically infinite, and would only be defined once the simulation has been stopped. Before injecting the ions, the substrate is relaxed at 300K for 10,000fs to relieve substrate stress. The substrate is also relaxed whenever an anchor is added.

Once the substrate is created, the injection cycle is started by placing the ion at random x and y directions. The ion is then injected towards the substrate at the defined incident angle and ion energy. In all MD simulations, the electrical charges of the ions are not considered as part of the interatomic forces. As such, though the impact particles are referred to as ions, the ions are treated as neutral species having the same kinetic energies. This approximation is based on the assumption that charged species in the plasma are neutralized at the moment of impact on the surface by the Auger effect [73, 74]. Upon ion injection, the kinetic energy of the ion is transferred to the substrate, then collision cascade occurs. This step is referred to as the energy preservation step since the system is allowed to evolve under constant total-energy conditions (NVE ensemble). The energy preservation step generally lasts for 300fs. Due to the kinetic energy transfer from the ion, the temperature of the system increases. As such, the system is artificially cooled down to prevent unrealistic heating. This is done by decreasing the velocities of all atoms with a Langevin thermostat for about 1600fs. Berendsen thermostat was then employed for the last 100fs of the injection cycle. Berendsen thermostat is only applied for 100fs to suppress

the 'flying ice cube' effect. A variable time step from 0.2fs to 0.5fs was used which would be adjusted depending on the fastest calculated velocities of the particles. The time step is small enough for good conservation of total energies of isolated systems. Except for the duration of the Berendsen cooling, the duration of the steps in the injection cycle can be varied as necessitated. In general, one injection cycle lasts for 2,000fs. The injection cycle is repeated for more than 1,000 times to have statistical accuracy in calculating macroscopic properties of the etching process such as etch yield and etch rate.

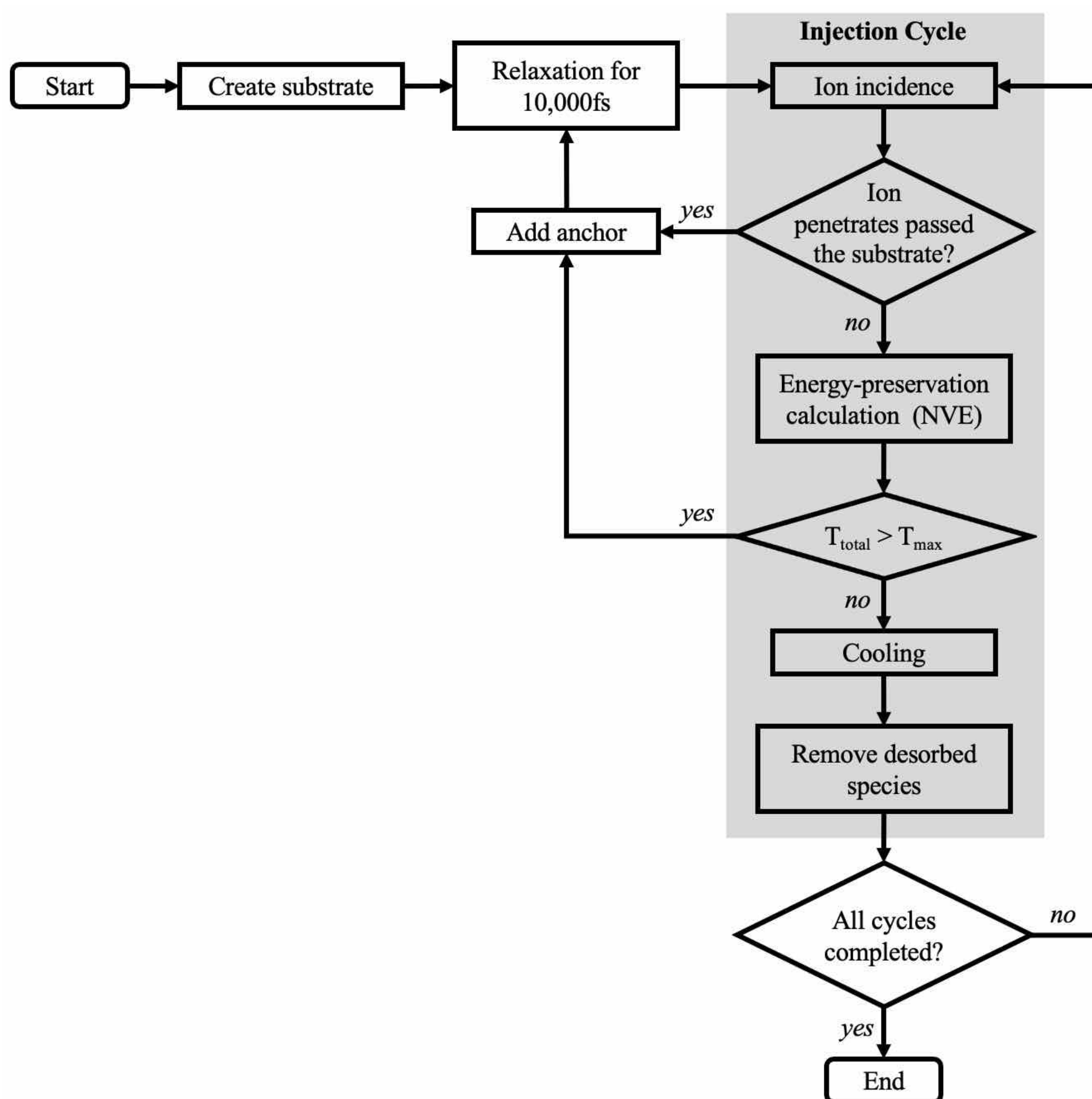

FIGURE 1.9: Flow chart of the MD simulation

.

1.4 Objectives

The primary objective of this research is to provide insight in the mechanism of the high aspect ratio etching step in the fabrication of 3D NAND devices through MD simulations supported by beam experiments. As HAR etching is a complex problem, the research has been divided into four main sections.

In Chapter 2, ion scattering simulations on smooth and rough surfaces of Si and SiO_2 by Ne^+, Ar^+, and Xe^+ ions were performed. The ions were injected at glancing angle to represent how ions interacts with the sidewalls of HAR channels. By doing this, the effects of atomic scale roughness on ion scattering could be inferred. In Chapter 3, etching simulations of SiO_2, SiN, and oxide-nitride multilayer by ${CF_3}^+$ ions were performed. This was done to understand how the etching mechanism changes when etching through different materials. In Chapter 4, etching simulations of SiO_2, and SiN by ${CF_3}^+$ ions and Cl^+ ions were performed to provide insights on the etching with Cl-containing fluorocarbon plasmas. To do this, interatomic potentials for the interaction of Cl with fluorocarbon were first developed. Simulation etch yields were compared with ion beam experiments to validate the MD simulation. In Chapter 5, etching simulations of SiO_2 with carbon masks by ${CF_3}^+$ ions were performed. This was done to understand the mechanisms of reactive ion etching processes to form nanometer-scale holes (nano-holes) into a SiO_2 surface region with a carbon mask by fluorocarbon plasmas.

Chapter 2

Inert-gas Ion Scattering at Grazing Angle Incidence on Si and SiO_2 Surfaces

2.1 Introduction

Semiconductor devices with higher integration have been continuously developed to address the demand for high-speed information processing and communication. NAND flash memory technology [6, 16, 17, 75] has been the leading solution to any platform that requires data storage. Manufacturing of 3D NAND devices requires the formation of extremely deep holes with relatively small cross-section diameters. Their aspect ratio (i.e., the ratio of the depth to the diameter) has continued to increase to accommodate more memory cells along the sidewalls of deep high-aspect-ratio (HAR) holes or channels. Plasmas are widely used to etch material surfaces in semiconductor manufacturing processes [27, 28, 76–79]. Simultaneous irradiation of energetic ions and chemically reactive species generated in a plasma can efficiently etch a material surface, which is called

reactive ion etching (RIE) [20, 80]. RIE to form HAR channels is considered to be one of the most challenging processes in 3D NAND manufacturing [81–84].

In RIE processes to form HAR channels (i.e., HAR etching), some energetic ions hit the sidewalls at grazing incidence and get reflected [61, 85, 86]. Most of such ions are considered to be reflected specularly on the sidewalls. However, depending on the sidewall materials (i.e., chemical compositions) and surface roughness, they may be reflected differently. Due to the difficulty of ion scattering experiments at grazing incidence, most studies on ion scattering on trench or hole sidewalls have been performed with numerical simulation. For examples, Van Nguyen *et al.* [87] and Dalton *et al.* [88] showed that ion scattering from the sidewalls greatly affected the mechanisms of trench etching. Abrams and Graves [89] modeled the scattering of low energy argon (Ar) ions ($\leq$ 200 eV) on silicon dioxide (SiO_2) surfaces and showed that incident angle less than 85° from the surface normal roughened the surface, which consequently affected the reflection characteristics of the ions incoming at glancing angles. Cagomoc *et al.* [90] showed incident fluorocarbon ions colliding with the SiO_2 sidewalls at glancing angles during hole channel etching preferentially sputtered off oxygen (O) atoms.

While few experimental studies seem to have been published so far of grazing angle scattering on silicon (Si)-based material surfaces, some studies examined ion scattering on carefully prepared smooth and pristine metal surfaces. Romney and Anderson performed molecular beam experiments to study the scattering of 0.05 eV–5 eV Ar from silver (Ag) (111) surfaces [91]. They reported that the scattering distributions of Ar at all energies peaked at/near specular angles. Hays *et al.* extended the energy range to 20 eV, wherein they also observed specular reflection [92]. Scattering experiments of 3 keV noble gas atoms and ions from a copper (Cu) (111) surface under grazing incidence by Pfandzelter *et al.* showed polar-angle distributions that peaked at the specular reflection [93].

The goal of this study is to understand the effect of atomic-scale roughness of HAR

channel sidewalls on the ion scattering. For this purpose, we performed molecular dynamics (MD) simulations [43, 94, 95] to obtain angular distributions of ions scattered on smooth and rough Si and SiO_2 surfaces at grazing incidence. Quantitative information on such scattered or reflected ions can be used to predict the profile evolution of HAR channels in RIE processes [96–106].

2.2 MD Simulation

MD simulation was used to simulate the scattering of Ar^+, neon (Ne^+), and xenon (Xe^+) ions on a 4.3 nm x 4.3 nm Si surface or 4.2 nm x 4.2 nm SiO_2 surface. Two types of surface morphology were defined for each material: (1) pristine or smooth surface; and (2) rough surface wherein the roughness was artificially created by placing around 1 nm-high protrusions on the surface, as shown in Fig. 2.1. The horizontal size of each protrusion is also about 1 nm x 1 nm.

The modeled roughness was selected to be sufficiently smaller than the typical roughness of etched structures but slightly larger than atomic scales. For example, figures of the sidewall striations in HAR etching of hole channels with a diameter of 100 nm reported by Omura *et al.* [83] indicate that such roughness is over 10 nm in height. The line edge roughness (LER) of Si fin structures reported by Dixit *et al.* [107] is around 4 nm. The goal of this study is to clarify the effects of roughness smaller than "observable" roughness (e.g., about 10 % of the minimum dimension of the structure to be etched) on ion scattering. This is because, in typical profile simulation models, such observable roughness can be directly modeled as part of the surface structures that reflect incident ions in certain directions. Effects of surface roughness smaller than the size of such an observable surface structure may appear as distributed angles of scattered ions around the specular angle. In this study, we attempt to understand such angular distributions of scattered ions on seemingly flat Si or SiO_2 surfaces as functions of the small-scale surface roughness and incident ion species.

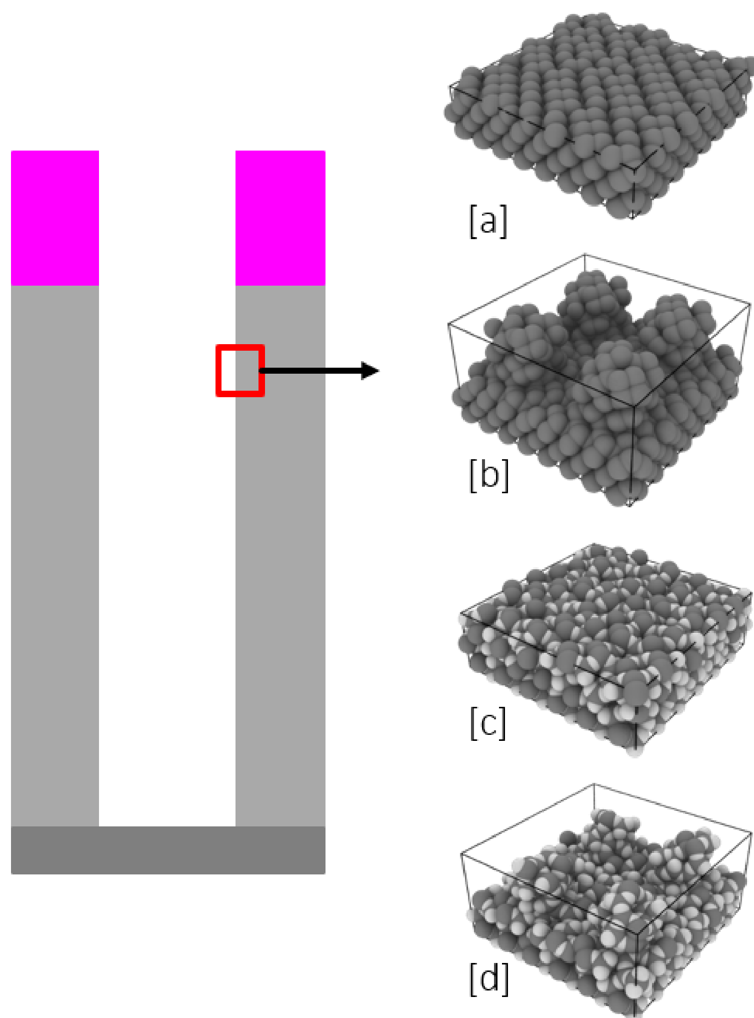

FIGURE 2.1: Atomic-scale surface models used in the MD simulations of this study. Here (a) and (b) represent smooth and rough crystalline Si surfaces and (c) and (d) represent smooth and rough SiO_2 surfaces. To model the scattering phenomena of incident ions on the sidewall of a HAR channel (as schematically depicted on the left), the top surfaces of (a)-(d) represent small areas of the nearly vertical sidewall surfaces of the HAR channel, into which energetic ions are at grazing incidence. The depth of each surface model here is depicted as relatively thin but, in MD simulations of high-energy ion impact, sufficiently thick surface models were employed, as discussed in the main text. The orientation of the top Si surface of (a) is (100).

The atomic interactions among Si and O atoms used in this study given by Stillinger-Weber potential functions [48, 49, 108], as discussed in Refs. 45, 109, 110. All interactions with nobles gases (Ar, Ne, and Xe) were described by the Moliére repulsive pair potential [42, 45]. Though the injected particles were referred to as ions, the MD code treated the injected ions as fast neutrals based on the assumption that incident ions would be neutralized near the surface [73, 74]. The scattering simulation code used in this study had

been extensively used in previous studies of plasma etching and deposition simulations [53, 60, 63, 74, 111–117].

The model surface represents a part of the sidewall of a Si or SiO_2 channel. Although the area that the model represents may be small compared with the deep trench or hole scale, it is assumed to be large enough on the atomic scale. Therefore, periodic boundary conditions were imposed in the horizontal directions of the model surface (i.e., the directions of the sidewall surface). The depth of the model surface is taken to be sufficiently deep and the positions of the atoms in the bottom layer were fixed to prevent the downward drift of the surface model during the simulation. If the incident ion or a recoiled atom of the material reaches the bottom layer of the surface model during the simulation, additional layers of the same material were added to the surface model from the bottom, making the depth of the surface model theoretically infinite. In our simulation, the initial surface model was in thermal equilibrium at 300 K.

In actual etching processes to form HAR 3D NAND channels through a stacked film of dozens – or even over a hundred – of pairs of thin SiO_2/silicon nitride (SiN) or SiO_2/polycrystalline Si layers, [81, 84, 117] reactive ions and charge-neutral radicals generated in fluorocarbon or hydrofluorocarbon plasmas are used with masks made of carbon-based materials [38, 118–122]. However, this study used noble-gas species instead as injected ions to focus on simple physical scattering phenomena and removed possible effects of chemical reactions. It should be noted that Ne has an atomic mass close to those of C and F and Ar has a mass close to that of Cl, i.e., reactive species widely used in plasma processing.

The scattering phenomenon was simulated by injecting ions with an incident angle $\theta_{\rm i}$ and following the ion trajectories as the ions were scattered by the surface [86]. The reflection angle ($\theta_{\rm r}$) and azimuthal angle ($\phi_{\rm a}$), as defined in Fig. 2.2, of each reflected ion were recorded for analysis. The incident angle and the reflection angle are measured from

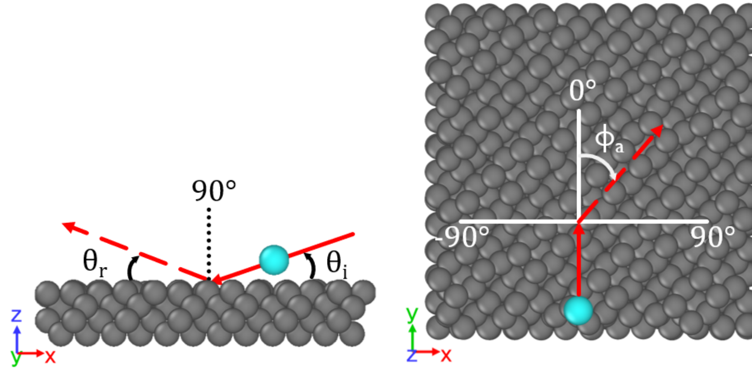

FIGURE 2.2: Definitions of the angles of incident and scattered ions relative to the surface normal and the direction of ion incidence. The side and top views of the surface model are given on the left and right. The blue sphere represents the incident ion and the broken lines and arrows represent the ion paths and their directions. The incident angle is θ_i, the reflection angle, i.e., angle of the reflected or scattered ion (or the corresponding charge-neutral atom after charge exchange on the surface) measured from the surface tangent is denoted as θ_r, and the azimuthal angle of the reflected ion is denoted as ϕ_a. Note that, for specular reflection, $\theta_r = 90° - \theta_i$ and $\phi_a = 0$.

the surface. The azimuthal angle of the reflected ion path is defined as the azimuthal angle around the axis normal to the surface at the location of impact.

As the simulation was performed to study the scattering on the sidewalls of HAR structures, the ions were initially injected at oblique angles from 5°– 20° with an ion energy (E_i) of 1,000 eV. Additional scattering simulations for Ar^+ with incident angles from 5°to 90° and ion energy of 100 eV were also performed to supplement the results.

In each ion-injection simulation cycle, an ion is injected into the clean initial surface with the predefined angle of incidence and kinetic energy. The initial position of the incident ion is slightly above the material surface and its horizontal position is randomly selected. The MD simulation of each ion injection cycle lasts for 2,000 fs. The simulation is performed under the microcanonical conditions, i.e., with the total energy being constant, for the first 300 fs. Subsequently, the system is gradually cooled by the Langevin thermostat [43, 57] for 1,600 fs and then by the Berendsen thermostat [58] for the remaining 100 fs, so that the material temperature is brought back to 300 K, i.e., the initial surface temperature, at the end of the ion-injection simulation cycle.

This ion injection cycle was repeated up to 10,000 times for statistical accuracy. In each injection cycle, the simulation is performed with the same initial surface given in Fig. 2.1 and no self-consistent change in the surface morphology due to the ion bombardment was considered. Because a reflected ion, if there is any, typically leaves the surface well before the cooling process starts (i.e., $t < 300$ fs with t being the simulation time in a single cycle.), the cooling process employed in the simulation is unlikely to affect the ion reflection properties examined in this study. However, the cooling process was performed to ensure that thermally desorbed ions (or the corresponding inert-gas atoms after charge neutralization) can be captured even if the injected ion is trapped in the material for an extended period. In the simulation, the injected ion is considered to be reflected when the z component of its velocity, v_z, is positive and escapes the surface at the end of the ion-injection cycle.

2.3 Results and Discussion

2.3.1 Angular distributions of reflected ions

We denote the probability of a reflected ion having kinetic energy E, reflection angle θ_r ($0° < \theta_r < 90°$), and the azimuthal angle ϕ_a ($-180° < \phi_a < 180°$) by $f(E, \theta_r, \phi_a)$ such that

$$\int_0^\infty dE \int_{0°}^{90°} d\theta_r \int_{-180°}^{180°} d\phi_a \;\; f\left(E, \theta_r, \phi_a\right) = 1 \quad .$$

Due to the system symmetry, we have $f(E, \theta_r, \phi_a) = f(E, \theta_r, -\phi_a)$.

The reflection-angle distribution $F(\theta_r)$ is defined as

$$F(\theta_r) = \frac{N_r}{N_{in}} \int_0^\infty dE \int_{-180°}^{180°} d\phi_a \;\; f\left(E, \theta_r, \phi_a\right) \quad ,$$

where N_r and N_{in} denote the number of incident ions reflected on the surface and the number of incident ions. It should be noted that incident ions may be trapped in the

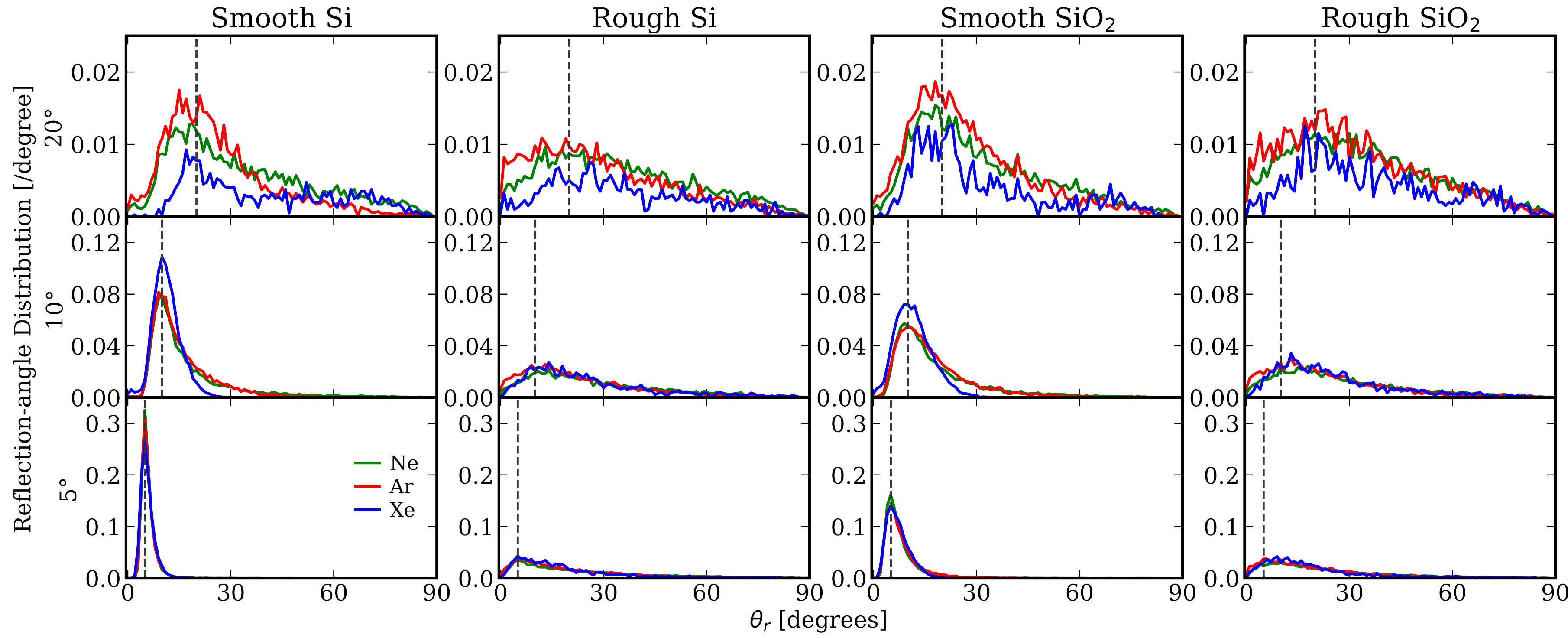

FIGURE 2.3: Reflection-angle distributions $F(\theta_r)$ of Ne^+ (green), Ar^+ (red) and Xe^+ (blue) ions reflected on the smooth and rough Si and SiO_2 surfaces defined in Fig. 2.1. The ion incident energy is 1,000 eV and angles of incidence are 5°, 10° and 20°. The vertical black dashed line indicates the specular angle in θ_r. At 5°and 10°, the curves for Ar and Ne nearly overlap. Note that incident ions may be trapped in the material.

material and the integral of $F(\theta_r)$ over the entire reflection-angle domain represents the ion reflection probability. The reflection-angle distributions for 1,000 eV noble-gas ion incidence on the smooth and rough Si and SiO_2 surfaces of Fig. 2.1 are plotted in Fig. 2.3.

For the smooth surface, the specular reflection is likely to take place. Indeed the reflection-angle distributions peaked at 5° and 10° on smooth Si and SiO_2 surfaces for all incident ion species examined here when the incident angles were 5° and 10°. Regardless of the incident ionic species or surface conditions, the reflection-angle distribution broadens with a decreasing ion incident angle. For a smaller incidence angle (i.e., an angle closer to the normal incidence), the incident ion is more likely to penetrate the material, rather than to be scattered on the material surface.

It is seen that the reflection-angle distribution on SiO_2 is broader than that on the Si surfaces under the otherwise same conditions. This can be attributed to the fact that the smooth SiO_2 surface has a small measure of roughness in comparison to the nearly perfectly smooth crystalline Si surface at 300 K. Introducing a 1 nm surface roughness to both Si and SiO_2 further broadens the θ_r distributions. Additionally, a narrower θ_r distribution for Xe^+ ion incidence was observed in comparison to those for Ar^+ or Ne^+ ion incidence due to the much larger mass of Xe. At the same kinetic energy, a heavier ion has a higher momentum and its path is less likely to be disturbed by the collision with lighter Si atoms.

The azimuthal-angle distribution $G(\phi_a)$, which is defined as

$$G(\phi_a) = \frac{N_r}{N_{in}} \int_0^{\infty} dE \int_{0^\circ}^{90^\circ} d\theta_r \;\; f\left(E, \theta_r, \phi_a\right) \quad ,$$

of reflected ions for 1,000 eV noble-gas ion incidence on the smooth and rough Si and SiO_2 surfaces are plotted in Fig. 2.4. It is seen that all azimuthal-angle distributions peak at $\phi_\mathrm{a} = 0$, i.e., the direction of forward scattering. It should be noted that $|\phi_a| < 90^\circ$ indicates the forward scattering. It is seen that, at an incident angle of 20°, a relatively large number

of Ne^+ and Ar^+ ions may result in backward scattering (i.e., $|\phi_a| > 90°$). In general, the larger the angle of incidence (i.e., the smaller the grazing angle) becomes, the narrower the azimuthal-angle distribution becomes. This is consistent with the observation of $F(\theta_r)$ above that, at a lower angle of incidence, the reflection is more specular. It is also seen in Fig. 2.4 that the rougher the surface is, the wider the azimuthal-angle distribution becomes. The ion mass effect is also seen; the azimuthal-angle distribution of Xe^+ ions is narrower than that of Ar^+ or Ne^+ ions. The heavier mass of an ion and therefore the higher momentum that the ion carries minimizes the deflection of the ion path when it hits a rough surface.

The mean kinetic energy $\overline{E}$ of reflected ions is defined by

$$\overline{E} = \int_0^\infty dE \int_{0°}^{90°} d\theta_r \int_{-180°}^{180°} d\phi_a \;\; E\, f\left(E, \theta_r, \phi_a\right) \quad .$$

The mean kinetic energies of reflected ions from the smooth and rough surfaces of Si and SiO_2 are plotted as functions of the ion incident angle in Fig. 2.5. The incident ion energy is 1,000 eV. The mean kinetic energy of reflected ions is seen to increase with the increasing incident angle in all cases. Especially at 5° on the smooth surface, the energy loss is relatively small since the interaction time is limited between the ion at grazing incidence and surface atoms. In general, lighter ions tend to lose less energy than heavier ions when they are reflected. Furthermore, ions reflected on the smooth surface tend to lose less energy than those reflected on the rough surface because incident ions tend to collide with a larger number of surface atoms when they are reflected on the rough surface. However, it is seen that, at 20°, the kinetic energies of reflected Xe^+ ions are less affected by the surface roughness probably because, even on the smooth surface, they tend to penetrate the material more deeply than in the cases of larger incident angles and interact with surface atoms for a more extended period.

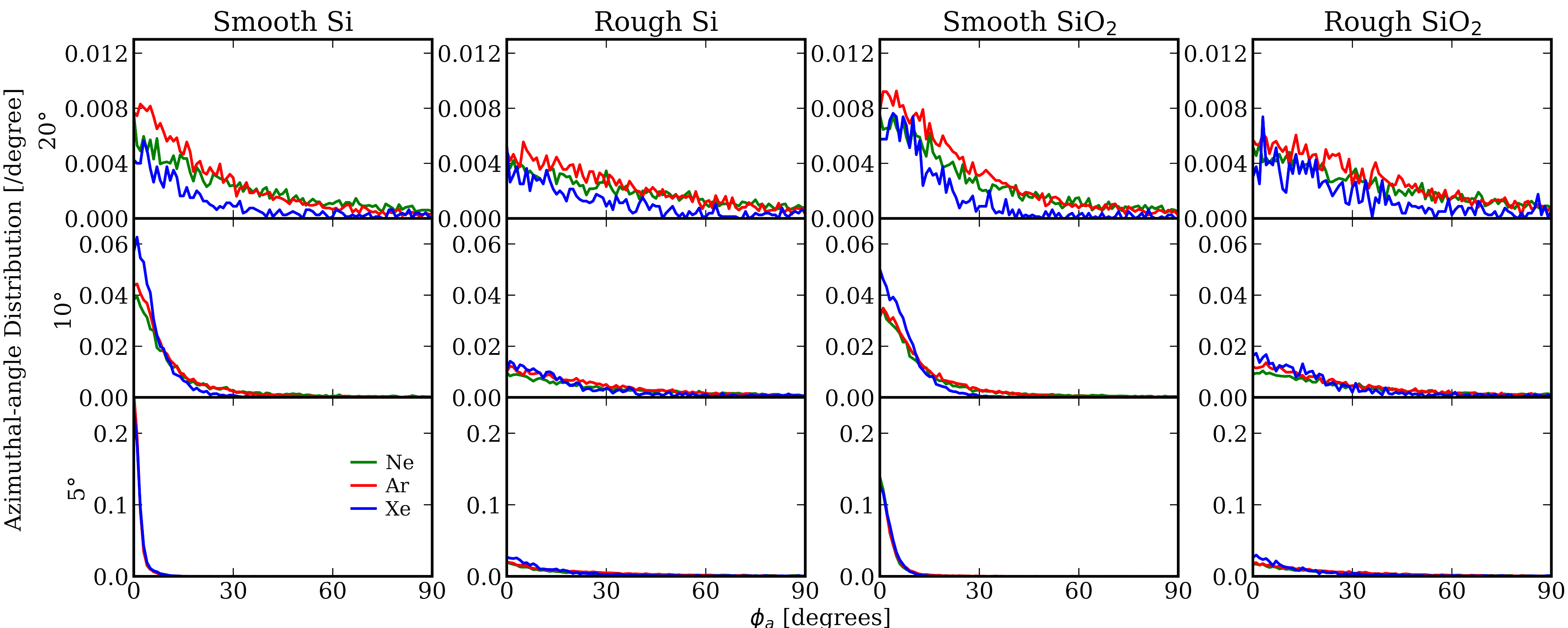

FIGURE 2.4: Azimuthal-angle distributions $G(\phi_a)$ of Ne^+ (green), Ar^+ (red) and Xe^+ (blue) ions reflected on the smooth and rough Si and SiO_2 surfaces defined in Fig. 2.1. The ion incident energy is 1,000 eV and angles of incidence are 5°, 10° and 20°. Because of the symmetry $G(\phi_a) = G(-\phi_a)$, $G(\phi_a)$ is plotted only for positive ϕ_a. The angle of $\phi_a = 0$ is the direction of specular reflection and $|\phi_a| < 90°$ indicates the forward scattering. It is seen that, at an incident angle of 20°, Ne^+ and Ar^+ ion incidence may result in backward scattering (i.e., $|\phi_a| > 90°$). At 5°and 10°, the curves for Ar and Ne nearly overlap. Note that incident ions may be trapped in the material.

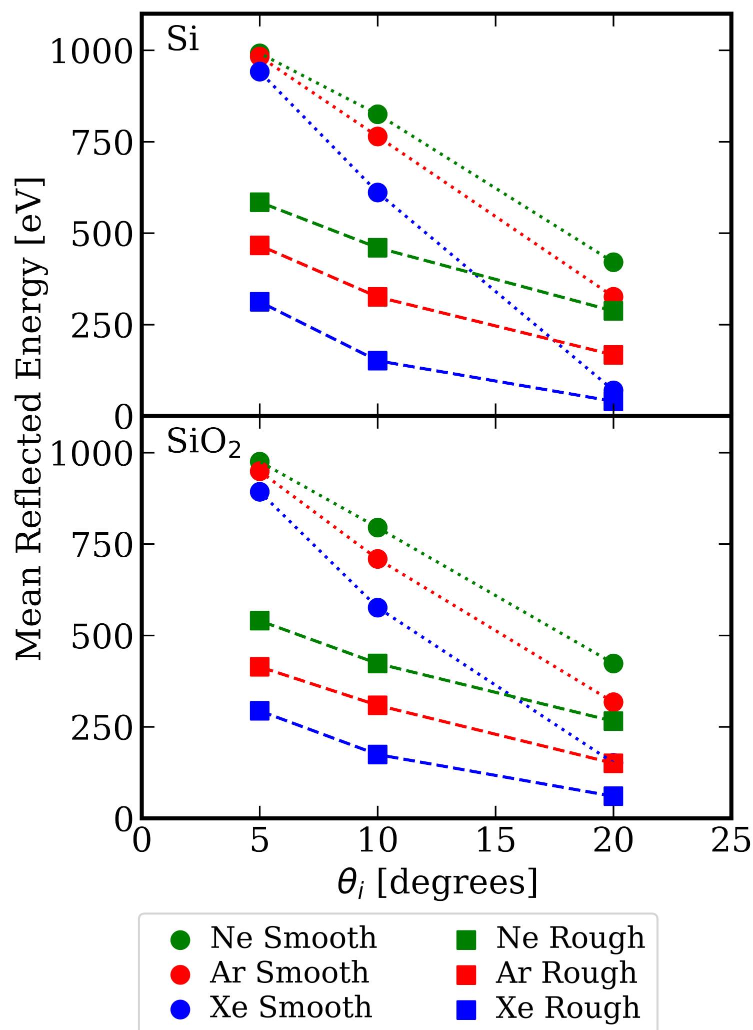

FIGURE 2.5: Mean kinetic energies of Ne^{+} (green), Ar^{+} (red), and Xe^{+} (blue) ions reflected on smooth (represented by circles) and rough (squares) Si and SiO_2 surfaces defined in Fig. 2.1, as functions of the angle of incidence. The ion incident energy is 1,000 eV.

2.3.2 Reflection probabilities

The reflection probability is defined as the ratio of the number of reflected ions to the total number of injected ions. The reflection probabilities of injected inert-gas ions are plotted as functions of the incident angle in Fig. 2.6, where the incident ion energy is 1,000 eV. It is seen that, at a lower incident angle of 5°or 10°, all ions have similar or nearly the same reflection probabilities on each surface and the surface roughness somewhat decreased the reflection probabilities. However, at 20°, the surface roughness hardly affected the reflection probabilities and the reflection probabilities are significantly lower than those

at lower angles. This is because, at 1,000 eV incident energy with an incident angle of 20°, significant sputtering takes place and incident ions are more likely to be embedded in the surface material.

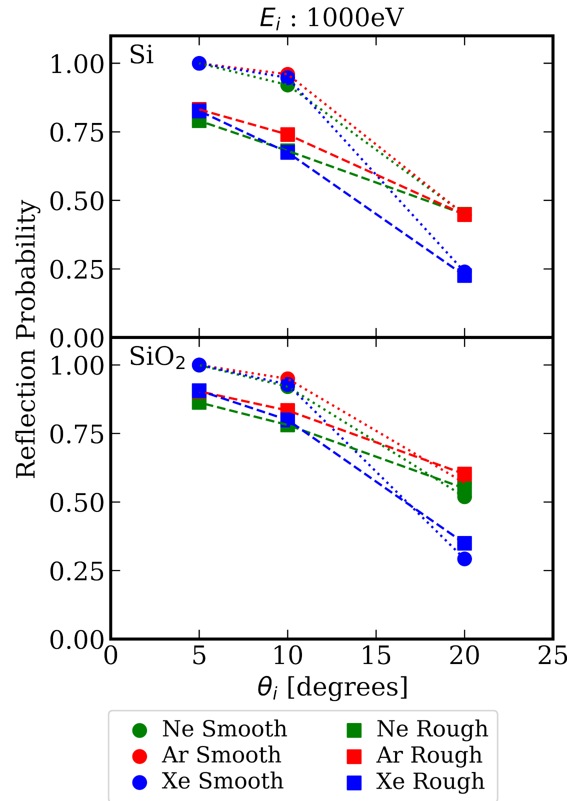

FIGURE 2.6: Reflection probabilities of Ne^+ (green), Ar^+ (red), and Xe^+ (blue) ions reflected on smooth (represented by circles) and rough (squares) Si and SiO_2 surfaces defined in Fig. 2.1, as functions of the angle of incidence. The ion incident energy is 1,000 eV. The data for Ne^+ and Ar^+ ions at 20° for the smooth and rough Si surfaces overlap. Similarly the data for Ne^+ and Ar^+ ions at 20° for the smooth and rough SiO_2 surfaces nearly overlap. At low incident angle (i.e., 5° or 10°), all ions have the same or similar reflection probabilities for each surface. The dotted and dashed lines are guides for the eye.

The reflection probabilities of low-energy injected inert-gas ions are plotted as functions of the incident angle in Fig. 2.7 for comparison, where the incident ion energy is 100 eV. It is seen that, at the oblique incident angles examined here, the reflection probabilities of all ions are near unity regardless of the surface conditions. This is because the incident energy is too small for the incident ions to penetrate the material. The reflection-angle and azimuthal-angle distributions for 100eV noble-gas ion on smooth and rough Si and SiO_2 surfaces are shown in Appendix A.

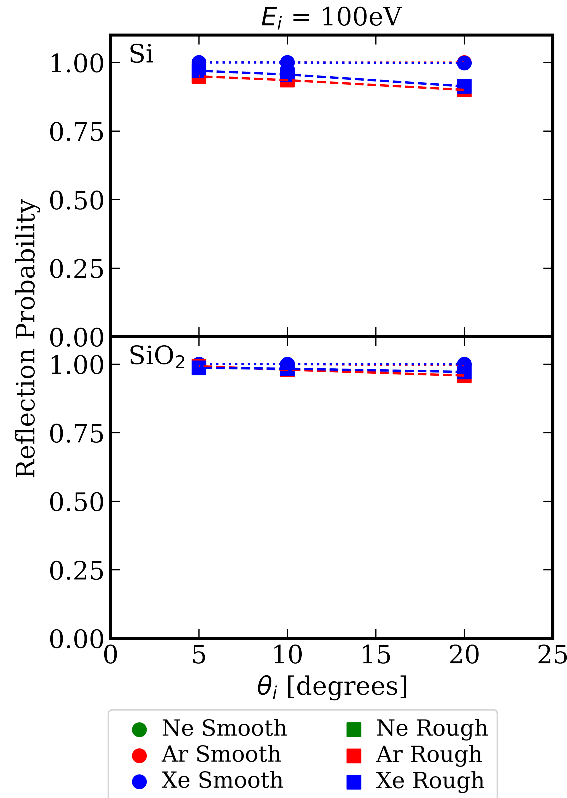

FIGURE 2.7: Reflection probabilities of Ne^+ (green), Ar^+ (red), and Xe^+ (blue) ions reflected on smooth (represented by circles) and rough (squares) Si and SiO_2 surfaces defined in Fig. 2.1, as functions of the angle of incidence. The ion incident energy is 100 eV. The reflection probabilities of all ions on each smooth surface overlap and are nearly unity. The reflection probabilities of all ions reflected on each rough surface also nearly overlap. The dotted and dashed lines are guides for the eye.

It should be noted that such reflection of low-energy incident ions on a material surface typically results from their multi-body collisions with the tightly bonded surface atoms. For example, Fig. 2.8 shows the reflection probabilities of Ne^+, Ar^+, and Xe^+ ions reflected on a smooth Si surface as functions of the angle of incidence, obtained from MD and "Stopping and Range of Ions in Matter" (SRIM) [123–126] simulations. SRIM is a binary-collision-based simulator for atomic motions. MD simulation results are the same as those in Figs. 2.6 and 2.7 with Ar^+ data being extended to 90°. It is seen that the reflection probabilities obtained from SRIM are nearly the same between the cases of 100 eV and 1,000 eV ion incident energies. Furthermore, the reflection probabilities obtained from SRIM are significantly lower than those from MD simulations, especially at low incident energy or large incident angles. This is because, in SRIM, the incident

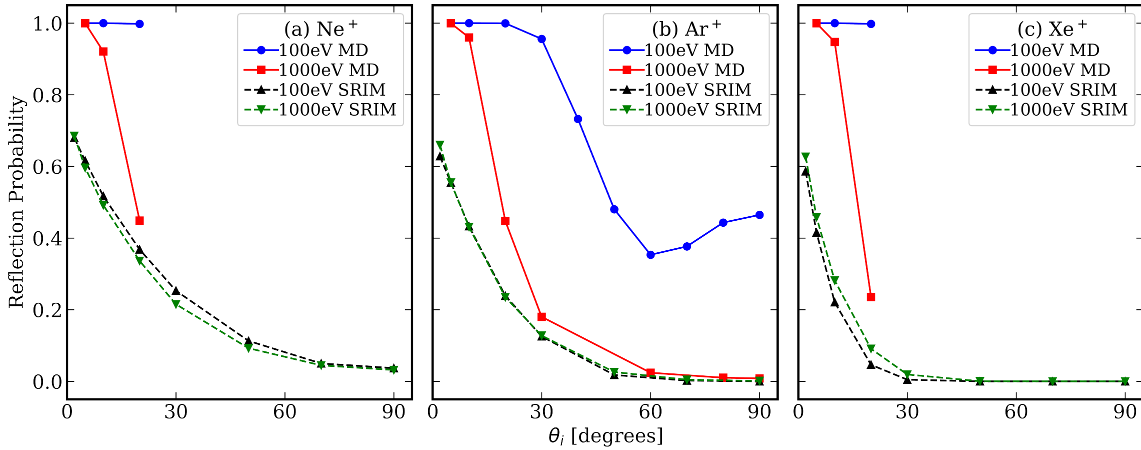

FIGURE 2.8: Reflection probabilities of (a) Ne^+, (b) Ar^+, and (c) Xe^+ ions reflected on a smooth Si surface as functions of the angle of incidence, obtained from MD and SRIM simulations with ion incident energies of 100 and 1,000 eV. MD simulation results are the same as those in Figs. 2.6 and 2.7 with Ar^+ data being extended to 0°. The obtained reflection probabilities are seen to differ significantly between MD and SRIM simulations, especially at low incident energy or large incident angles. In each case, SRIM data at 100 eV and 1,000 eV nearly overlap. As discussed in the main text, the MD simulation results are considered to be more reliable than the SRIM simulation results.

ion only interacts with a single atom on the surface with which it is about to collide and does not interact with other neighboring atoms on the surface simultaneously. Therefore, the incident ion in SRIM simulations does not "see" the surface, i.e., an array of tightly bonded atoms, and it penetrates the material unless it makes a backward scattering with this collision. On the other hand, MD simulation can handle multi-body collisions and, therefore, the incident ion interacts with multiple atoms on the surface simultaneously, which may collectively prevent the incident ion from penetrating the material. The binary collision assumption for ion injection into a material is typically valid only when the colliding atom has sufficiently high kinetic energy. For this reason, the MD simulation is considered to represent the surface collision and reflection processes more accurately than the SRIM simulation.

2.4 Conclusions

Molecular dynamics simulation of the scattering of Ne^+, Ar^+, and Xe^+ ions at grazing incidence (i.e., with the angle of incidence $\leq 20°$) on smooth and rough Si and SiO_2 surfaces were performed to evaluate their scattering properties. The ion incident energy used in this study was 1,000 eV in most cases. The study was motivated to understand how energetic ions interact with the sidewalls of HAR channels when they hit the sidewalls at grazing incidence during RIE processes to form such channels. In RIE processes, incident ions are typically reactive ions such as fluorocarbon ions. However, in this work, we limited our interest to inert-gas ions to focus on the effects caused by physical impact.

It is found from the MD simulations that the angular distributions of reflected ions broaden more when the ion mass is lower, the incident angle is closer to the normal incidence, or the surface is rougher. The mean kinetic energy of reflected ions increases with the ion incident angle. Especially when the surface is smooth, the ion mass is low, or the incident ion grazing angle is small, the mean kinetic energy of reflected ions becomes close to the incident ion energy and the reflection becomes nearly specular. The surface roughness reduces the mean kinetic energy of reflected ions, especially at grazing incidence. In general, a crystalline Si surface is smoother than a typical smooth SiO_2 surface at the atomic level. Therefore, on a smooth crystalline Si surface, the angular distribution of reflected ions is slightly less broad and the mean kinetic energy of reflected ions is slightly higher than those on a smooth SiO_2 surface. The reflection probability also increases as the angle of incidence increases. Especially, the reflection probabilities of all ions examined in this study scattered on a flat surface are close to unity at an ion incident angle of 5°. When the incident ion energy is as low as 100 eV, the reflection probabilities of all incident ions are close to unity as the incident ions do not have enough energy to penetrate the material.

The reflection probabilities evaluated with SRIM simulations are typically much smaller than those obtained from MD simulations. Because SRIM is based on a binary collision

model, the incident ion in SRIM simulation interacts only with a single atom on the material surface and cannot be repelled collectively by the surrounding surface atoms even if its incident kinetic energy is not sufficient to pass through the narrow interatomic space of the material surface.

It should be noted that all data obtained in this study were those on the surfaces defined in Fig. 2.2; the surface morphologies and other conditions were not modified self-consistently by the incident ion impact for the sake of simplicity. For practical applications of our interest, i.e., scattering of chemically reactive incident ions such as fluorocarbon ions on sidewall surfaces of HAR channels, the surfaces are modified by not only the incident-ion impact but also the redeposition of chemically reactive species arriving from the plasma or other areas of the sidewalls as sputtered or desorbed species. The present study is the first step toward a more comprehensive understanding of such complex scattering phenomena of chemically reactive species.

Chapter 3

Molecular Dynamics Simulation of Oxide-Nitride Bilayer Etching with Energetic Fluorocarbon Ions

3.1 Introduction

The 3D NAND flash memory technology emerged when the scaling of planar NAND devices can no longer address the demand for larger memory storage [6]. The idea behind 3D NAND devices is to stack memory cells vertically to increase the memory density per area. There are various 3D NAND structures developed in the industry today such as the Terabit Cell Array Transistor (TCAT) and the Bit-Cost Scalable (BiCS). The fabrication of 3D NAND devices starts with the deposition of alternating thin films on the substrate. The types of deposited films depend on the design of the device; for example, a multi-layer stack of alternating silicon dioxide (SiO_2) and silicon nitride (SiN) layers is known as an ONON layer. The number of deposited layers in such a stack determines the memory capacity of the fabricated 3D NAND devices [6]. After the formation of a multi-layer stack, the next process is high-aspect-ratio (HAR) etching to form deep holes through

the stack. The HAR etching is preceded by the deposition of a hard mask patterned with holes to allow the etching of deep hole channels [17]. The purpose of HAR etching is to create hole channels with smooth and straight sidewall profiles. The HAR etching is the main roadblock in 3D NAND device fabrication due to the increasing difficulty in maintaining ideal hole channel profiles and avoiding issues, e.g., bowing, tapering, twisting, and incomplete etch, with increasing aspect ratios [24]. The goal of this study is to understand the fundamental properties of the ONON layer etching by energetic reactive ions. Reactive ion etching (RIE), i.e. etching of materials by energetic ion impact combined with surface chemical reactions [20, 80] is used for HAR etching in the fabrication of 3D NAND devices. Energetic ions used for RIE are typically generated in chemically reactive plasmas [27, 28, 76–79]. To achieve this goal, we use molecular dynamics (MD) simulation [94, 95, 127] to study the interaction of incident chemically reactive ions with surface atoms.

Fluorocarbon or carbon fluoride (CF) plasmas are typically used in SiO_2 and SiN etching. It has been known that CF-containing surface-material layers (which we call "mixing layers") are formed on the material surface during such etching processes and can facilitate surface etching reactions by forming silicon fluorides (SiF_x) and other volatile molecular species. For example, with MD simulations, Abrams and Graves showed MD simulation results of Si etching by CF_3^+ ($\leq$ 200eV) ions wherein a fluorocarbosilyl layer forms on the Si surface [128]. Smirnov et al. showed that SiO_2 etching proceeded with and without CF-polymer layer formation by low-energy ions [129]. Rauf et al. demonstrated MD simulation of layer-by-layer etching of Si and SiO_2 by fluorocarbon and Ar^+ ions [130]. Miyake et al. found that the electronegativity of fluorine (F), which weakens the carbon (C) –carbon bond and strengthens the carbon-fluorine bond of C–C–F or C=C–F structures strongly affects the nature of polymer deposition and, therefore, the formation of the mixing layer during etching [60].

Mass-selected ion beam experiments have been used to characterize the etching properties of SiO_2, SiN, and other materials [38]. For example, Karahashi et al. presented

the sputtering yields of SiO_2 by F^+ and fluorocarbon ions as functions of the incident ion energy [119] and Yanai et al. presented those of SiN [120]. Ito et al. examined hydrogen effects in CF-based etching of SiN [121].

In this study, we focus on the etching of SiO_2 and SiN by ${CF_3}^+$ ions with a high energy range (up to 2000eV). Specifically, we are interested in the etching of a SiO_2 and SiN (ON) bilayer, which represents a part of the ONON multilayer used in 3D NAND devices, and how the etch rate changes as the etch front passes the bilayer interface. From such simulations, we aim to understand how the multi-layer structure can affect the final etched profiles of HAR deep holes.

3.2 Methodology

In this study, we employed classical MD simulation to study the RIE of SiO_2, SiN, and SiO_2-SiN bilayers by ${CF_3}^+$ ions at various incident ion energies ranging from 200eV to 2000eV. In classical MD, Newton's equations of motion are numerically integrated to determine the orbits of all atoms in the system [94, 127]. The interatomic potential functions that we used for this study atoms are based on Stillinger-Weber potentials [48, 49] which were modified to include all necessary two-body and three-body interactions for the Si-O-N-C-F system. The modified potentials have been used in earlier studies [45, 53, 60–72].

The model of a SiO_2 film (Fig. 3.1a) was created by placing Si and O atoms to form a pseudo cristobalite structure [74] in a rectangular box with a surface area of 17.5nm^2 (4.19nm x 4.19nm). The initial depth was set to optimize the computational time, depending on the incident energy of ions injected into the film, e.g., 3.49nm for 200eV to 5.58nm for 2000eV. The periodic boundary conditions were imposed in the horizontal directions, such that the model represented an infinitely wide thin layer of a SiO_2 film. The model of a SiN film was also formed similarly with a stoichiometry of

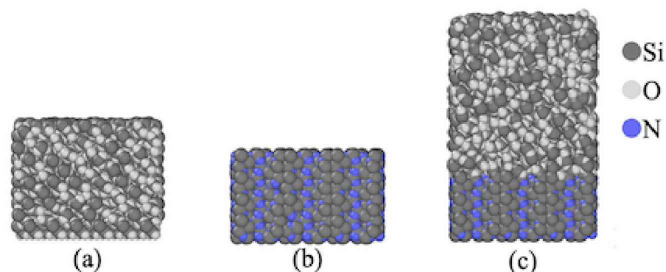

FIGURE 3.1: Sideview images of the (a) SiO_2, (b) SiN, and (c) oxide-nitride bilayer model surface materials. In (c), it should be noted that the bottom nitride layer is assumed to be infinitely thick. As the etching simulation proceeds, more materials are added from the bottom.

Si_3N_4 (Fig. 3.1b) by placing Si and N atoms in a rectangular box with a surface area of 15.7nm^2 (4.04nm x 3.88nm) and an initial depth of 2.25nm. The periodic boundary conditions were also imposed in the horizontal directions. Both SiO_2 and SiN films were then thermalized at 300K.

The model of a SiO_2-SiN bilayer (Fig. 3.1c), which we referred to as an ON bilayer, was then created by placing a 4.85nm thick SiO_2 on top of a 2.25nm thick SiN layer with a stoichiometry of Si_3N_4 in a rectangular simulation box with a surface area of 15.7nm^2 (4.04nm x 3.88nm). These layers are thinner than those typically used in 3D NAND ONON structures [14], to enable MD simulations with reasonable computation times. The periodic boundary conditions were imposed in the horizontal directions. The SiO_2 layer was originally formed on a surface area of 4.19nm x 4.19nm, as discussed above, and then placed in the rectangular simulation with a bottom area of 4.04nm x 3.88nm, with slight compression in the horizontal directions initially. The ON bilayer model film was then thermalized at 300K for 10ps, resulting in a film with a total depth of 6.63nm.

The atoms of the bottom 2 mono layers of each model film were fixed in position (which we call an anchor layer) to prevent a downward drift of the model film during the simulation of ion injection. During the simulation, an additional material layer was added to the model film from the bottom when the film was deemed to be too thin. The atoms in the anchor layer before the addition of the bottom material layer also served as the binding sites for the atoms of the added layer and were then allowed to

move according to the interatomic forces. The new anchor layer was then created at the bottom of the added new layer. The model film was deemed too thin when incident ions and/or knocked-on material atoms reach the region near the anchor layer, or the thermal energy of the material becomes higher than the predetermined value after an ion injection. This is because the model film to be etched by ion impact has to be sufficiently wide and deep, such that the momentum and energy transferred from an injected ion are transported unimpeded by phonons and thermal conduction away from the position of impact. Whenever a new bottom layer is added during simulation, the entire film model was again thermalized at 300K.

The etching simulation consists of a series of injection cycles. Each injection cycle begins by injecting a CF_3^+ ion at normal incidence into a random horizontal position on the material surface with predetermined kinetic energy. In our MD simulation, as in earlier studies of MD simulation of etching, we do not consider the electrical charges of ions as part of interatomic forces and treat energetic ions as the corresponding neutral species having the same kinetic energies. This is because we assume that charged species are neutralized on the surface by the Auger effect at the moment of impact. To save simulation time, the ion is injected from a position just above the material surface where the incident ion is not interacting with surface atoms. Typically, in each injection cycle, we inject only a single CF_3^+ ion.

Each injection cycle is typically 2000fs long. For the first 300fs, the total system (i.e., material surface and the injected ion) is allowed to evolve under the microcanonical (NVE) conditions, where the number of all atoms, the simulation volume, and the total energy of the system are conserved. In this period, the kinetic energy transfer from the ion to the material and the subsequent collision cascade occur. The positions and velocities of the atoms are calculated using the velocity-Verlet algorithm [131, 132] with a variable timestep of 0.2 – 0.5fs. The timestep is varied depending on the fastest calculated velocity and selected to be small enough for good conservation of the total energy of the system. Following the 300fs NVE conditions, the system is artificially cooled to

300K by gradually decreasing the velocity of all atoms for 1600fs using the Langevin thermostat [57] and for 100s using the Berendsen thermostat [58, 59]. This artificial cooling represents the process of energy dissipation in the system. Because we use a small model surface material, the total energy is conserved under the NVE conditions. In reality, the surface is much wider and deeper, so all energy and momentum transfer from the incident ion to the surface material is transported and dissipates from the position of impact to the outer region, so the material around the location of impact cools down gradually until it is subject to another ion impact. For a small area used for our simulation, it typically takes microseconds to milliseconds for the next ion to hit the same area. In our simulation, we shortened this slow cooling or thermal relaxation period to 1700fs to achieve computational efficiency.

At the end of a single injection cycle, all atoms that are above the surface and not bonded with the surface atoms are removed as desorbed species. The etching yield or sputtering yield of a specific species (such as Si), i.e., the average number of the desorbed or reflected species by a single ion impact, is evaluated from the number of such desorbed species. After the removal of desorbed species, a new injection cycle starts using the ion irradiated material surface of the present cycle. In this way, the time evolution of the surface conditions during the etching process is also self-consistently simulated. For typical etching simulations, the injection cycles are repeated for thousands of cycles, such that statistical averages of physical quantities of our concern (such as etching yields) can be taken and compared with experimentally observed values of the corresponding quantities. Unless otherwise specified, we continue the simulations until the system reaches steady state, where the averaged etching yields of all atomic species and surface conditions no longer change as the ion dose increases.

3.3 Results and Discussions

3.3.1 Etching of SiO_2 and SiN

MD simulations of the etching of SiO_2 and SiN model surfaces by ${CF_3}^+$ ions were performed to evaluate the etching yields and the formation of CF-containing mixing layers. Here we define the etching yield for each species, e.g., Si, O, C, and F in the case of SiO_2 etching by ${CF_3}^+$ ions, more specifically as the average number of removed or reflected atoms from the surface per ion injection. In the case of SiO_2 etching by ${CF_3}^+$ ions, if the system is in steady state, the etching yields of Si and O are positive and those of C and F are 1 and 3 so that no accumulation of C or F atoms occurs on the surface.

Figure 3.2 shows the instantaneous etching yields of (a) SiO_2 and (c) SiN by 500eV ${CF_3}^+$ ions for all atomic species of the systems and the corresponding changes in depth for (b) SiO_2 and (d) SiN as functions of the ion dose obtained from MD simulations with the model surfaces of Fig. 3.1(a) and (b). The angle of ion incidence is normal to the film surface. Here the instantaneous etching yield is defined as the running average of the removed or reflected atoms from the surface over 50 ion injections into the model material surface. The steady-state etching is seen to be attained after 0.5x10^{16} ions/cm^2, wherein the average removed C and F corresponds to the numbers of injected atoms per cycle, i.e., 1 and 3. Furthermore, we define the “etch rate” of the surface material as the etched depth per unit ion dose, i.e., the slope of the etched surface position as a function of the ion dose, as shown in Fig. 3.2(b) and (d).

The etching yields of SiO_2 and SiN for Si atoms obtained from MD simulation are plotted as functions of the ion incident energy in Fig. 3.3. The etching yields are evaluated in steady state. For comparison, etching yields of SiO_2 [119] and SiN [120] by ${CF_3}^+$ ions obtained from ion beam experiments are also shown in Fig. 3.3. It is seen that the simulation and experiment yields are in good agreement for both SiO_2 and SiN, which corroborates the relevance of the interatomic potential functions used in this study.

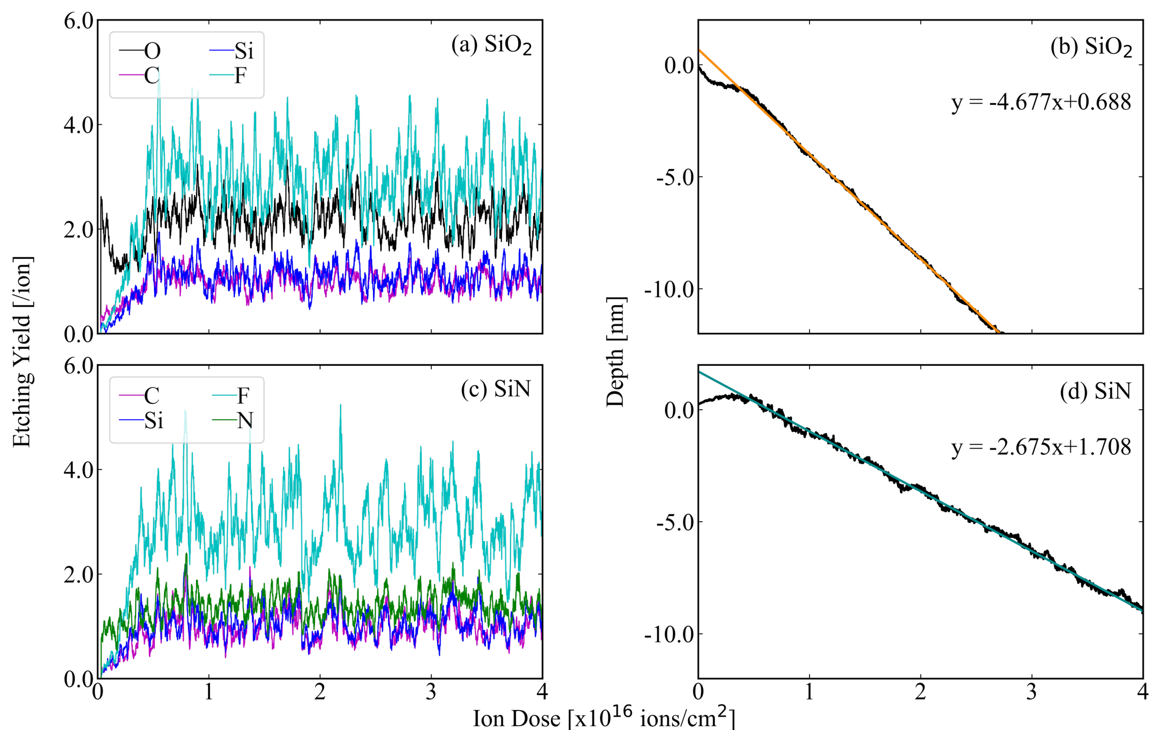

FIGURE 3.2: Instantaneous etching yields (a) SiO_2 and (c) SiN by 500eV CF_3^+ ions for all atomic species of the systems and the corresponding changes in depth for (b) SiO_2 and (d) SiN as functions of the ion dose obtained from MD simulations. The angle of ion incidence is normal to the film surface.

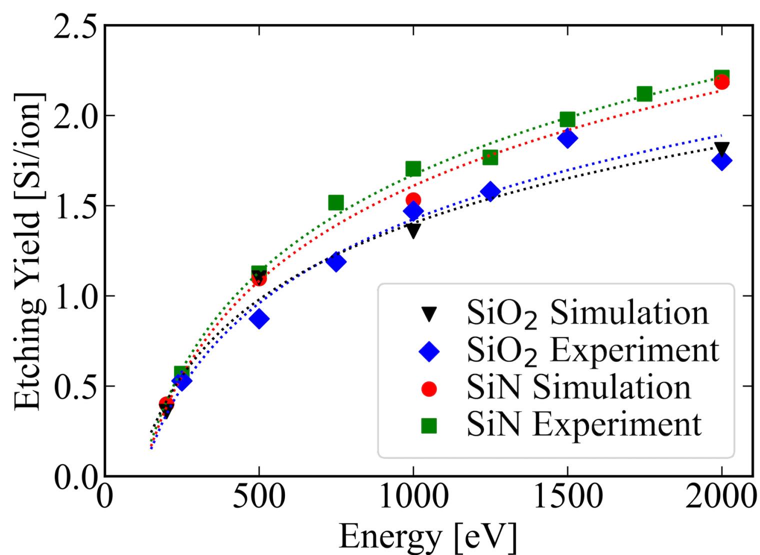

FIGURE 3.3: The etching yields of SiO_2 and SiN in steady state for Si atoms by CF_3^+ ions as functions of incident ion energy obtained from MD simulations and ion beam experiments. The experimental yield values are taken from Ref. 119 for SiO_2 and Ref. 120 for SiN.

The etch rates of SiO_2 and SiN obtained from MD simulations are also plotted as functions of the ion incident energy in Fig. 3.4. It is seen that the etch rate for SiO_2 is higher than that of SiN even though Fig. 3.3 shows that the Si etching yield of SiN is higher than that of SiO_2. This is because the atomic density of SiN is higher than that of SiO_2; it is required to remove more Si atoms to etch the same thickness of SiN as SiO_2.

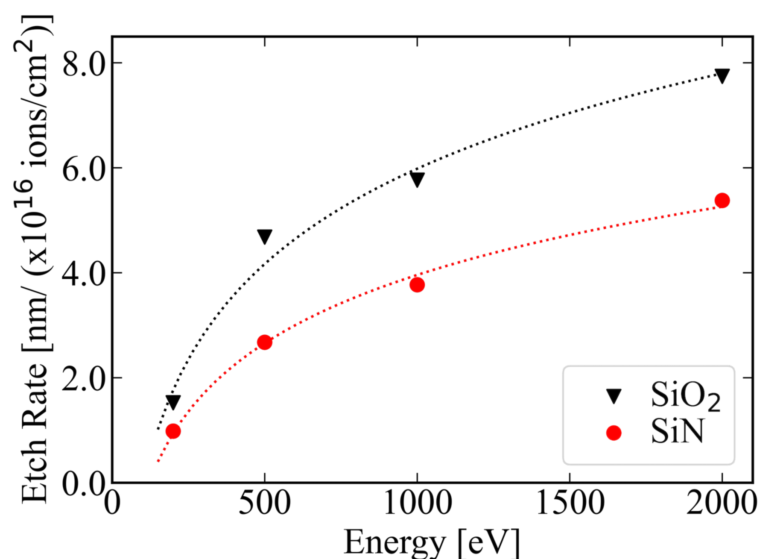

FIGURE 3.4: The etch rates as functions of the ion energy for the etching of SiO_2 and SiN by CF_3^+ ion irradiation obtained from MD simulation. The etch rate is defined here as the etched depth per unit ion dose and given in units of nm/(10^{16} ions/cm^2).

Figure 3.5 shows the depth profiles of atomic densities of SiO_2 (a) – (d) and SiN (e) – (h) etched by CF_3^+ ion irradiation at an ion dose of 4.0x10^{16} ions/cm^2 for both materials. The depth is measured from the position of the top surface of the model material before etching. Note that the scales of vertical axes of Fig. 3.5 are not the same among different depth profiles. It is seen that much of C and F is deposited near the top surface. This layer, where C and F atoms coexist with surface Si and O or N atoms, is the mixing layer, as stated earlier. In this layer, chemical reactions take place during the etching process, which may facilitate the etching of SiO_2 and SiN by forming volatile species. It is seen in Fig. 3.5 that the mixing layer is typically a few nanometers thick, and its thickness varies with the ion incident energy and surface material. It is observed that the densities of accumulated C and F atoms in SiO_2 and SiN decrease with increasing ion energy. This

is because, at sufficiently high incident ion energy, the etching of the material surface supersedes the deposition of C and F atoms. Especially at 200eV, as seen in Fig. 3.5 (a) and (e), the C and F densities near the top surface are much higher than the Si and O or N densities, indicating the deposition of a CF polymer layer on top of the SiO_2 or SiN surface. At higher ion energies, however, CF polymer is hardly seen, especially in SiO_2, as the density of C atoms remaining in the surface region decreases with the increasing ion energy.

In contrast to the densities, the thickness of the mixing layer increases with increasing ion energy. This is because, the higher the energy is, the deeper the ions can penetrate. The mixing layer thicknesses in SiO_2 and SiN at the onset of steady-state etching measured at ion doses of $0.57 \text{x} 10^{16}$ ions/cm^2 and $0.64 \text{x} 10^{16}$ ions/cm^2, respectively, are plotted as functions of the ion energy in Fig. 3.6.

Figure 3.7 and 3.8 show the depth profiles of bond densities of SiO_2 and SiN respectively etched by CF_3^+ ion irradiation at an ion dose of $4.0 \text{x} 10^{16}$ ions/cm^2 for both materials. The bond density profiles correspond to the atomic density profiles in Fig. 3.5. Bonds whose densities are negligibly small such as carbon-carbon double bonds (C=C) are not plotted here. It is observed in Fig. 3.7(a) that, at 200eV, the deposited C and F atoms on SiO_2 are comprised primarily of those of C-F, C-C, C-O, and Si-F bonds. The dominance of the C-C and C-F bonds near the top of the surface shows the formation of a CF polymer layer there. As the ion energy increases further, the C-C and C-F bond densities decrease, which is consistent with the low C densities at such high ion energies observed in Fig. 3.5. At such high energies, deposited F atoms are mostly bonded with Si atoms.

The results for SiN are similar to those for SiO_2 except that more C tends to remain in SiN than in SiO_2, especially at higher energies, as we saw in Fig. 3.5. In SiN, the Si-C bond density increases with the increasing ion energy whereas, in SiO_2, it decreases with the increasing ion energy beyond 500eV.

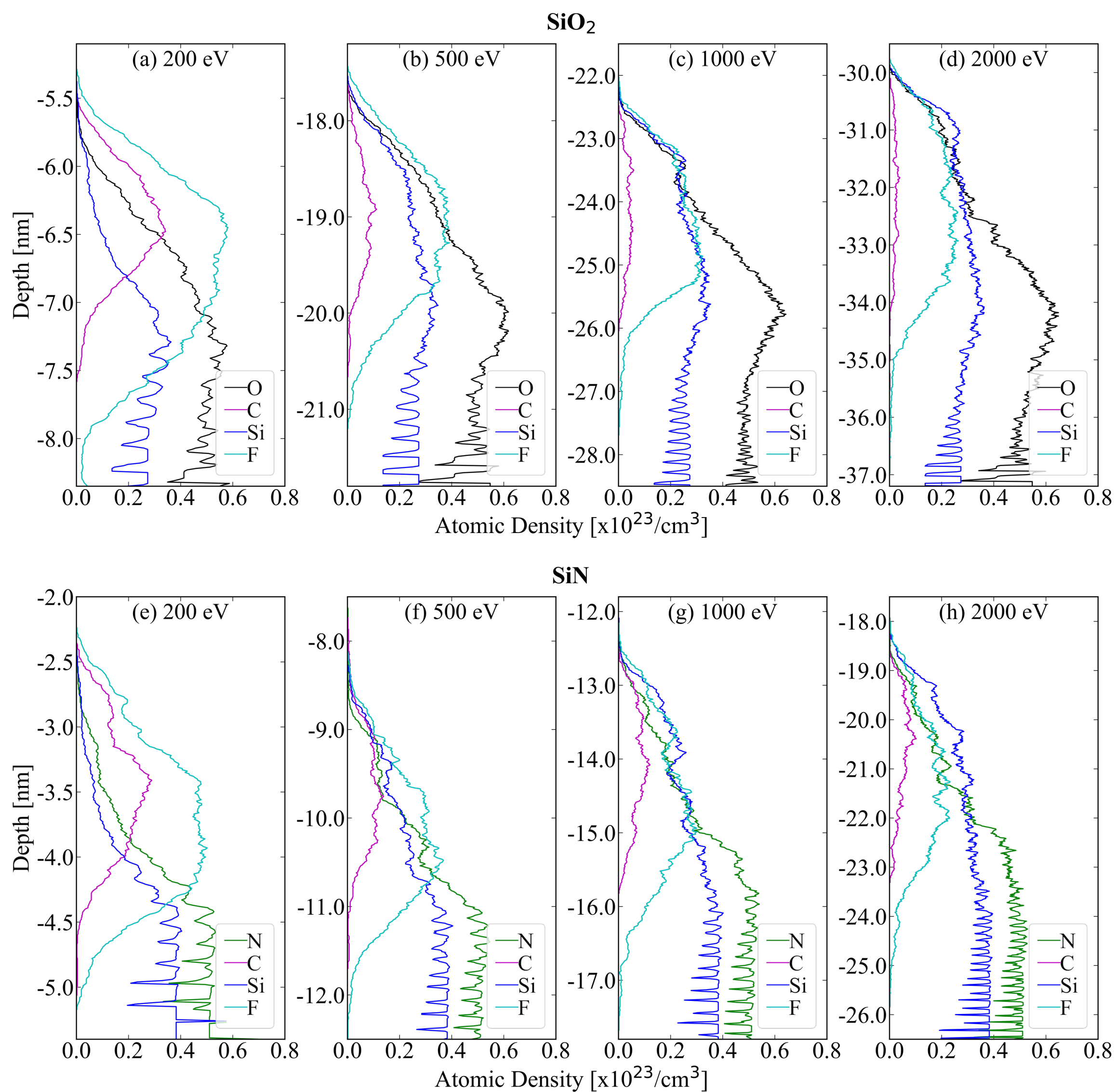

FIGURE 3.5: The depth profiles of atomic densities during steady-state etching of (a) – (d) SiO_2 and (e) – (h) SiN by CF_3^+ ion irradiation with incident energies of 200eV, 500eV, 1000eV, and 2000eV, obtained from MD simulation. The depth profiles were taken at an ion dose of $4.0\text{x}10^{16}$ ions/cm^2 for both SiO_2 and SiN. The origin of the vertical axis is the position of the material's top surface prior to etching. Note the scale and position of the vertical axis vary among different profiles. Except for the absolute values of the depth, the relative positions of the atomic density profiles and their shapes hardly change during steady-state etching.

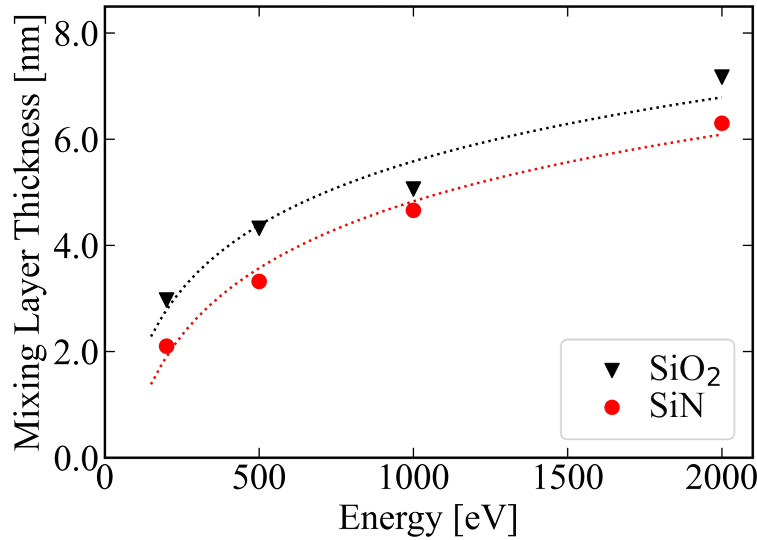

FIGURE 3.6: The mixing layer thicknesses as functions of the ion energy for SiO_2 and SiN etched by CF_3^+ ion irradiation with incident energies of 200eV, 500eV, 1000eV, and 2000eV, obtained from MD simulation. The thickness was measured from the depth profiles at the onset of steady state etching, i.e., at the ion dose of 0.57×10^{16} ions/cm^2 for SiO_2 and 0.64×10^{16} ions/cm^2 for SiN.

As seen in Fig. 3.5(a) – (d), the O density near the top surface decreases with the increasing incident ion energy and becomes close to the Si density, indicating preferential sputtering of O from the SiO_2 surface. This is consistent with the increase of the Si-Si bond density in SiO_2 as the incident ion energy increases. Similarly, as seen in Fig. 3.5(e) – (h), the N density near the top surface decreases with the increasing incident ion energy and becomes close to or even lower than the Si density, indicating preferential sputtering of N from the SiN surface. This is also consistent with the increase of the Si-Si bond density in SiN as the incident ion energy increases.

The desorbed species or etched products of the SiO_2 and SiN model materials by CF_3^+ ion etching were also studied. From the desorbed species, we could infer the surface chemical reactions that occur during etching. The number of specific species removed from the surface per ion injection is counted and normalized by the total number of all removed species per ion injection. These ratios of all desorbed species accumulated up to a dosage of 4.0×10^{16} ions/cm^2 for both SiO_2 and SiN are plotted as percentages in Fig. 3.9. Here the dominant desorbed species under some conditions are explicitly listed

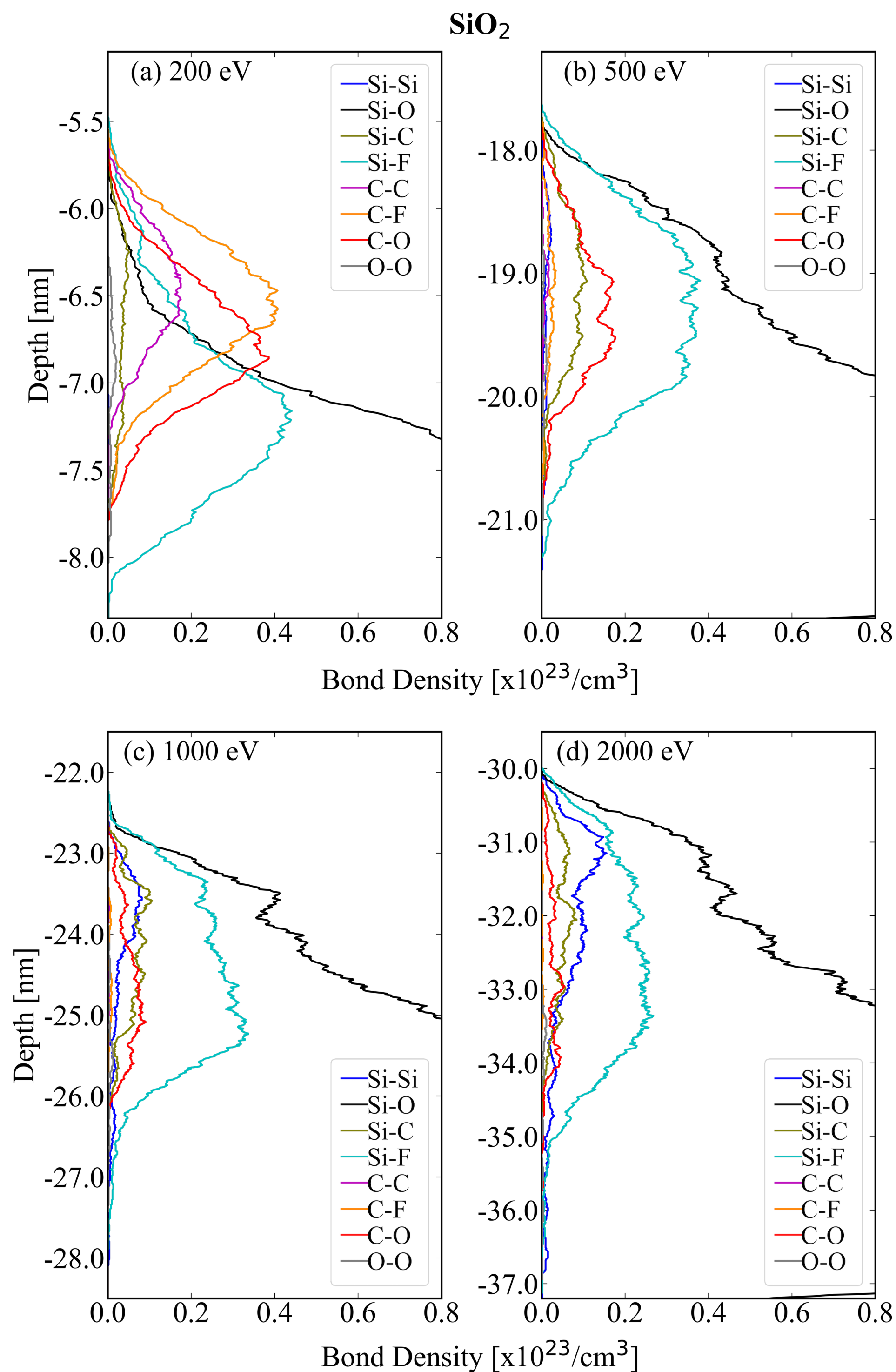

FIGURE 3.7: The depth profiles of bond densities during steady-state etching of SiO_2 by CF_3^+ ion irradiation with incident energies of (a) 200eV, (b) 500eV, (c) 1000eV, and (d) 2000eV, obtained from MD simulation. The bond depth profiles were taken at an ion dose of 4.0x10^{16} ions/cm^2 and the origin of the vertical axis is the position of the material's top surface prior to etching, as in Fig. 3.5.

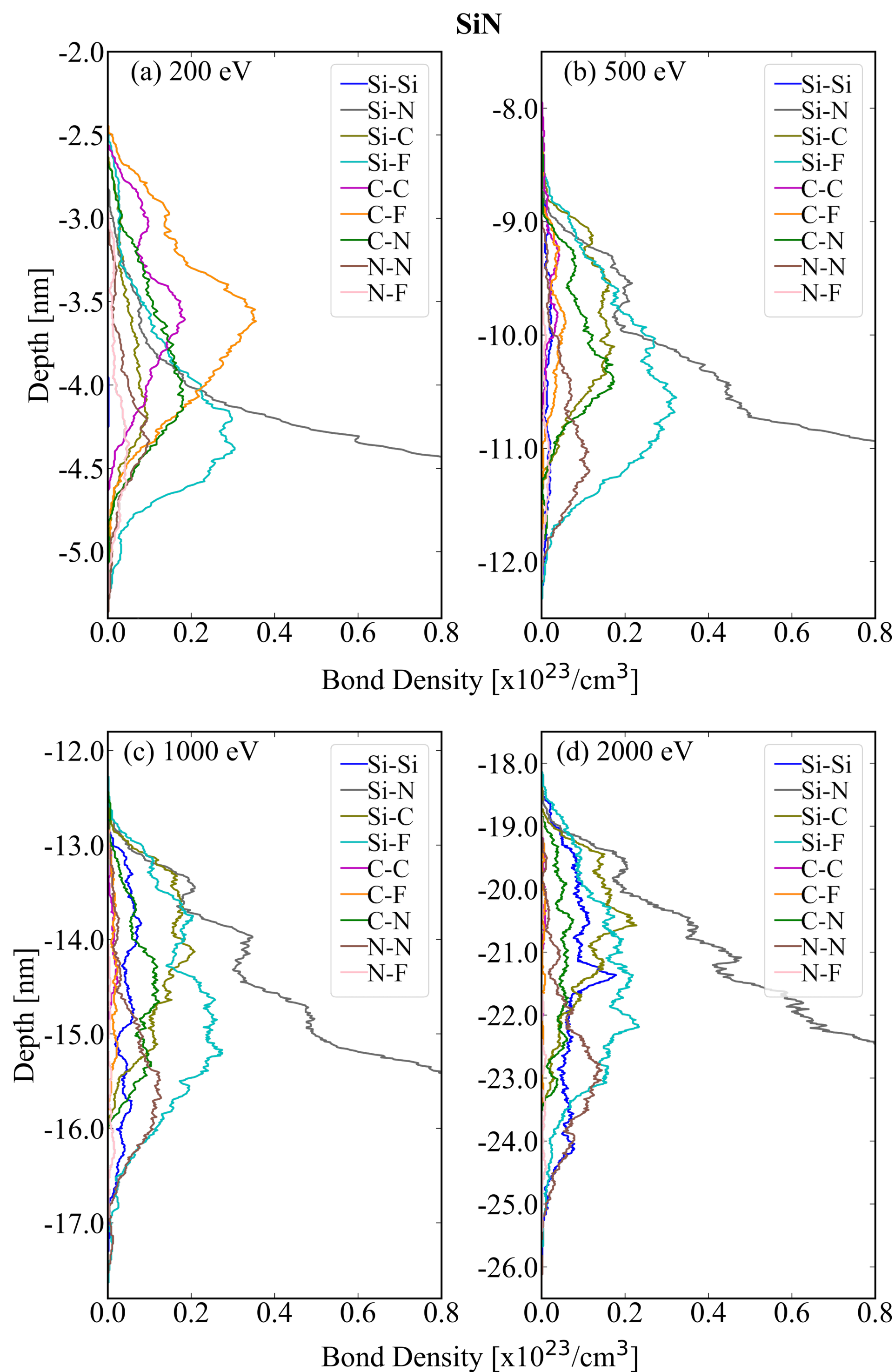

FIGURE 3.8: The depth profiles of bond densities during steady-state etching of SiN by CF_3^+ ion irradiation with incident energies of (a) 200eV, (b) 500eV, (c) 1000eV, and (d) 2000eV, obtained from MD simulation. The bond depth profiles were taken at an ion dose of 4.0x10^{16} ions/cm^2 and the origin of the vertical axis is the position of the material's top surface prior to etching, as in Fig. 3.5.

while the species whose ratios are less than 3.2% under all conditions examined are listed as "others."

For the etching of SiO_2, Si atoms are primarily removed as monoatomic Si or SiF_x ($1 \leq x \leq 4$) while O atoms are primarily removed as monoatomic O, O_2, CO, or CO_2. It is observed that the desorption of Si, SiO, SiO_2, O, and O_2 increases with increasing ion energy. At 2000eV, 60% of the total desorbed species that contain atoms from the etched material (i.e., Si or O) are monoatomic species (i.e. atomic Si and O) and diatomic species (i.e. O_2, CO, and SiF). This suggests the dominance of physical sputtering at higher incident ion energies. However, it is also seen that the desorption of SiF_x ($1 \leq x \leq 4$), CO, and CO_2 increase up to 500eV and then decrease as the incident ion energy further increases. This observation is consistent with that of the beam study of SiO_2 etching with CF_3^+ ions by Toyoda et al., where the desorption of SiF_2 and CO increased with the increasing ion energy, though their study was limited to 400eV [133]. Among all desorbed species observed in the SiO2 etching simulation, volatile molecules, i.e., species with no dangling bonds, were O_2, F_2, OF_2, CO, CO_2, COF_2, CF_4, C_2F_2, C_2F_4, C_2F_6, and SiF_4, which may be considered "stable" or hardly redeposit (or redeposit with low sticking probabilities) when they interact with a material surface. In our simulation, such volatile molecules accounted for 32%, 34%, 29% and 26% of the total desorbed species for SiO_2 etched by 200eV, 500eV, 1000eV, and 2000eV CF_3^+ ions, respectively. All other desorbed species with dangle bonds are likely to deposit with high sticking probabilities if they interact with a material surface.

Additionally, among the desorbed SiF_x ($1 \leq x \leq 4$), at 200eV ion irradiation, the amount of desorbed species satisfies $SiF_4 > SiF_3 > SiF_2 > SiF$ while, at 2000eV, $SiF_4 < SiF_3 < SiF_2 < SiF$. Figure 3.7(a) shows that, at 200eV, the Si-F bond is concentrated just below the CF polymer layer. As Si atoms desorb through the polymer layer, the polymer layer may act as a steady source of F atoms and allows the desorbing Si atoms to be bonded with more F atoms. The presence of the CF polymer may also account for the fact that there are more sputtered or desorbed F, F_2, CF, and CF_2 species at

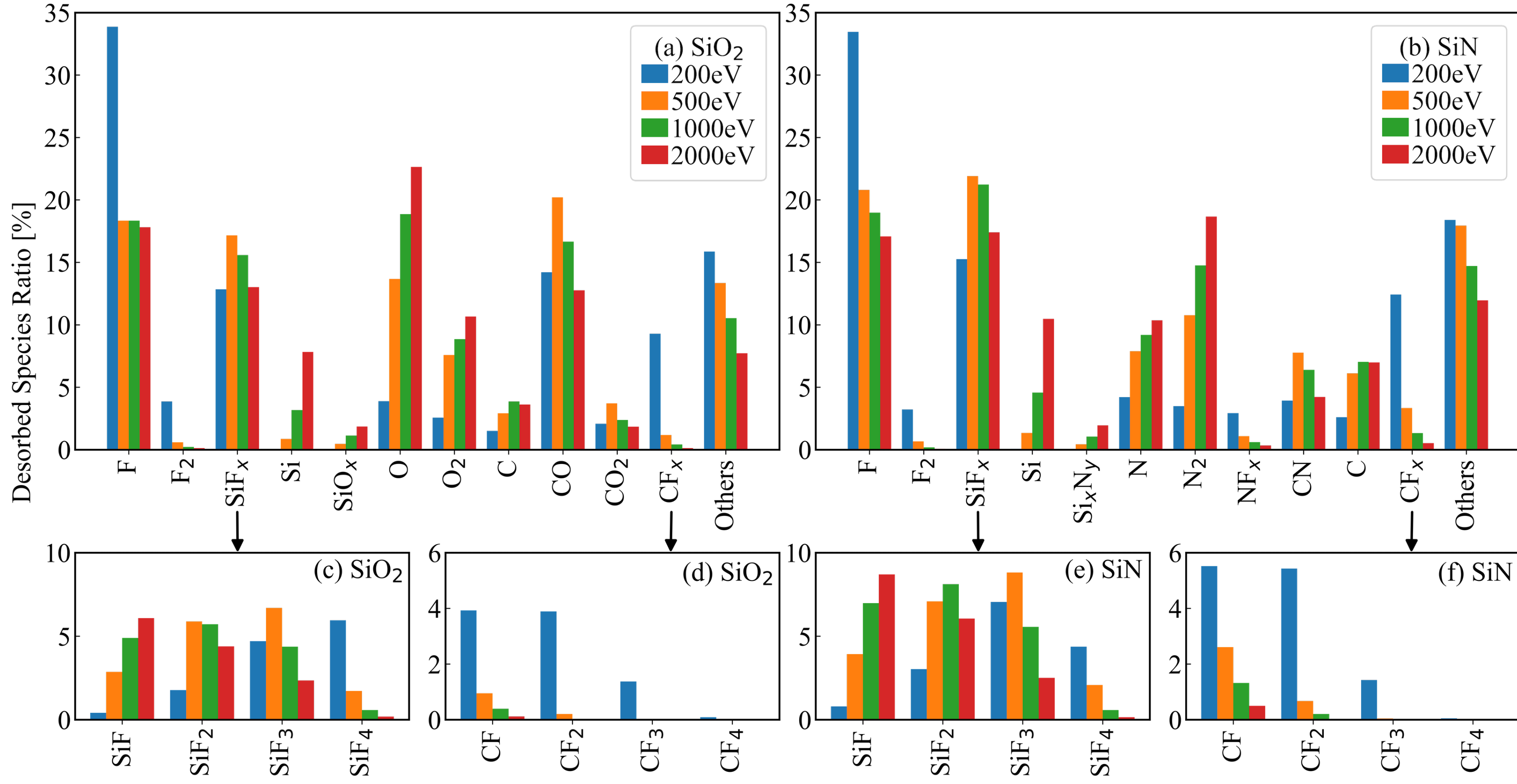

FIGURE 3.9: The ratios of desorbed species from (a) SiO_2 and (b) SiN surfaces etched by CF_3^+ ion irradiation with incident energies of 200eV, 500eV, 1000eV, and 2000eV, obtained from MD simulation. The ratios of desorbed SiF_x ($1 \leq x \leq 4$) species from (c) SiO_2 and (e) SiN, and desorbed CF_x ($1 \leq x \leq 4$) from (d) SiO_2 and (f) SiN are also plotted. The ratio of a specific desorbed species is defined as the total number of the specific desorbed species indicated in the horizontal axes divided by the total number of all desorbed species during the simulation.

200eV than at higher ion energies. This is also consistent with the study of Toyoda et al. showing that the desorption of CF_2 radicals decreases with the increasing ion energy [133]. As the ion energy increases from 500eV to 2000eV, the Si-F bond density (Fig. 3.7(b) – (d)) decreases. Specifically, at 500eV or higher energies, the C-F bonds hardly exist. Therefore, the desorption of highly fluorinated SiF_x and CF_x becomes less probable as the ion energy increases.

For the etching of SiN, Si atoms are primarily removed as monoatomic Si or SiF_x ($1 \leq x \leq 4$) while N atoms are primarily removed as monoatomic N, N_2, NF_x, ($1 \leq x \leq 3$), and CN. It is observed that the desorption Si, Si_xN_y ($1 \leq x \leq 3$, $1 \leq y \leq 4$), N, and N_2 increases with the increasing ion energy. Also at 2000eV, monoatomic species and diatomic species such as N, N_2, CN, Si, and SiF accounted for 52% of the total desorbed species. However, the desorption of SiF_x ($x \leq 4$) and CN increases up to 500eV but then decreases above 500eV while the desorption of NF_x ($x \leq 3$) decreases with the increasing ion energy. Among all desorbed species observed in the SiN etching simulation, volatile molecules (i.e., species without dangling bonds) were F_2, N_2, NF_3, CF_4, C_2F_2, C_2F_4, C_2F_6, and SiF_4, which accounted for 12%, 14%, 16%, and 19% of the total desorbed species for the ion energies of 200eV, 500eV, 1000eV and 2000eV ion energy, respectively. Unlike in the case of SiO_2 etching, the percentage of these species increases with increasing ion energy in the case of SiN etching. This increasing trend was primarily caused by the increasing amount of N_2 desorption with the increasing ion energy.

Similar to the case of SiO_2 etching, among the desorbed SiF_x ($1 \leq x \leq 4$), at 200eV ion irradiation, the amount of desorbed species satisfies $SiF_3 > SiF_4 > SiF_2 > SiF$ while, at 2000eV, $SiF > SiF_2 > SiF_3 > SiF_4$ for SiN etching. The desorption of F, F_2, CF, and CF_2 are also higher at 200eV than at higher ion energies for SiN etching. These facts indicate that the etching of SiN becomes more physical sputtering than chemical etching as the ion energy increases, as in the case of SiO_2.

3.3.2 Etching of an Oxide-Nitride Bilayer

3.3.2.1 Etching Yields and Etch Rates

MD simulation of the ON bilayer etching with CF_3^+ ions was performed to examine the etching process through a material interface. The instantaneous etching yields for all removed or reflected atomic species are plotted as functions of the ion dose in Fig. 3.10(a) – (d) and the corresponding changes in the position of the top surface are also plotted as functions of the ion dose in Fig. 3.10(e) – (h). The origin of the vertical axis of Fig. 3.10(e) – (h) represents the top surface position of the ON bilayer prior to etching. In Fig. 3.10(e) – (h), the location of the SiO_2 – SiN interface is indicated by the grey horizontal broken line, which was 4.85nm below the original top surface. The slopes of the orange and green solid lines indicate the steady state "etch rates" (i.e., etched depths per unit ion dose) of the SiO_2 and SiN model substrates by CF_3^+ ions at the corresponding ion incident energy. The ion dose at which the N atoms start to desorb is indicated by the green broken vertical line. The ion incident energy used for etching is indicated in each graph. As in the single material etching discussed above, the angle of ion incidence is normal to the surface. Additionally, the depth profiles of the atomic densities of the ON bilayer etched by CF_3^+ ions with ion energies of 200eV to 2000eV are plotted in Fig. 3.11(a) – (d). The depth profiles are plotted at the indicated ion dose. The horizontal dashed line indicates the position of the interface between SiO_2 and SiN.

In the case of 200eV ion injection, it is seen in Fig. 3.10(a) that steady-state etching is achieved prior to the etching of the underlying SiN layer, which is considered to occur when the non-zero etching yield of N atoms starts to appear at around an ion dose of 2.7×10^{16} ions/cm^2. The oxide etching may be considered to have reached the steady state when the average etching yields of C and F are close to 1 and 3, meaning no deposition of C and F atoms takes place, and the time-averaged etching yields of Si and O hardly change as functions of the ion dose. Figure 3.10(e) shows that the surface height went down slightly when the ion injection started. We observed that, during this very initial

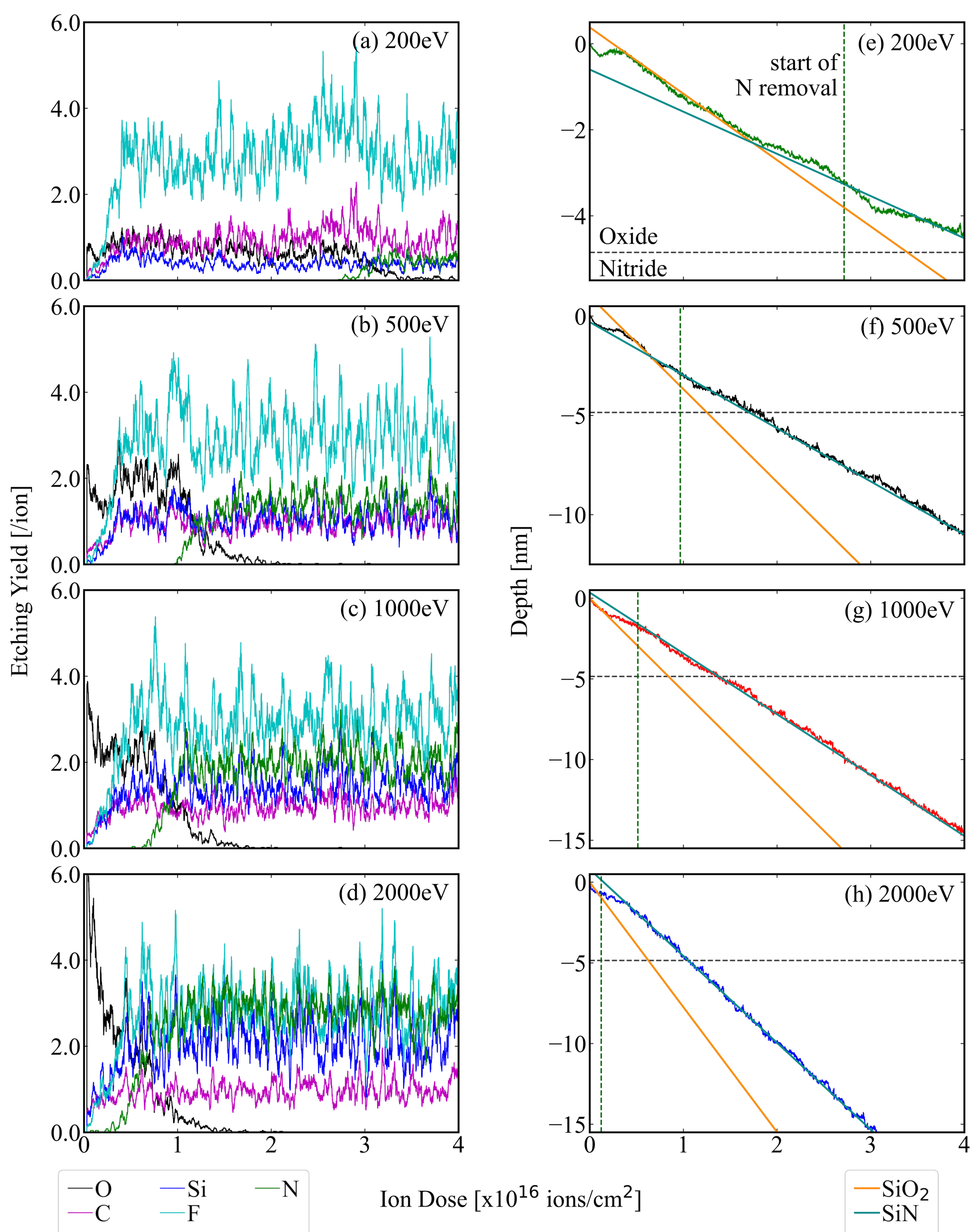

FIGURE 3.10: The instantaneous etching yield of each atomic species as a function of the ion dose for the ON bilayer etched by CF_3^+ ion irradiation with incident energies of (a) 200eV, (b) 500eV, (c) 1000eV and (d) 2000eV, and the corresponding change of the surface height (i.e., depth) as a function of ion dose with ion incident energies of (e) 200eV, (f) 500eV, (g) 1000eV and (h) 2000eV, obtained from MD simulation. In (e) – (h), the vertical dash line corresponds to the start of the removal of nitrogen, i.e., the start of etching of the underlying SiN.

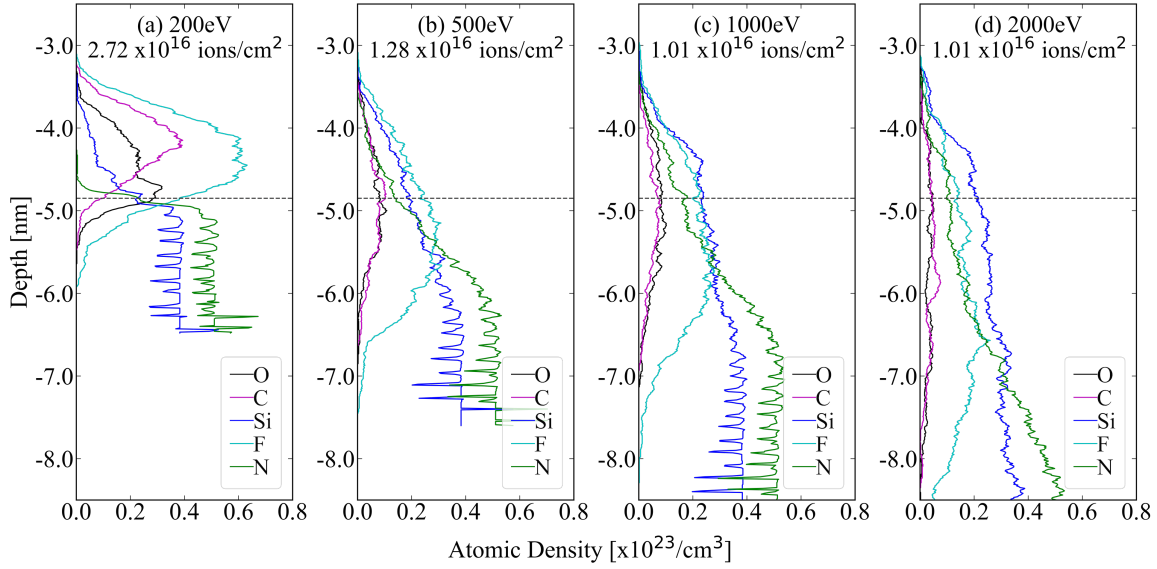

FIGURE 3.11: The depth profiles of the atomic densities for the etching of the ON bilayer by CF_3^+ ion irradiation with incident energies of (a) 200eV, (b) 500eV, (c) 1000eV and (d) 2000eV, obtained from MD simulation. The depth profiles were taken at the ion doses indicated at the top of the graphs. The origin of the vertical axis is the position of the material's top surface prior to etching. The horizontal dashed line indicates the position of the interface between SiO_2 and SiN.

phase, O atoms were preferentially removed from the SiO_2 surface, and therefore the volume of the model surface decreased initially. It is also seen in Fig. 3.10(a) that more O atoms were removed than Si atoms initially. Before the etching reached the steady state, C and F atoms are also seen to have accumulated, which formed the mixing layer. The accumulation of C and F atoms eventually increased the surface height until around an ion dose of about $0.4 \text{x} 10^{16}$ ions/cm^2, from which the surface height steadily decreased because of the SiO_2 etching. It is seen that the etch rate of the ON bilayer changes from that of SiO_2, as indicated by the orange line, to that of SiN, as indicated by the green line. This is because, at 200eV, the mixing layer thickness for pure SiO_2 (3.0nm, as seen in Fig. 3.6) is less than the thickness of the initial oxide layer (4.9nm). However, it should be noted the etch rate slowed down even when the ion beam was still etching the SiO_2 layer.

As seen in Fig. 3.10(b) and (f), in the case of 500eV ion injection, the steady-state etching of the oxide layer occurred after a short period of the mixing layer formation. However, the duration of the steady-state etching of SiO_2 was shorter than in the case

of 200eV ion injection, and the etch rate changed to that of pure SiN at around a dose of 0.97x10^{16} ions/cm^2. In this case, the mixing layer of pure SiO_2 for 500eV (4.3nm) was slightly less than the initial thickness of the SiO_2 layer.

As seen in Fig. 3.10(c) and (g), at 1000 eV, the underlying SiN layer was already being etched at a low dosage of 0.5x10^{16} ions/cm^2 as evidenced by the removed nitrogen seen in Fig. 3.10(c). In this case, the mixing layer of pure SiO_2 (5.1nm) was slightly thicker than the oxide layer thickness. As such, there was a mixing of the oxide and nitride layers from the very beginning. Once nitrogen started to be removed, even when less than half of the oxide layer was etched, the etch rate of the ON bilayer already followed that of pure SiN.

At 2000eV, as seen in Fig. 3.10(d), the underlying SiN layer is already etched at a low dose of 0.07x10^{16} ions/cm^2. Fig. 3.10(h) shows that the etch rate hardly followed that of pure SiO_2. Unlike in the 200eV case, the oxide and nitride layers were mixed well before the etch front reached the interface. The mixing of the oxide and nitride layers is evidenced by the depth profile of atomic densities shown in Fig. 3.11(d). It is seen that the O atoms reached about 4nm beyond the interface. Because the nitride layer is much thicker than the oxide layer, the etch rate immediately followed that of pure SiN even with a small amount of O present in the SiN layer.

The ON bilayer examined here has a thin SiO_2 layer over an infinitely thick SiN layer. Therefore, when the single etch rate appeared at sufficiently high ion incident energy, it was the etch rate of SiN. In the case of a multiple alternating SiO_2 and SiN layer, i.e., an ONON layer, the simulation results above suggest that, if the ONON layer is etched with sufficiently high ion energy, a single average etch rate between the etch rates of SiO_2 and SiN would appear, depending on the thicknesses of their layers. If the thicknesses of ONON multilayers are not uniform over the horizontal cross-sectional area of a HAR etched hole, a non-uniform etch rate over the etched-hole cross-section can appear, which

we speculate may cause a bending of the HAR etched hole as the etch front passes through dozens of multilayers.

3.3.2.2 Desorbed Species from the ON bilayer Etching

Figure 3.12 shows the accumulated desorbed species or etch products from a unit area of the ON bilayer etched by CF_3^+ ions as functions of the ion dose for various ion energies. Plotted in (a) are the most dominant O-containing desorbed species. The curves of O-containing desorbed species become flat once O atoms are depleted from the surface. It is seen that, with increasing ion energy, more oxygen was removed as O or O_2 while the desorbed amounts of CO and CO_2 decreased. Plotted in (b) are the most dominant N-containing desorbed species. Note that the scale of the vertical axis of (b) is much smaller than that of (a). As in (a), with increasing ion energy, more N and N_2 desorbed while the among of desorbed NF_x ($1 \leq x \leq 3$) decreased. The amounts of NF_2 and NF_3 were much smaller than that of NF for all ion energies examined here. At 2000eV, only NF appeared as desorbed species among NF_x. NO molecules desorbed at all energies but were much fewer than N, N_2, and NF. Plotted in (c) are the most dominant Si-containing desorbed species. It is seen that, with increasing ion energy, the removal of monoatomic Si increased while that of SiF_4 molecules decreased. It should be noted that the trends are opposite between the 200eV and 2000eV cases. In the case of 200eV, the desorbed amount of SiF_4 is the highest followed by those of SiF_x species with decreasing number x of bonded F atoms with the desorbed amount of monoatomic Si as the lowest. In contrast, in the case of 2000eV, the desorbed amount of the monoatomic Si is the highest followed by those of SiF_x species with the increasing number x of bonded F.

The trend observed in the desorbed species for the ON bilayer etching is similar to the trend of the desorbed species of individual SiO_2 and SiN. The main difference is the presence of NO among the desorbed species. In actual HAR deep hole etching, volatile species such as CO, CO_2, O_2, NF_3, and SiF_4, may leave the hole without sticking to the

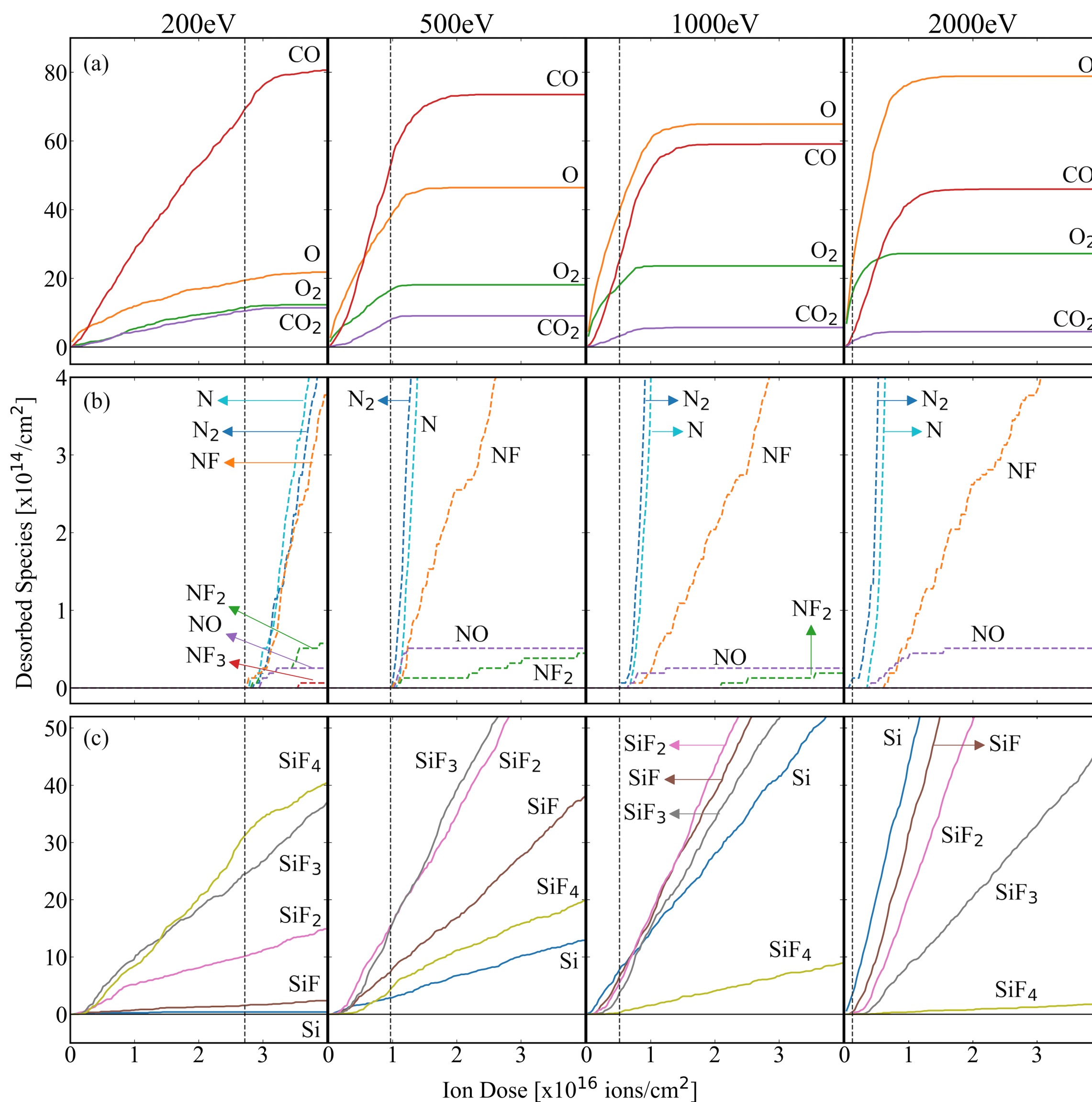

FIGURE 3.12: The accumulated numbers of desorbed species emitted from a unit area of the ON bilayer surface etched by CF_3^+ ion irradiation with incident energies of 200eV, 500eV, 1000eV, and 2000eV, obtained from MD simulation. The horizontal axis represents the ion dose. Only dominant species among (a) oxygen-containing desorbed species, (b) nitrogen-containing desorbed species, and (c) silicon-containing desorbed species are plotted. The vertical dash lines correspond to the start of the removal of nitrogen, i.e., start of etching of the underlying SiN.

wall whereas other desorbed species with dangling bonds such as O and SiF_x with $1 \leq x \leq 3$ may be redeposited on the sidewalls, which may cause tapering, as schematically illustrated in Fig. 3.13. However, this figure is not meant to imply that the redeposition is the sole cause of tapering. In reality, the flux of incident ions that reaches the bottom of a HAR channel as well as the transport of gas-phase radicals along the channel can also greatly affect the resulting profile of the HAR channel.

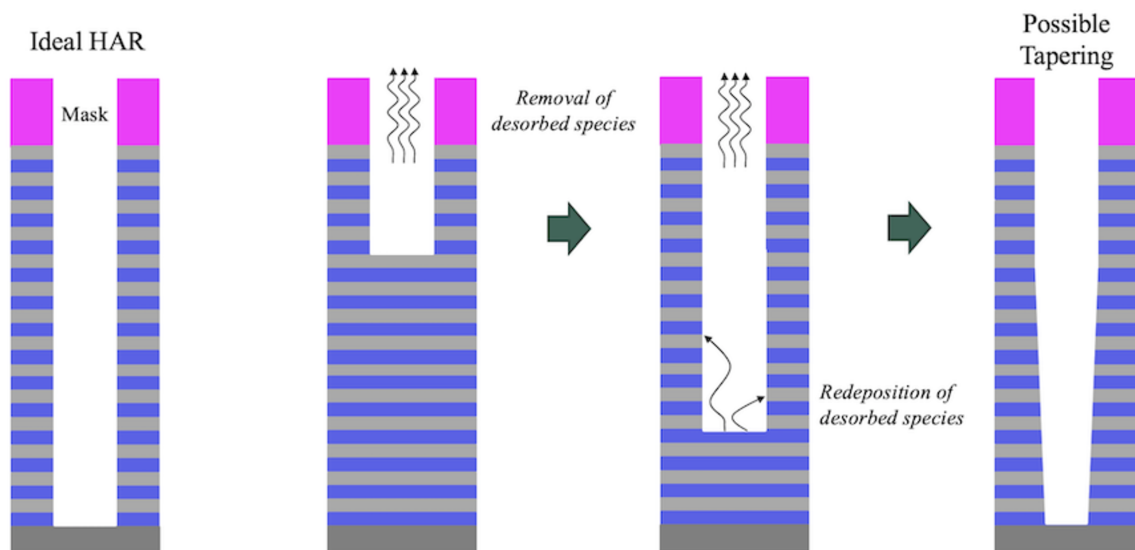

FIGURE 3.13: Schematic diagram of a possible mechanism of the formation of tapered HAR channels in 3D NAND.

3.4 Conclusions

In this study, MD simulations of etching of SiO_2, SiN, and ON bilayer model materials by energetic CF_3^+ ions were performed. In the etching of SiO_2 and SiN separate materials, good agreement between the experimental and the simulation etching yields was attained. In the ON bilayer etching, when the incident ion energy is low, the etch rates of oxide and nitride layers were observed separately since the thickness of the mixing layer is less than the initial thickness of the oxide layer. At high incident ion energies where the mixing layer is much thicker than the initial oxide layer, the mixture of oxide and nitride layers resulted in the single etch rate of the thicker underlying SiN layer. The results suggest

that, in the case of an ONON multilayer, the overall etch rate is expected to depend on the thicknesses of oxide and nitride layers as well as the ion incident energy. It is possible that, in the HAR deep hole etching of an ONON multilayer for 3D NAND device manufacturing, non-uniform layer thicknesses may result in spatially dependent etch rates across the horizontal cross-section of each hole, which could lead to the deflection of the etch front passing through the oxide-nitride interfaces and bend the etched hole channel. The desorbed species obtained from the simulations showed that the number of desorbed monoatomic species or small moieties with fewer chemical bonds increased with increasing ion energy. In HAR deep hole etching, desorbed species with dangling bonds are likely to be redeposited on the sidewalls of the hole channels.

Chapter 4

Molecular Dynamics Simulation of Oxide and Nitride Etching by CF_3^+ and Cl^+

4.1 Introduction

The 3D NAND flash memory devices has been the leading solution to any platforms that require high memory capacity (e.g. smartphones, laptops, etc.). In light of this, further scaling of 3D NAND is required. The simplest method of increasing the memory capacity of 3D NAND is by increasing the number of alternating films (e.g. SiO_2 and SiN) that form the memory cells. In the fabrication process of 3D NAND, pillars that goes through all deposited films must be created. As such, etching hole channels with high aspect ratio (HAR) and straight profiles is needed. However, creating a straight profile becomes more difficult as the aspect-ratio increases. As the aspect ratio increases, the flux of reactive species would have difficulty in reaching the bottom of the channel causing the RIE lag, and in some cases, an etch stop [24, 25]. Imperfect profile shapes such as tapering, bowing, necking, and incomplete etch has a higher tendency to occur

as the aspect-ratio increases. Due to this, HAR etching has been known as the main roadblock to further scaling of 3D NAND flash memory devices [5, 6, 17, 24].

Fluorocarbon plasma is commonly used in HAR etching and other etching processes in the semiconductor industry [27, 28, 32]. It is well known that in fluorocarbon plasma etching, the fluorine-to-carbon (F/C) ratio of the reactive species in the plasma would greatly affect whether deposition of the fluorocarbon (FC) film or the etching of the material would occur [32–34]. In light of this, this chapter focuses on exploring other species that can be incorporated in fluorocarbon plasma etching. In particular, this chapter studies the effect of adding Cl^+ ions to the commonly used fluorocarbon plasma in the etching SiO_2 and SiN through molecular dynamics (MD). To the best of the author's knowledge, MD simulation combining chlorine with fluorocarbon has not been done before. As such, interatomic potential that would model the interaction of chlorine with carbon and fluorine has been developed.

4.2 MD Simulation

Classical MD has been employed to simulate the etching of SiO_2 and SiN with chlorine-containing fluorocarbon plasma. With classical MD, Newton's equations of motions are numerically solved to determine the motion of the atoms. The behaviour of the atoms is defined by the forces acting on them. These forces can be described by interatomic potential models [39, 43, 46]. In this study, the interatomic potential model used is based on Stillinger-Weber (SW) potentials [48, 49]. The SW-potentials has been modified to include the two-body and three-body interactions for SiO_2 and SiN interacting with fluorocarbon and chlorine separately [45, 60, 62, 63, 74]. Interatomic potential models that include interaction of chlorine with fluorocarbon has not been develop. As such, the development of F–C–Cl interatomic potential model would be discussed in the next section.

MD simulations of Si, SiO_2, and SiN etching by Cl^+ injected at normal incidence with ion energies from 50eV to 3,000eV were done. The etching simulation with just Cl_+ were done to verify the interatomic potential model that was developed for Cl. The model Si film was created by placing Si atoms to form a diamond crystal structure in a rectangular box with a surface area of 18.84nm^2 (4.34nm x 4.34nm). The model SiO_2 and SiN films were created in a similar manner as the films used in Ref. 117 with surface areas of 17.5nm^2 (4.19nm x 4.19nm) and 15.7nm^2 (4.04nm x 3.88nm) respectively. A 0.5nm layer of atoms from the bottom of the films are fixed to prevent lateral displacement of the simulation box. The fixed layer also serves as the bonding sites for adding new film layers called 'anchor'. Since additional film layers can be added, the height of the film is theoretically infinite. Periodic boundary conditions are applied in the horizontal directions such that an actual surface can be mimicked. All films are thermalized at 300K before ion injection, and whenever an anchor is added. To understand the etching mechanism of SiO_2 and SiN with chlorine-containing fluorocarbon plasma, MD simulations by alternating injection of CF_3^+ and Cl^+ were done. MD simulations by alternating injection of CF_3^+ and Ar^+ were also done to supplement the results.

The SiO_2 and SiN films were etched by alternating injection of CF_3^+ and Cl^+ ions at normal and 60° incidence with ion energies from 500eV to 2,000eV as shown in Fig. 4.1. The 60° incident angle had been chosen based on previous simulations wherein the etching of SiO_2 by CF_3^+ with incident angle 0° – 85° showed the highest etch yield at 60° [47]. Though CF_3^+ and Cl^+ are referred to as ions, they are actually treated as charge-neutral species since electrical charges of ions were not considered in the interatomic potential models. Electrical charges were not considered under the assumption that charged species in the plasma are neutralized by the Auger effect upon interaction with the surface [73, 74]. After injecting the ion, the system is allowed to evolve for 300fs under microcanonical NVE ensemble wherein the total-energy of the system is conserved. During this period, the kinetic energy of from the ion is transferred to the film which subsequently causes the collision cascade. As such, the volume-averaged temperature of the system increases.

Films used in reality are much larger, and can readily dissipate the energy transferred from the ion. However, the simulation box used in the simulation are much smaller. As such, artificial cooling of the system was done to prevent unrealistic heating of the films. Artificial cooling to 300K was done by gradually decreasing the velocities of all atoms for 1600fs using the Langevin thermostat [57] and for 100s using the Berendsen thermostat [58, 59]. Atoms not bonded to the bulk of the film (i.e. positioned above the film) are considered as etched products or desorbed species. These species are not cooled, are allowed to move without changing its velocities until the end of the cycle. Each injection cycle lasts for 2,000fs with a variable time step of of 0.2 – 0.5fs. The time step changes in accordance to the velocity of the fastest atom, and is small enough such that the total energy of the system can be conserved. At each time step, the positions and velocities of the atoms are calculated using the velocity-Verlet algorithm [131, 132]. At the end of injection cycle, the desorbed species are removed. The resulting film would then be used for the next cycle. The injection cycle is repeated continuously until relevant macroscopic properties such as the etch yield can be obtained with sufficient statistical accuracy.

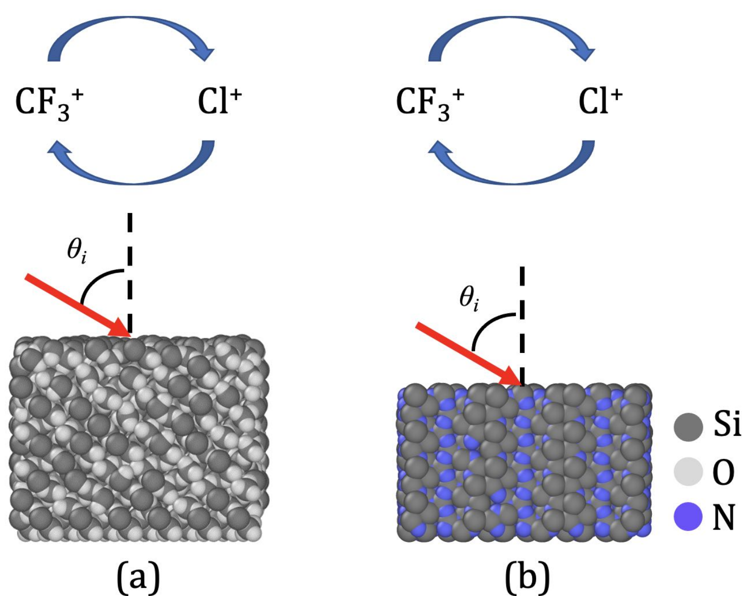

FIGURE 4.1: Sideview images of the (a) SiO_2 and (b) SiN model films etched by alternating injection of $CF_3{}^+$ and Cl^+ injected at incident angle θ_i of 0° (normal) and 60°.

4.3 Interatomic Potential Model for Fluorocarbon and Chlorine Interaction

In this section, an interatomic potential model for the interaction of chlorine with carbon and fluorine was developed for the etching of SiO_2 and SiN by CF_3^+ and Cl^+. The interatomic potential models for all other interactions are the same models used in previous studies shown in Refs. 45, 53, 60–72.

The interatomic potential model for Cl–C–F interaction is based on SW-type potential where the total potential energy Φ is given as the summation of the two-body V_2 and three-body V_3 interactions as shown in Eq. 4.1 [48, 49]. In this SW-type potential model, all atoms are considered as charge-neutral species.

$$\Phi = \sum_{i<j} V_2(i,j) + \sum_{i<j<k} V_3(i,j,k) \tag{4.1}$$

The calculations for the interatomic potential model is based on previous studies [45, 74, 110, 115] wherein Eq. 4.1 is parameterized. The two-body V_2 interaction between the ith and jth atoms would be dependent on their interatomic distance r_{ij}, and is given by the repulsive V_R and attractive or bonding V_B interaction between the two atoms.

$$\begin{aligned} V_R &= ar^{-p} \exp\left(\frac{c}{r - r_c}\right) \\ V_B &= -br^{-q} \exp\left(\frac{d}{r - r_c}\right) \end{aligned} \tag{4.2}$$

Assuming that V_R is linearly dependent on the square of V_B ($p = 2q$ and $c = 2d$), the two-body V_2 interaction is given by

$$V_2(i,j) = ar^{-2q} \exp\left(\frac{2d}{r_{ij} - r_c}\right) - br^{-q} \exp\left(\frac{d}{r_{ij} - r_c}\right), \text{ if } r_{ij} < r_c \tag{4.3}$$

Table 4.1: Calculated parameter values for the two-body V_2 interaction of C–Cl.

Parameters	Values	Units
a	548.92	$(eV)^{2q}/Å$
b	86.40	$(eV)^{q}/Å$
q	1.39	
d	3.93	Å
r_c	3.99	Å

Table 4.2: Calculated parameter values for the two-body repulsive V_R interaction of C–Cl.

Parameters	Values
a	27951.76
p	0.75
c	10.17
r_c	2.36

where a, b, d, q, and r_c are parameters with r_c being the interatomic cutoff distance. The two-body V_2 interaction would be zero if $r_{ij} \geq r_c$.

The two-body V_2 potential energy curve for the Cl and C atoms from a stable CH_3Cl molecule was obtained from *ab initio* quantum mechanical calculations based on density functional theory (DFT). The calculations were done using a B3LYP/6-311G basis set using the software *Gaussian* [52]. In the calculation, the interatomic distance between C and Cl were varied from 0.6 to 4.8Å with a 0.05Å step while maintaining the C-H bond lengths. The C–Cl potential energy per 0.05Å step was obtained by subtracting the total energies of the C, Cl, and H atoms from the total energy of a CH_3Cl molecule. The final C–Cl potential energy as function of interatomic distance was obtained by adjusting the curve to the published minimum bonding energy -3.39eV at 1.77Å interatomic distance [134]. The potential energy obtained from DFT is fitted with Eq. 4.1 using Levenberg-Marquardt nonlinear fitting as shown in Fig. 4.2. The parameters obtained from the fitting are summarized in Table 4.1.

For purely repulsive interaction, V_R in Eq. 4.2 is fitted to the same data points obtained from DFT calculations as shown in Fig. 4.3. The parameters obtained from the fitting are summarized in Table 4.2.

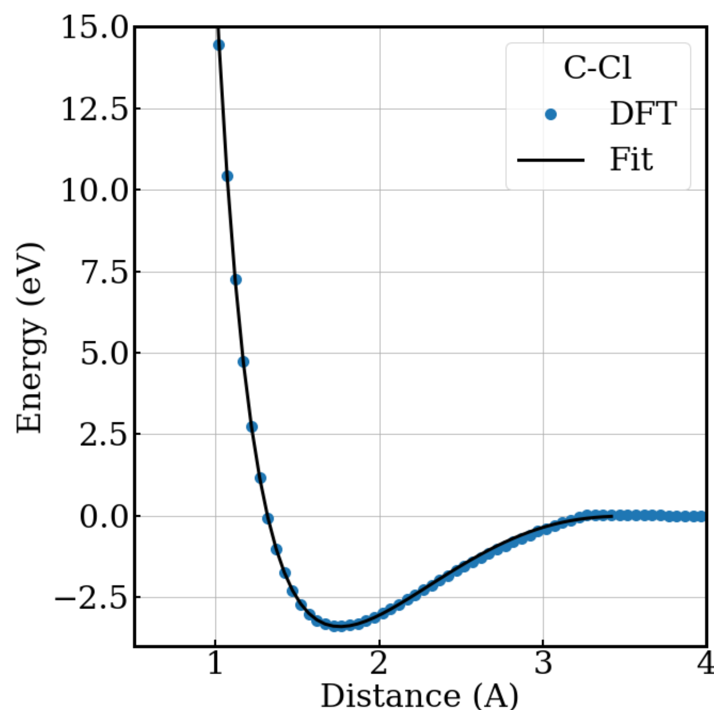

FIGURE 4.2: C–Cl two-body V_2 potential energy as a function of the interatomic distance. The data points are obtained from DFT calculations, and the curve is obtained from fitting V_2 interaction described by Eq. 4.1.

In a similar manner, the two-body V_2 potential energy curve for the interaction of Cl and F was also obtained from *ab initio* DFT calculations using a FCl molecule. The F–Cl potential energy was obtained by subtracting the total energies of the F and Cl atoms from the total energy of a FCl molecule. The final F–Cl potential energy as function of interatomic distance was obtained by adjusting the curve to the published minimum bonding energy -2.58eV at 1.63Å interatomic distance [134]. The potential energy obtained from DFT is also fitted with Eq. 4.1 using Levenberg-Marquardt nonlinear fitting as shown in Fig. 4.4. The parameters obtained from the fitting are also summarized in Table 4.3. The repulsive V_R interaction in Eq. 4.2 is also fitted to the same data points obtained from DFT calculations as shown in Fig. 4.5. The parameters obtained from the fitting are summarized in Table 4.4.

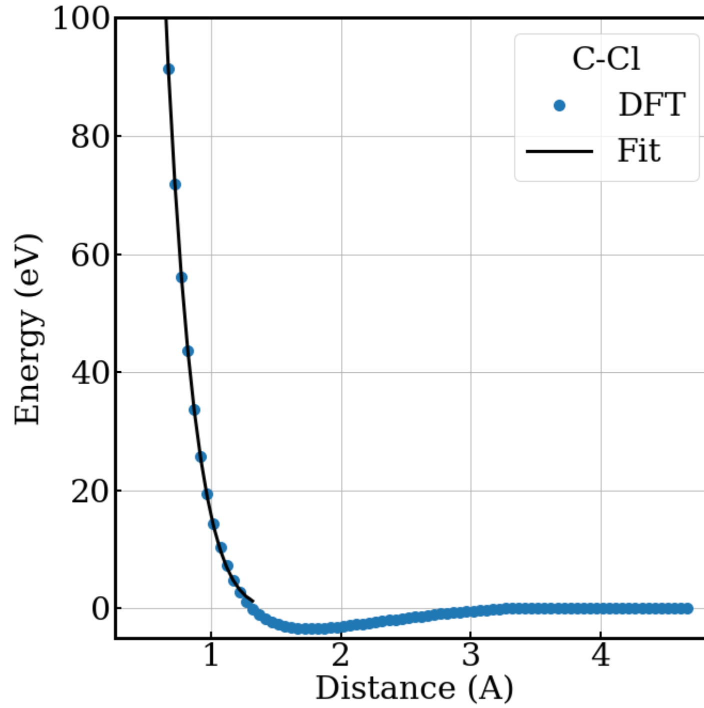

FIGURE 4.3: C–Cl two-body V_2 potential energy as a function of the interatomic distance. The data points are obtained from DFT calculations, and the curve is obtained from fitting V_R interaction described by Eq. 4.2.

TABLE 4.3: Calculated parameter values for the two-body V_2 interaction of F–Cl.

Parameters	Values	Units
a	661.35	$(eV)^{2q}/Å$
b	82.67	$(eV)^{q}/Å$
q	1.17	
d	3.55	Å
r_c	3.22	Å

The three-body V_3 interaction given by

$$V_3(i,j,k) = h_{jik}(r_{ij}, r_{ik}, \theta_{jik}) + h_{ijk}(r_{ji}, r_{jk}, \theta_{ijk}) + h_{ikj}(r_{ki}, r_{kj}, \theta_{ikj}). \tag{4.4}$$

describes the angular dependencies of the ith, j^{th}, and k^{th} atoms. The h function expressed below is dependent on the angle between three atoms θ, and the distances r of the two atoms from the vertex atom denoted by the center subscript.

$$h_{ijk}(r_{ji}, r_{jk}, \theta_{ijk}) = k_{ijk}|\cos\theta_{ijk} - \Theta_{ijk}|^{\gamma_{ijk}} f_{ij}(r_{ij}) f_{jk}(r_{jk}). \tag{4.5}$$

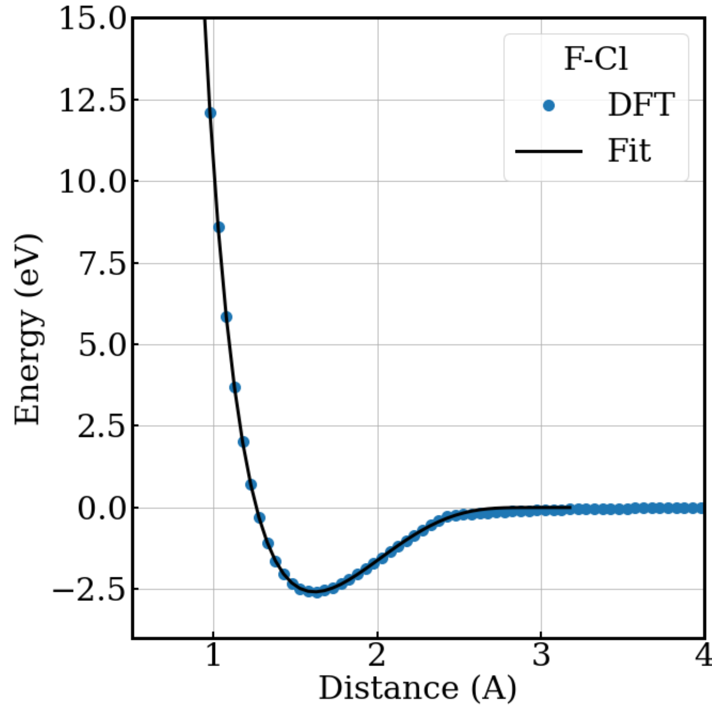

FIGURE 4.4: F–Cl two-body V_2 potential energy as a function of the interatomic distance. The data points are obtained from DFT calculations, and the curve is obtained from fitting V_2 interaction described by Eq. 4.1.

TABLE 4.4: Calculated parameter values for the two-body repulsive V_R interaction of F–Cl based on FCl molecule.

Parameters	Values
a	3013.26
p	1.49
c	5.84
r_c	2.02

where k, Θ, and γ are parameters. The f function prevents the overestimation of the angular dependency, and is dependent on V_2 given by

$$f_{ij}(r) = \begin{cases} 1, & r \leq r_{min}, \\ \frac{V_2(r)}{V_{2min}}, & r_{min} < r < r_c, \\ 0, & r > r_c, \end{cases} \tag{4.6}$$

where r_{min} is the distance between the ith and jth at the minimum two-body interaction

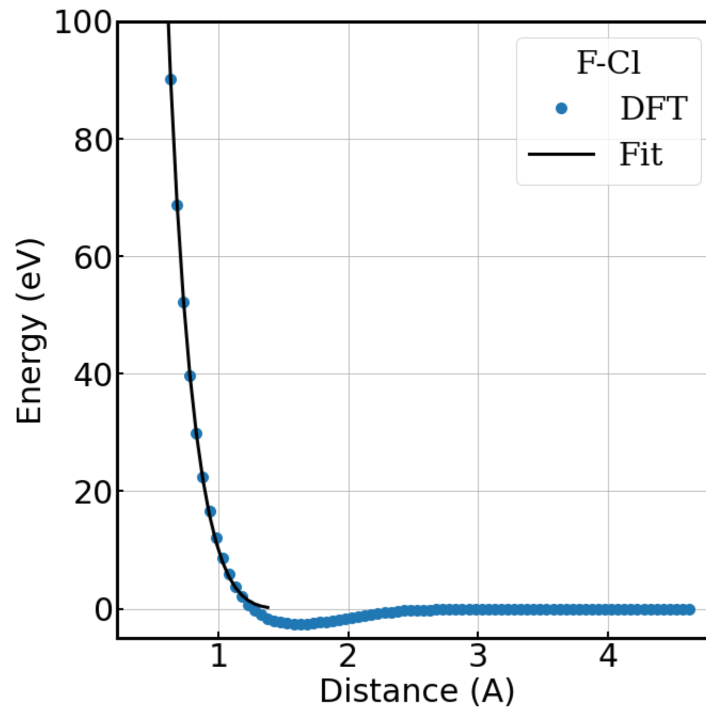

FIGURE 4.5: F–Cl two-body V_2 potential energy as a function of the interatomic. The data points are obtained from DFT calculations, and the curve is obtained from fitting V_R interaction described by Eq. 4.2.

energy V_{2min}. Since the k, Θ, and γ are parameters dependent on the configuration describe by its subscript, the parameters for all possible three-body V_3 configurations of the system with Si, O, N, C, F, and Cl atoms must be calculated. The calculation for the parameters of the single bonded F–C–Cl three-body V_3 interaction is shown as example in this section.

The three-body V_3 potential energy of F–C–Cl as a function of the angle θ was also obtained from *ab initio* DFT calculations using a chlorofluoromethane (CH_2ClF) molecule. In this calculation, the bond lengths of between atoms are maintained. Only the angle θ_{FCCl} between the F, C, and Cl atoms with C as the center atom was varied by 1° increment without changing the azimuthal angle. The potential energy obtained from DFT is fitted against Eq. 4.5 as shown in Fig. 4.6. The potential energy data as a function of the angle θ fitted against Eq. 4.5 for other configurations with Cl are shown in Appendix C. The parameters k, Θ, and γ for various configuration of Cl with Si, O, N, C, and F

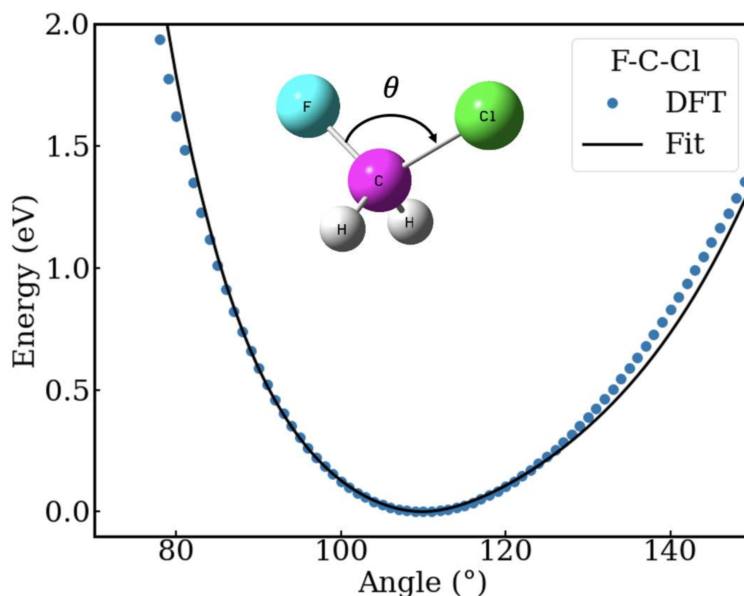

FIGURE 4.6: F–C–Cl three-body V_3 potential energy as a function of the angle θ. The data points are obtained from DFT calculations, and the curve is obtained from fitting V_3 interaction described by Eq. 4.5. The DFT calculation was done on a chlorofluoromethane (CH_2ClF) molecule wherein the bond lengths of all atoms are maintained. Only the angle θ was varied without changing the azimuthal angle.

are summarized in Table 4.5.

4.4 Results and Discussion

4.4.1 Simulation and Experimental Etch Yield Comparison

The interatomic potential model developed in this study were tested by performing MD simulation of the etching of Si, SiO_2, and SiN by Cl^+ ions. The etch yield as a function of ion energies from the MD simulations were then compared to existing ion beam experimental studies for Si [135, 136], and etch yields for SiO_2 as shown in Fig. 4.7. The experimental etch yield for SiO_2 was obtained from beam experiments done with the mass-selected ion beam system discussed in Ch. 1. Ion beam experimental studies of SiN etched by Cl^+ ions has not been completed. In this figure, the simulation etch yield is calculated as the removed Si per injected ion during steady-state etching. The etch

TABLE 4.5: Calculated parameter values for the three-body V_3 interactions for various configurations of Cl with Si, O, N, C, and F.

Configuration	k	Θ	γ
F–C–Cl	6.339864	-0.344385	2.228620
C–C–Cl	6.362699	-0.365817	2.317829
Cl–C–Cl	6.795467	-0.388800	2.270487
H–C–Cl	3.768094	-0.288685	2.223051
N–C–Cl	5.871474	-0.410142	2.184573
Si–C–Cl	4.004965	-0.376433	2.153366
O–C–Cl	5.326747	-0.307112	2.076946
C=C–Cl	6.267638	-0.531098	2.086608
O=C–Cl	5.770617	-0.543057	1.961318
N=C–Cl	3.784756	-0.529934	2.083379
C≡C–Cl	2.157150	-0.944879	1.810899
N≡C–Cl	3.611220	-1.000000	1.309323
C–Si–Cl	3.608483	-0.319625	2.307230
F–Si–Cl	3.373096	-0.314520	2.206953
N–Si–Cl	2.428939	-0.407355	1.912306
C–O–Cl	3.981111	-0.356296	1.989148
F–O–Cl	4.782706	-0.308851	2.149168
N–O–Cl	4.275831	-0.412694	2.077401
C–N–Cl	4.303012	-0.346871	2.032523
F–N–Cl	4.070931	-0.283824	1.994282
H–N–Cl	2.515344	-0.244634	1.992099
N–N–Cl	5.087651	-0.381209	2.182551
O–N–Cl	4.779717	-0.337203	2.075855
Si–N–Cl	4.347006	-0.488270	2.323039
O=N–Cl	6.829497	-0.435532	2.200072
C=N–Cl	1.864396	-1.014258	1.170672

yields of Si and SiO_2 showed relatively good agreement with experimental yields. The simulation etch yields of SiO_2 and SiN by CF_3^+ ions as a function of ion energy were published in Ref. 117 and discussed in Ch. 3. The relatively good agreement between the simulation and experiment suggests that the MD simulation could provide good insight in the etching of SiO_2 and SiN by CF_3^+ ions with Cl^+ ions.

4.4.2 Etching of SiO_2 and SiN by CF_3^+ ions with Cl^+ ions

In this section, the effects of adding Cl^+ to the etching of SiO_2 and SiN by CF_3^+ ions would be discussed.

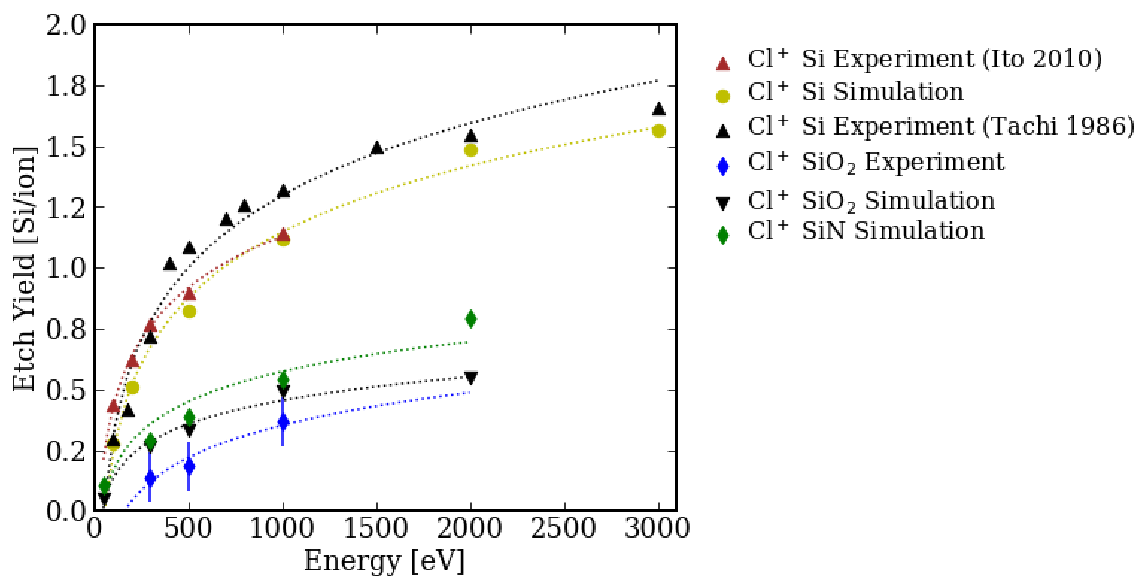

FIGURE 4.7: The etch yields of Si, SiO_2, and SiN by Cl^+ as a function of ion energy obtained from MD simulation. For comparison, the etch yields of Si [135, 136] and SiO_2 by Cl^+ ions obtained from ion beam experiments are also shown. Ion beam experiment for SiN etched by Cl^+ ions has not been completed.

Figure 4.8 shows the instantaneous etching yields of (a) SiO_2 and (c) SiN by 1,000eV $CF_3{}^+$ ions and Cl^+ for all atomic species of the systems and the corresponding changes in depth for (b) SiO_2 and (d) SiN as functions of the ion dose obtained from MD simulations during steady-state etching. Since the $CF_3{}^+$ ions and Cl^+ ions were injected alternatingly, the ion dose considered is only for the $CF_3{}^+$ ions. As such, steady-state etching is defined when the etch yield of Si, O, and N atoms are positive, and when the average removed C, F, and Cl atoms are 1, 3, and 1 respectively. Steady-state etching was found to begin at $1.0\text{x}10^{16}$ $CF_3{}^+$ ions/cm^2. By doing this, the etching simulations can be easily compared to the etching simulations with only $CF_3{}^+$ ions. Since etch time as defined in experiments is not a parameter in the simulations, the etch rate is defined as the change in depth as a function of the ion dose as shown in Fig. 4.8(b) and (d). Since the etch yield is directly correlated to the etch rate, subsequent discussion would be focused on the etch rate.

Figure 4.9 shows the etch rate of SiO_2 etched by 1,000eV $CF_3{}^+$ ions with Cl^+ ions injected at 0° and 60° incident angles. This was compared with etching simulation of SiO_2 by $CF_3{}^+$ ions only. At 0° incidence, an increase in the etch rate at the beginning

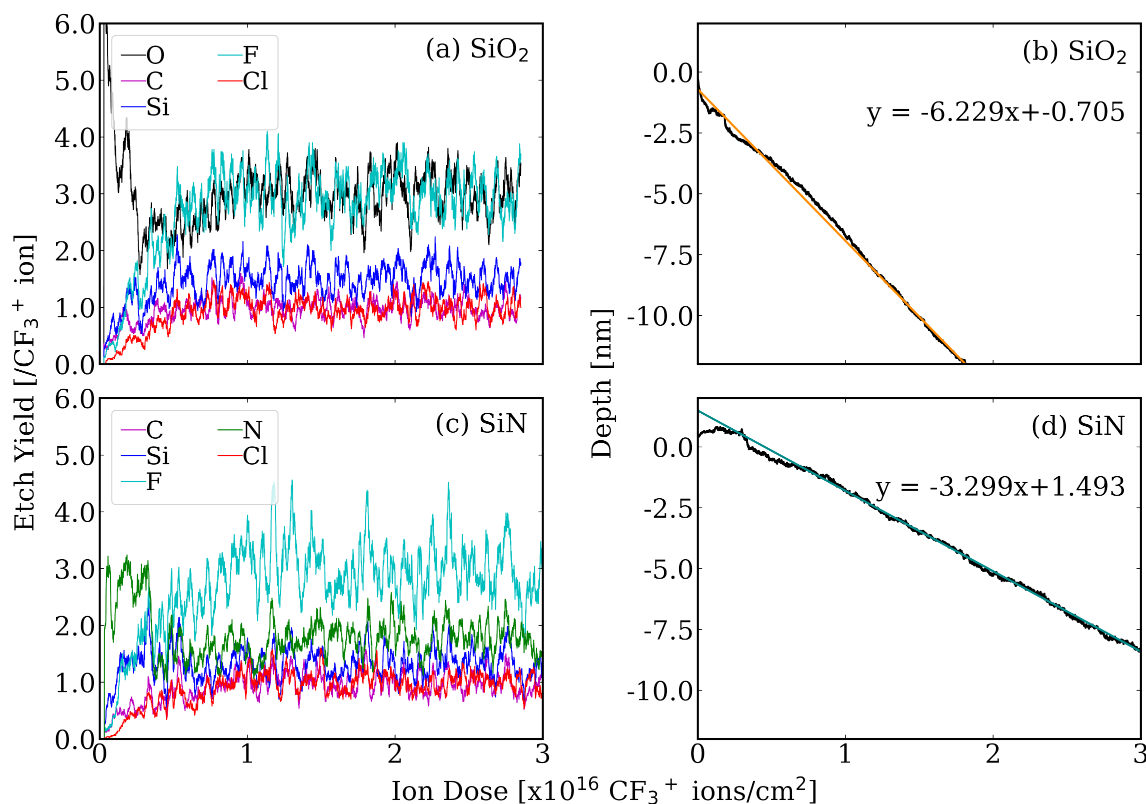

FIGURE 4.8: Instantaneous etching yields (a) SiO_2 and (c) SiN by 1,000eV CF_3^+ ions with Cl^+ ions for all atomic species of the systems and the corresponding changes in depth for (b) SiO_2 and (d) SiN as functions of the ion dose obtained from MD simulations. Here, the x-axis denotes only the CF_3^+ ion dose. The angle of ion incidence is normal to the film surface.

of etching could be observed. However, it can be readily seen that adding Cl^+ ions to CF_3^+ ions has minimal change to the etch rate of SiO_2 once steady-state etching has been attained. The expected increase in etch rate was only observed when the incident angle was changed to 60°.

The calculation of the etch rate was done for both SiO_2 and SiN at all energies. The etch rates are then plotted as a function of ion energy as shown in Fig. 4.10. The etch rates of SiO_2 and SiN by CF_3^+ ions with Cl^+ ions are plotted with black and red square markers for 0° and 60° incident angles. For comparison, the etch rates SiO_2 and SiN etched by CF_3^+ ions only are also plotted as blue and green circle markers respectively. It can be seen in this figure that the etch rate of SiO_2 is greater than the etch rate of SiN. This was expected due to the difference in material density even though the etch yield of

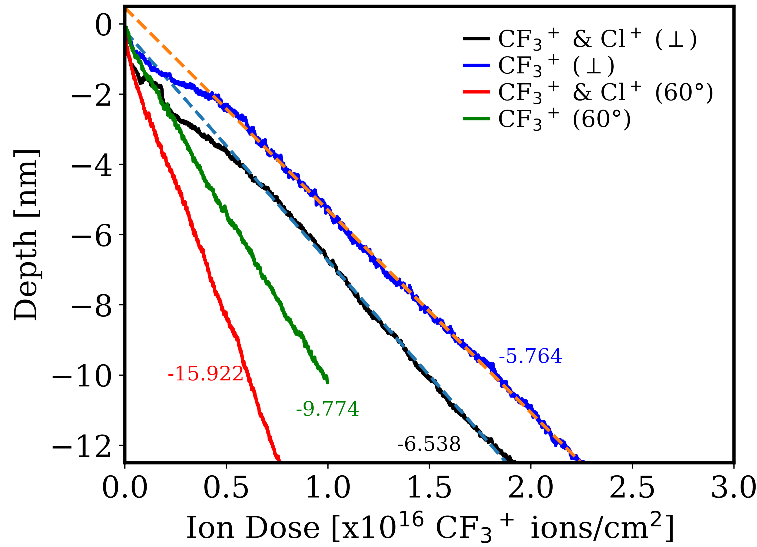

FIGURE 4.9: Change in depth as a function of ion dose of SiO_2 etched by 1,000eV CF_3^+ ions with Cl^+ ions injected at 0° and 60° incident angles. This was compared with etching simulation of SiO_2 by CF_3^+ ions only. Here, the x-axis denotes only the CF_3^+ ion dose. The y-axis denotes the thickness of the etched material with zero as the initial material height. The orange and cyan dashed lines are sample fitting lines for the slope calculation during steady-state etching. The values denote the calculated slopes representing the etch rate.

SiO_2 and SiN by CF_3^+ ions with Cl^+ ions only have small differences. However, it was unexpected that the etch rate for SiO_2 would not change at all ion energies. The minimal change in the etch rate was also observed for SiN except at 500eV CF_3^+ ions with Cl^+ ions. For SiN at 500eV, adding Cl^+ ions to the CF_3^+ ions actually inhibited the etching as evidenced by the decrease in etch rate. We expected that adding Cl^+ ions to CF_3^+ ions would result to an increase in etch rate since the etch rate with just Cl^+ ions would be added to the etch rate with just CF_3^+ ions. However, such effects for both SiO_2 and SiN were only observed when the ions are injected at 60° incident angle. At 60°, adding Cl^+ ions to CF_3^+ ions resulted to ≈1.6x increase in the etch rate.

The depth profiles as a function of atomic densities of each species for SiN etched at 500eV ion energy are plotted in Fig. 4.11. The proceeding discussion would focus on the results for SiN at 500eV since much of the effects of adding Cl^+ ions could be observed at this case. Looking first at Fig. 4.11(c) and (d), the difference of the material surface could already be seen. Since the ion is injected at an angle for Fig. 4.11(d), the penetration

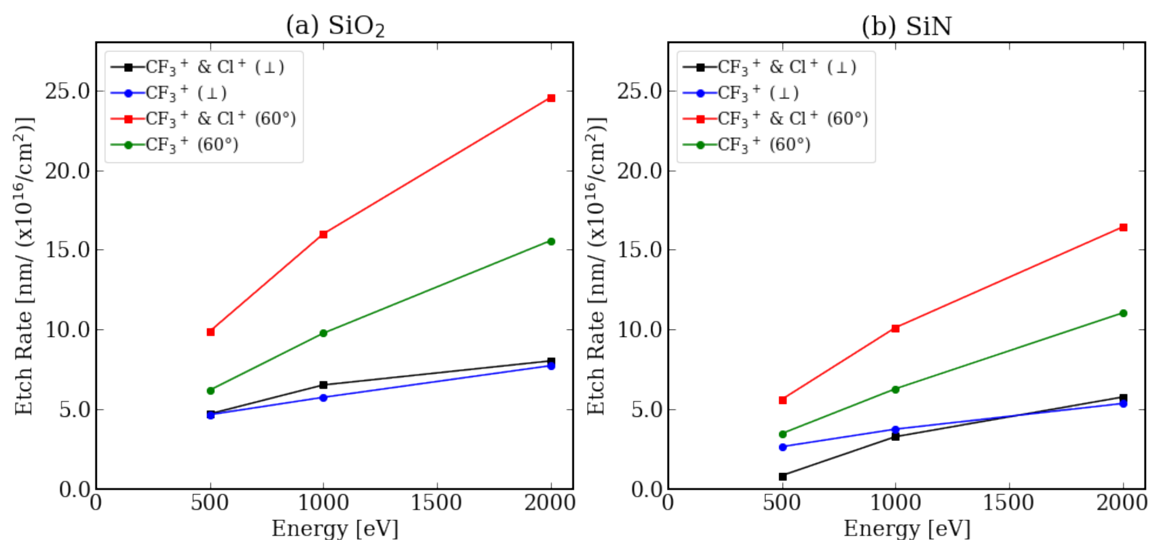

FIGURE 4.10: Etch rate as a function of ion energy for (a) SiO_2 and (b) SiN etched by CF_3^+ ions with Cl^+ ions denoted by square markers, and by CF_3^+ ions only denoted by circle markers. The ions are injected at 0° and 60° incident angles. The lines are just guides to the eyes.

depth of the ions is shallower compared to Fig. 4.11(c). As such, the mixing layer when the ions are injected at 60° is thinner and less dense compared to 0°. Here, the mixing layer is defined as the layer that contains Si, N, C and F atoms. At 60°, the etch rate is higher even with a thinner modified layer. It is likely that at 60°, physical sputtering is more dominant.

Comparing Fig. 4.11(c) to Fig. 4.11(a), the effect of adding Cl^+ ions to CF_3^+ ions could clearly be seen by the much denser mixing layer in Fig. 4.11(a). The lower etch rate observed at Fig. 4.10 for SiN etched at 500eV CF_3^+ ions with Cl^+ ions could then be attributed to a much higher atomic densities for C and F shown in Fig. 4.11(a). It is well known that in fluorocarbon etching, a surface layer containing FC species is needed to facilitate the etching [63]. However, when the deposition of the FC species overtakes the etching of the material, etch stop could occur due to the formation of a thick FC film that would passivate the surface. In line with this, it is possible that due to the relatively low energy of 500eV, the Cl_+ ions retained by the material blocks the CF_3^+ from etching the SiN. Since the CF_3^+ ions are not being used in etching, deposition of the FC film would be more favourable. Figure 4.11(b) showed the SiN material with the least atomic

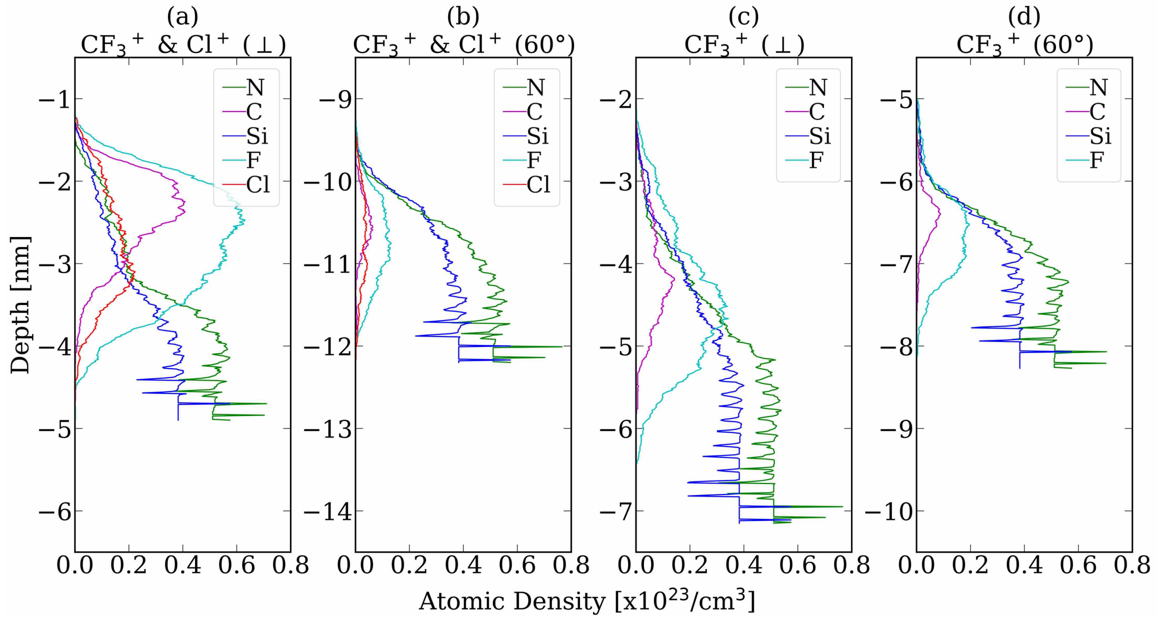

FIGURE 4.11: The depth profiles of the atomic densities for SiN etched by 500eV CF_3^+ & Cl^+ injected at (a) 0° and (b) 60°, compared to SiN etched by 500eV CF_3^+ ions injected at (c) 0° and (d) 60°. The depth profiles were taken at the same ion dose of 1.8x10^{16} CF_3^+ ions/cm^2. The origin of the vertical axis is the position of the material's top surface prior to etching. The vertical axes have different ranges but same increment.

densities for C and F. Due to a thinner mixing layer for this case, the ions can readily sputter the SiN material.

The depth profiles of atomic densities for both SiO_2 and SiN at other energies are shown in Appendix C. Based on the depth profiles of atomic densities, it can be inferred that the Cl^+ injected at 0° would spend most of its kinetic energy on a thick mixing layer. With a thick mixing layer, the Cl $^+$ ions would just etch the carbon and fluorine on top. As such, the etch rate of SiO_2 at all ion energies, and the etch rate of SiN at >500eV ion energies had minimal changes with the addition of Cl^+ to CF_3^+ ions. It can be said that the net effect of the etching by adding Cl^+ ions, and the deposition of the FC species to form the mixing layer is essentially zero.

To determine the etching mechanism of Cl^+ ions when added to CF_3^+ ions, additional simulations wherein Cl^+ ions were replaced with Ar^+ ions were performed. Argon was chosen due to two reasons: (1) similar mass with chlorine; and (2) inert. With Ar having a similar mass with the system, a similar physical interaction with the system could be

expected. Also, Ar would have a different chemical interaction compared to Cl since Ar is inert. This would help highlight the chemical effects of adding Cl^+ to CF_3^+ ions. Results (Appendix C) showed that for both SiO_2 and SiN etched by CF_3^+ ions with Ar^+ ions at 0°, minimal change in the etch rates for all ion energies compared to the etching without Ar^+ ions was observed. Also at 60°, addition of Ar^+ ions to CF_3^+ ions exhibited similar etch rates with the addition of Cl^+ ions to CF_3^+ ions. Since both Ar and Cl showed the same etch rates except for SiN etched by 500eV ions injected at 0°, it can be inferred that the mechanism upon which Cl removes the fluorocarbon is through physical sputtering. To further verify this, the etched products or desorbed species for the etching of SiO_2 and SiN by CF_3^+ ions with Cl^+ ions were also studied.

4.4.3 Desorbed Species from the Etching of SiO_2 and SiN by CF_3^+ and Cl^+

The desorbed species from the MD simulation of the etching of SiO_2 by CF_3^+ ions with and without addition of Cl^+ ions were plotted in Fig. 4.12. There were various desorbed species but only relevant ones were plotted. It can be observed in Fig. 4.12 that by injecting the ions at 60° incident angle, the yield of monoatomic species (e.g. Fig. 4.12(a) Si and Fig. 4.12(b) O) removed through physical sputtering increases. By adding Cl^+ ions to CF_3^+ ions at 60°, this yield would be further increased due to the higher ion flux. As a consequence, the yield of heavier molecules (e.g. Fig. 4.12(h) SiF_3 and Fig. 4.12(i) SiF_4) removed through chemical sputtering decreases.

It can also be observed that the yield of heavier SiF_x species (Fig. 4.12(h)–(j)) is highest for CF_3^+ ions injected at 0°. This yield would also decrease when Cl^+ ions injected at 0°are added. Additionally, the yield of monoatomic C and F increased when Cl^+ ions were added as shown in Fig. 4.12(f) and (m). The trends observed in the desorbed species support the inference in the previous section which suggests that Cl^+ ions primarily remove the fluorocarbon through physical sputtering. The desorbed species

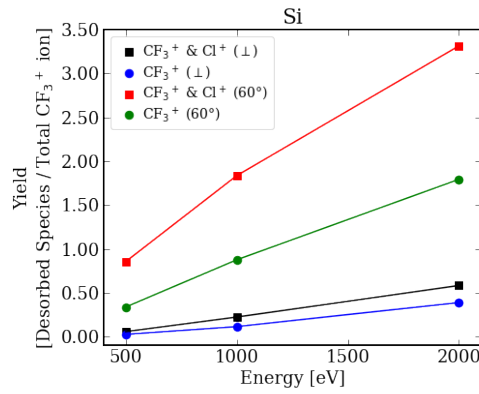

(a)

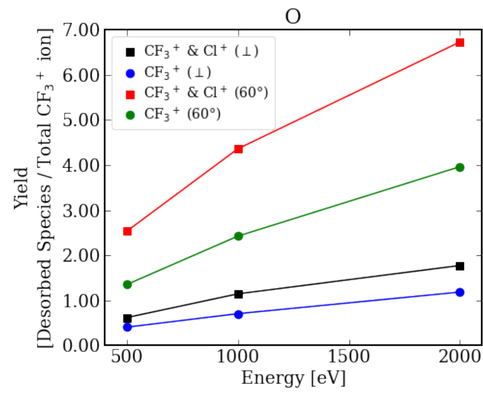

(b)

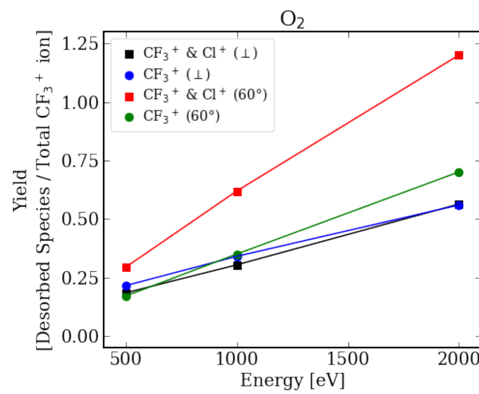

(c)

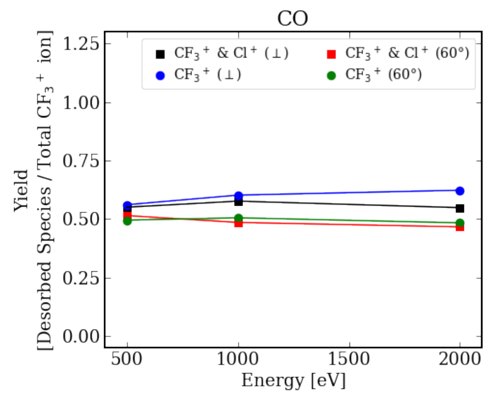

(d)

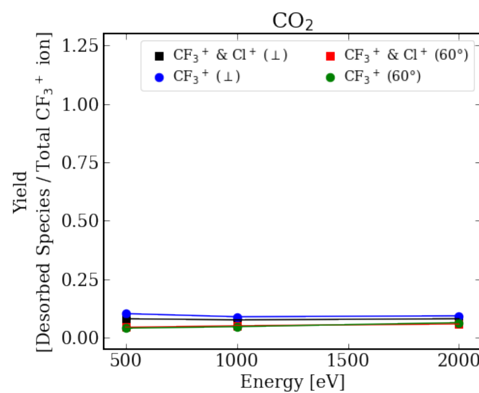

(e)

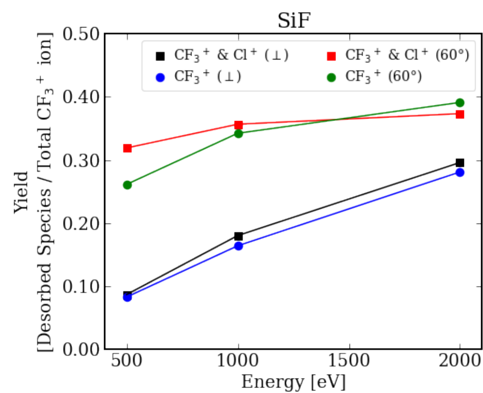

(f)

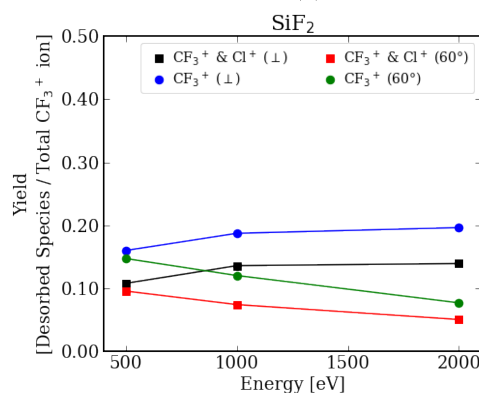

(g)

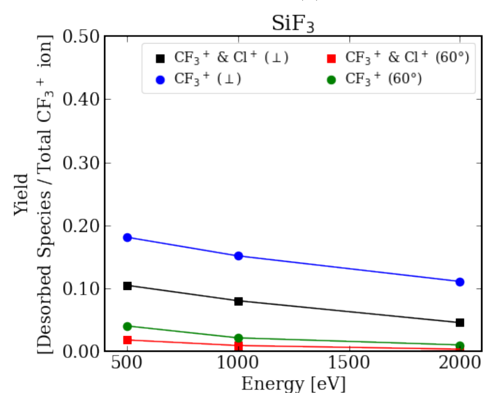

(h)

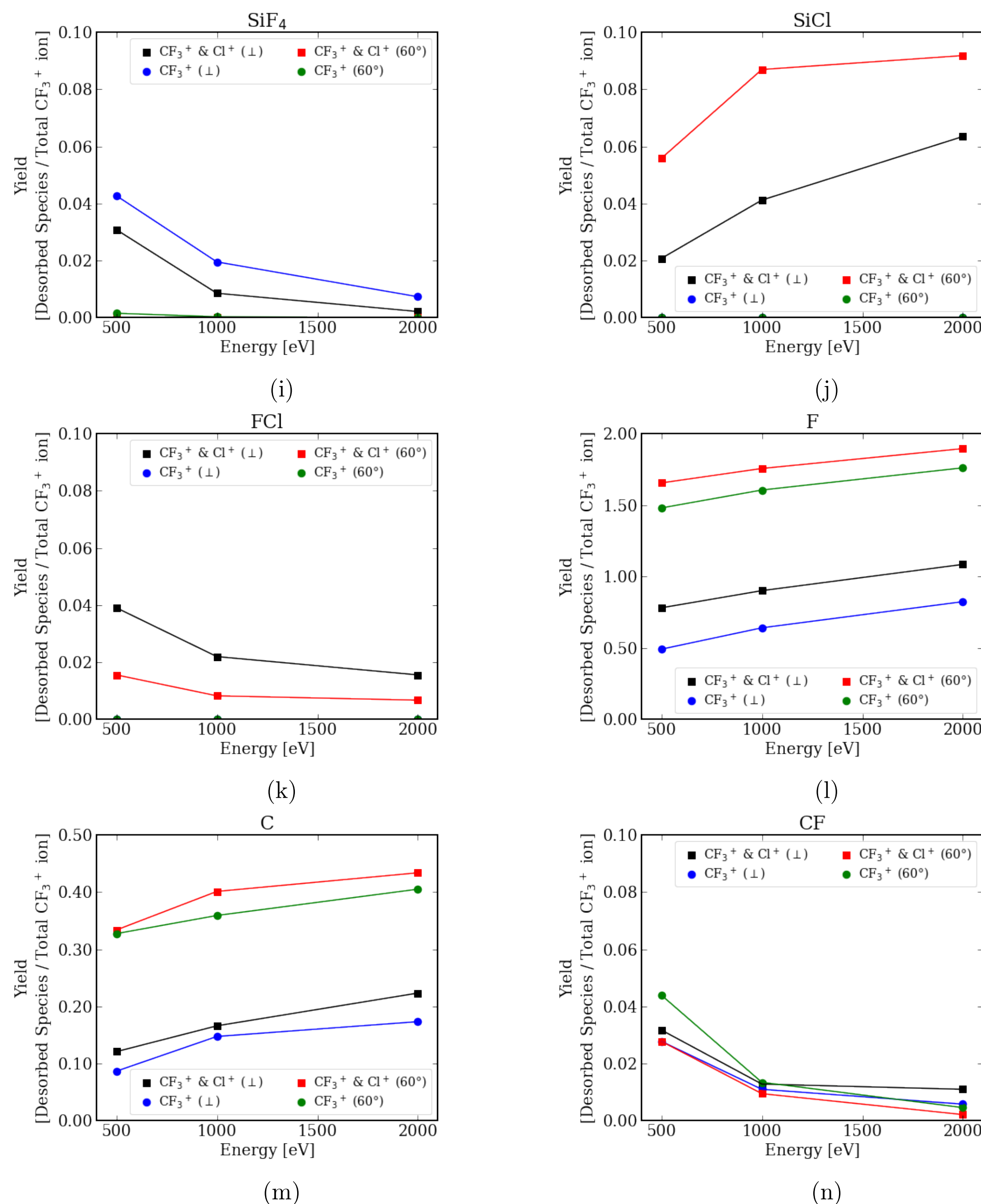

FIGURE 4.12: The yield of the desorbed species as a function of ion energy for SiO_2 etched by CF_3^+ ions with and without addition of Cl^+ ions. The yield is calculated as the number of specified desorbed species over the total number of injected CF_3^+ ions.

from the MD simulation of the etching of SiN by CF_3^+ ions with and without addition of Cl^+ ions were plotted in Appendix C. The trends observed in the desorbed species for SiN are similar to that of SiO_2. The main difference was only observed for SiN etched by

500eV CF_3^+ ions with Cl^+ ions injected at 0° wherein a much higher yield of CF molecule was observed. As such, further discussion would not be necessary.

Implications of the results of the MD simulations of the etching of oxide and nitride by CF_3^+ ions with and without addition of Cl^+ ions is on the effects in the etching of a tapered structure. In a tapered HAR channel, the ion flux reaching the bottom of the channel would come at normal incidence. In contrast, the ions would hit the channel sidewalls at an angle. Based on the results of the MD simulation, the etch rate at the bottom of the trench would be the same but the etch rate of the tapered sidewall could be faster. This could lead to smoothing of the tapered sidewall, and form a straight channel profile as schematically illustrated in Fig. 4.13.

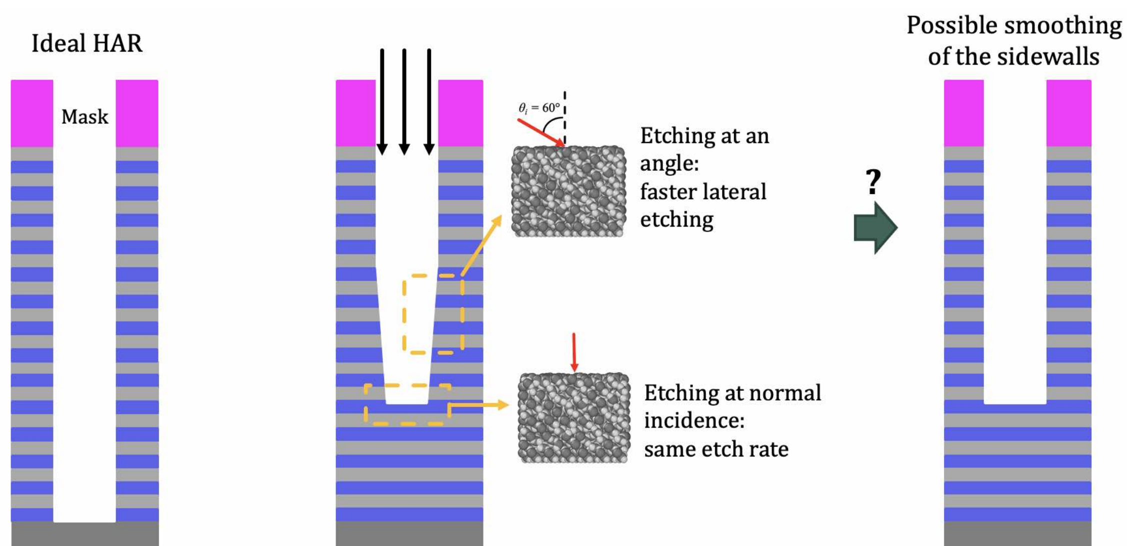

FIGURE 4.13: Schematic diagram of a possible mechanism of the smoothing of tapered HAR channels in 3D NAND.

4.5 Conclusion

In this study, MD simulations of etching of SiO_2, and SiN by energetic CF_3^+ ions with and without Cl^+ ions injected at 0° and 60° were performed. To perform MD simulation combining chlorine with fluorocarbon, interatomic potential that would model the

interaction of chlorine with carbon and fluorine has been developed. To validate the interatomic potential model developed, MD simulation of the etching of Si, SiO_2, and SiN by Cl^+ were performed. Good agreement between the etch yield results from the MD simulations and ion beam experiments were obtained.

In the MD simulation of the etching of SiO_2 and SiN by CF_3^+ ions and Cl^+ ions, it was determined that adding Cl^+ ions at 0° had minimal effect on the etch rate of both SiO_2 and SiN. This was true at all ion energies for SiO_2 but not for SiN. Adding 500eV Cl^+ ions at 0° to the etching of SiN resulted to the decrease in etch rate. It was determined that the etch rate decreased due to the deposited FC film that passivated the SiN material. The minimal and even negative effect of adding Cl^+ ions at 0° to CF_3^+ ions was attributed to the possibility that much of the energy of the Cl^+ ions is spent on etching the carbon and fluorine atoms from the thick mixing layer formed during etching at 0°. In contrast, an increase in etch rate was observed when the added Cl^+ ions were injected at 60° since the resulting mixing layer would be thinner. By replacing Cl^+ with Ar^+, it was determined that Cl^+ ions remove that carbon and fluorine primarily through physical sputtering. This finding was supported by an apparent increase in the yield of monoatomic C and F desorbed species when Cl^+ ions were added. Implication of the results is on the etching of tapered HAR channels in 3D NAND. Due to the difference in the etch rates observed when the Cl^+ ions are injected at 0° and 60°, a tapered structure could be smoothed into a straight profile by controlling the direction of the ion flux.

Chapter 5

Molecular Dynamics Study of SiO_2 Nanohole Etching by Fluorocarbon Plasmas

5.1 Introduction

Computer-mediated communication and high-speed information processing have become necessities in our modern society. Such technologies require the capacity to store a large volume of data. Due to its cost efficiency, NAND (i.e., an abbreviation of "Not And") memory devices have been at the forefront in addressing the need for large data storage. Therefore, three-dimensional (3D) NAND devices, which are the latest rendition of NAND memory devices, have been the focal point of much research in the industry [5, 6].

In the fabrication of 3D NAND memory devices, an alternating stack of films (e.g. silicon dioxide (SiO_2) and silicon nitride (SiN)) are deposited on a silicon wafer. To form the memory cells, hole channels must be etched through all the deposited films. Memory cells are formed around each hole channel at the locations of specific film layers (e.g., SiN layers) and the surrounding SiO_2 layers serve as insulating layers. Increasing the number

of memory cells formed around each hole channel requires an increase in the number of stacked film layers, which in turn requires the formation of deeper hole channels. For a hole channel, its aspect ratio (AR) is defined as the ratio of its depth to the diameter of its circular cross-section. Because the memory capacity of the 3D NAND device is dependent on the numbers of deposited film layers and hole channels, the manufacturing of large-capacity 3D NAND memory devices requires etching processes to form high-aspect-ratio (HAR) hole channels.

An etching process to form HAR structures is referred to as HAR etching [5, 6, 24]. The typical ion incident energy of HAR etching for NAND device manufacturing is said to be several keV, possibly up to over 10 keV, although there has been little open discussion on the actual ion energies used in the industry. HAR etching is challenging because of the difficulty in maintaining the circular cross sections and straight-depth profiles of the holes' inner surfaces, upon which memory cells are built [14, 17, 24, 82, 83, 137, 138]. Problems encountered in HAR hole etching include incomplete etch or etch stop with tapered etched hole profiles, which may be caused by the depletion of energetic ions reaching the bottom and/or redeposition of sputtered/desorbed atoms. Twisted etched profiles are also encountered, which may be caused by the deflection of the incoming ions caused by the electric field arising from the electrical charges accumulated on the holes' inner surfaces or collisions of ions with the sidewalls at grazing angles. Clogging and depletion of the hard mask are also encountered in HAR etching [24, 137]. Extensive experimental studies have been performed to investigate how the shape of the mask affects the resulting hole profile [35, 36, 139]. Numerical studies have also been performed to investigate various factors (e.g. neutral-ion flux ratio, the presence of specific radical species) that affect the profiles of HAR hole channels [104, 117, 137, 140].

Reactive ion etching (RIE), i.e., etching by energetic ion impact combined with surface chemical reactions [20, 80, 84], is widely used in semiconductor device fabrication processes, including HAR hole etching for 3D NAND devices. Energetic ions used for RIE are typically generated in chemically reactive plasmas [27, 28, 76–79]. In general,

fluorocarbon (FC)-based plasmas are used to etch SiO_2 and SiN etching [32, 118–121]. It has been known that a surface layer containing FC species (which we call a "mixing layer") is formed on the material surface during such etching processes and can facilitate etching reactions by forming silicon fluorides (SiF_x) and other volatile molecular species [63].

The interactions of gaseous species such as incident ions and sputtered/desorbed species with the inner surfaces of an etched HAR hole channel strongly influence the etched profiles of the hole. In this study, motivated to understand such interactions holistically, we simulate the etching process of a small hole into a SiO_2 film by FC-based plasmas under idealized conditions, using molecular dynamics (MD) simulation [43, 94, 95]. A typical HAR hole channel of 3D NAND memory devices has a diameter of several dozen nanometers and a depth of a few microns. However, in this study, we study an etching process to form far smaller – atomic-scale – holes. This is because we are also partly motivated to understand the processing of atomic-scale structures used in advanced semiconductor devices [80, 84, 116]. Although the etching processes to form nanometer-scale holes can be quantitatively far different from those to form far-larger-scale HAR holes for 3D NAND memory devices, some aspects of the surface processes such as simultaneous etching and redeposition of sputtered/desorbed species on the side walls may be common, given the fact the mean-free paths of gaseous species are far larger than the typical dimensions of such holes.

The rest of this chapter is organized in the following manner. First, we shall discuss the effects of two types of carbon masks – diamond and amorphous carbon (a−C) – on the etched profiles of SiO_2 by performing MD simulations for nanohole etching with those masks by FC ion beams. Second, with a hypothetical ideal mask, the etching mechanisms for the formation of nanoscale holes into SiO_2 by FC ion beams will be further examined. Third, to understand plasma etching, rather than ion beam etching, we shall examine the synergistic etching effects of simultaneous irradiation of energetic FC ions and thermal

FC radicals, by performing MD simulations of etching of a flat surface, rather than a deep hole. The conclusions will be presented in the final section.

5.2 MD Simulation

The interatomic potentials used in MD simulations of this study are based on Stillinger-Weber potentials [48, 49, 108] modified for Si-O-C-F systems [45, 53, 129]. The modified potentials have been used in earlier simulation studies in Refs. 60, 62–65, 71, 74, 114, 116, 117, 129. The van der Waals (vdW) forces [53] are also included in this study. The interatomic potential functions used in this study are briefly summarized in the supplementary material.

In this study, the model material to be etched by energetic ions is SiO_2. The SiO_2 model material was created by initially placing Si and O atoms in the ideal β-cristobalite structure with a lattice constant of 6.978 Å (which is close to the ideal β-cristobalite lattice constant of 7.138 Å) and thermalizing the system at 300 K, as explained in Ref. 74. The initial thickness of the model SiO_2 material is, e.g., 3.5 nm or selected to be sufficiently large, depending on the ion incident energy.

Three sets of simulations are performed in this study. In the first set of simulations, the SiO_2 model material is covered with a carbon mask. The lateral dimensions of the model material covered with a carbon mask are 5.58 nm $\times$ 5.58 nm. Periodic boundary conditions are applied in the lateral directions. Two types of carbon masks are considered; (a) diamond and (b) $a-$C, as shown in Fig. 5.1. Each carbon mask has a hole with a diameter of 4nm in its center. The use of a diamond mask is unrealistic for typical semiconductor processes but we examine it to understand the effects of the hardest carbon mask that we can create self-consistently in our simulation. In this set of simulations, both SiO_2 and carbon masks are etched by the same incident ion flux simultaneously, as

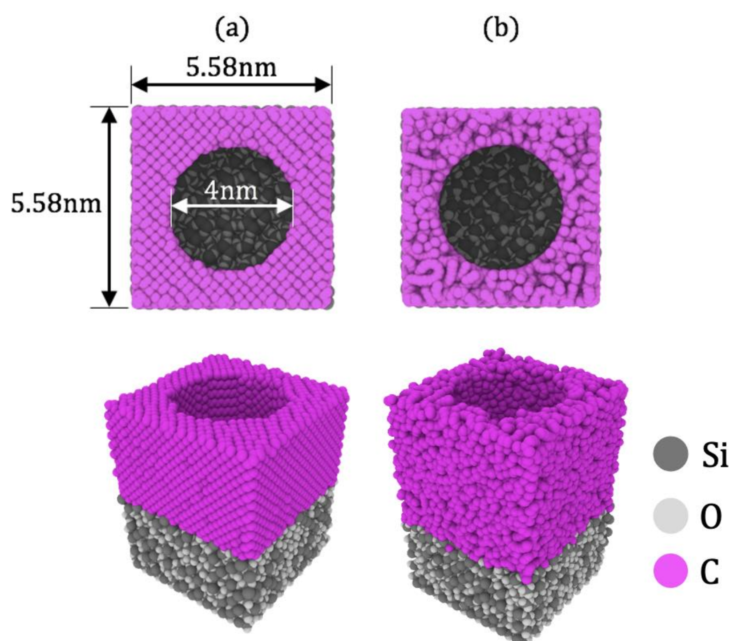

FIGURE 5.1: Schematic diagrams of SiO_2 films with (a) diamond and (b) a−C hard masks. The initial thickness of the SiO_2 films is 3.5 nm and the thickness of carbon masks is (a) 3.7 nm and (b) 5.1 nm. Each carbon mask has a hole with a diameter of 4 nm in its center. As the etching process proceeds in simulation, the thickness of the SiO_2 increases with more SiO_2 being added from the bottom, and therefore the model material represents an infinitely deep SiO_2 film covered with a carbon mask. With periodic boundary conditions imposed in the horizontal directions, the model also represents an infinitely wide surface.

in the real system. The diamond carbon mask has a unit cell of 3.57 Å. Figure 5.1 and all succeeding figures that visualize the model material are rendered with OVITO [141].

In the second set of simulations, the same SiO_2 model material covered with the diamond mask is used but we assume that the mask cannot be etched at all by the incident ions. In the third set of simulations, the SiO_2 model material without any mask is etched. Its lateral dimensions are 4.19 nm × 4.19 nm. With periodic boundary conditions imposed in the lateral directions, it represents an infinitely wide flat surface.

The model material is placed in the simulation box to which periodic boundary conditions are applied in the horizontal (i.e., x and y) directions. The bottom monolayer of the initial model material is fixed in position to prevent vertical drift of the model material during the simulation box due to the momentum transfer from injected ions. The film

is maintained to be thick enough during the simulation. If needed, more SiO_2 is added to the model film from the bottom, as explained below. Initially the model material was thermalized at 300K.

As in the earlier studies (e.g., Refs. 116 and 117), we perform etching simulations by injecting ions cyclically. In each ion injection cycle, an ion is injected into the surface of the model material at normal incidence with a predetermined kinetic energy. The lateral (i.e., x-y) position of impact is selected randomly across the material surface. In this study, incident ions are CF_3^+ as representative ions emitted from FC plasmas. The ion is injected from a position slightly above the material surface to minimize the ion transit time in vacuum. The ion kinetic energy examined in this study is in the range of 200eV to 2,000eV. The injected ions in the simulation are treated as fast neutrals. This approximation is based on the assumption that the injected ions are neutralized by Auger emission upon interaction with a surface [73, 74]. After ion injection, the system (i.e., surface material and injected ions) is left to evolve under constant total energy (i.e., microcanonical) conditions for 700fs. The kinetic energy transfer of the injected ion to the material and the subsequent collision cascade can occur in this period. In addition, during this time period, the majority of sputtered atoms and reflected ions from the inner surface of the etched hole typically have sufficient time to travel across the hole diameter.

At the end of this microcanonical simulation period, atoms not covalently bonded to the material surface (i.e. atoms floating above the material top surface or in the etched hole channel) are removed from the system as volatile etch products. It should be noted that, in this removal process, atoms that are weakly bonded to the material surface by the vdW forces are not removed.

Although fast-moving sputtered or reflected species from the sidewall can reach other areas of the sidewall and be redeposited there, some desorbed species that travel slowly in the open space of the etched hole may be removed from the system prematurely. Therefore, in our simulation, we may underestimate the redeposited materials.

After the microcanonical simulation period, the system is then artificially cooled by gradually decreasing the velocities of all remaining atoms with a Langevin [57] thermostat for 1,200fs. After this Langevin cooling step, the temperature of the model material is then brought to 300K with a Berendsen [58] thermostat for 100fs. Thus, the duration of a single injection cycle is 2,000fs. Atoms that are not covalently bonded to the surface at the end of the cooling step are also removed from the system and counted as etch products. The system at the end of the injection cycle is then used as the material to be etched for the next injection cycle.

Atoms that are weakly bonded to the surface by the vdW forces may thermally desorb over timescales much longer than the ion injection cycle used in our simulation. However, in our simulation, we never observed a large number of weakly bonded atoms built up on the surface, which indicates most weakly bonded atoms desorbed eventually in later ion injection cycles as etch products. Therefore, we believe that the fact that we do not remove weakly bonded atoms from the system in the atom removal processes discussed above would not much affect the simulation results.

During an ion injection cycle, if the volume-averaged temperature of the system exceeds a predefined temperature (1,700K in this study), or the injected ion or recoiled atoms reach the bottom layer of the model material, the simulation of this ion injection cycle is discarded and a sufficiently thick SiO_2 slab is added from the bottom of the model material. After this thicker model material is thermalized at 300K, the next injection cycle starts. This injection cycle is repeated until the ion dose reaches the desired value.

In the third set of simulations, where the SiO_2 model material is etched without a mask, etching yields of SiO_2 by simultaneous incidence of CF_3^+ ions and CF_3 radicals are examined. For this purpose, we repeat the radical irradiation cycle and ion injection cycle alternatingly, as schematically depicted in Fig. 5.2. The ion energy is set at 2,000 eV. The radical injection cycle is essentially the same as the ion injection cycle, except

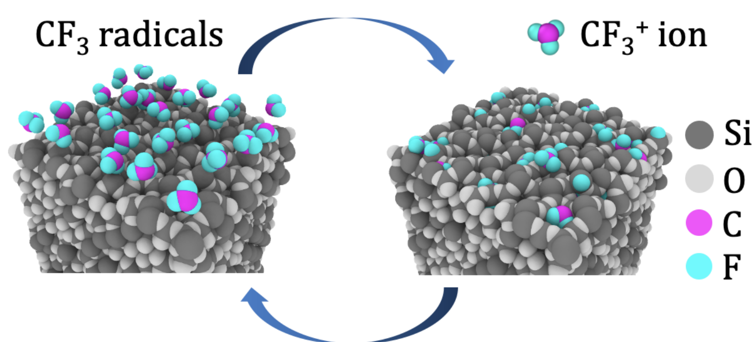

FIGURE 5.2: Alternating CF_3 radical irradiation and ${CF_3}^+$ ion injection to simulate simultaneous radical and ion irradiation of a SiO_2 flat surface.

that multiple radicals (25 or 50 radicals at a time) are sent to the surface at random lateral positions with an incident kinetic energy of each radical species being 0.5eV. The incident angle of each radical species is set to be normal to the surface for the sake of simplicity. As in the ion injection cycle, the radical injection cycle also has the same cooling processes by Langevin and Berendsen thermostats.

In reality, radicals are typically in thermal equilibrium with the background gas, so each radical species should have an average kinetic energy of 0.026 eV for 300 K gas temperature and its incident angle should be distributed uniformly. In the simulation, we use a slightly higher incident energy of 0.5 eV with normal incidence because it can reduce the traveling time of CF_3 radicals in vacuum before reaching the surface. We have observed that the use of 0.5 eV, rather than 0.026 eV, hardly increase the surface temperature or affect the nature of radical deposition on the surface. This is likely because a kinetic energy of 0.5 eV is far below a typical covalent bond energy of a few eV. More discussion on FC deposition by radical irradiation is given in the supplementary material (Appendix D).

5.3 Results and Discussion

5.3.1 Etched Hole Profiles of SiO_2 with Carbon Masks by CF_3^+ Ion beams

First, we examine ion beam etching of SiO_2 with carbon masks. In the simulations, CF_3^+ ions are injected at normal incidence across the top surface with fixed kinetic energy. The resulting hole profile cross-sections of the carbon mask/SiO_2 model material are shown in Fig. 5.3, where the side view of all atoms in a thin vertical layer with a thickness of 0.558nm that passes through the central axis of the model material (Fig. 5.1) is depicted after etching. The etched profiles with the diamond masks are given in Fig. 5.3(a) and those with the a−C masks are in Fig. 5.3(b). The corresponding top-down perspectives of the carbon masks are also shown in Fig. 5.4. Here, the depth of the top-down perspectives is only down to the interface between the carbon masks and the SiO_2 film, so no SiO_2 film is seen in this figure. For both Fig. 5.3 and Fig. 5.4, the ion dose for the 200, 300, and 500eV cases is 6.42×10^{15} cm^{-2} (2,000 injections) and that for the 1,000 eV case is 3.21×10^{15} cm^{-2} (1,000 injections).

In both mask types, the shallowest hole channels are observed at 200eV while the deepest hole channels are observed at 500eV. At 1,000eV, we stopped the simulations after 1,000 ion injections (an ion dose of 3.21×10^{15} cm^{-2}) for both mask types because the mask collapsed completely by then. At 200eV, the rate of FC deposition was faster than the rate of SiO_2 removal. Initially, SiO_2 was etched by the incident ion beam, resulting in the formation of shallow hole channels. However, further ion injections at this energy caused FC film deposition. A similar observation was made in the case of 300eV ion incidence. However, the rate of FC deposition was slower than that at 200eV. At 500eV, deeper etched channels were observed. The channel formed with the diamond mask was much deeper than that with the a−C mask. This was due to the faster etching

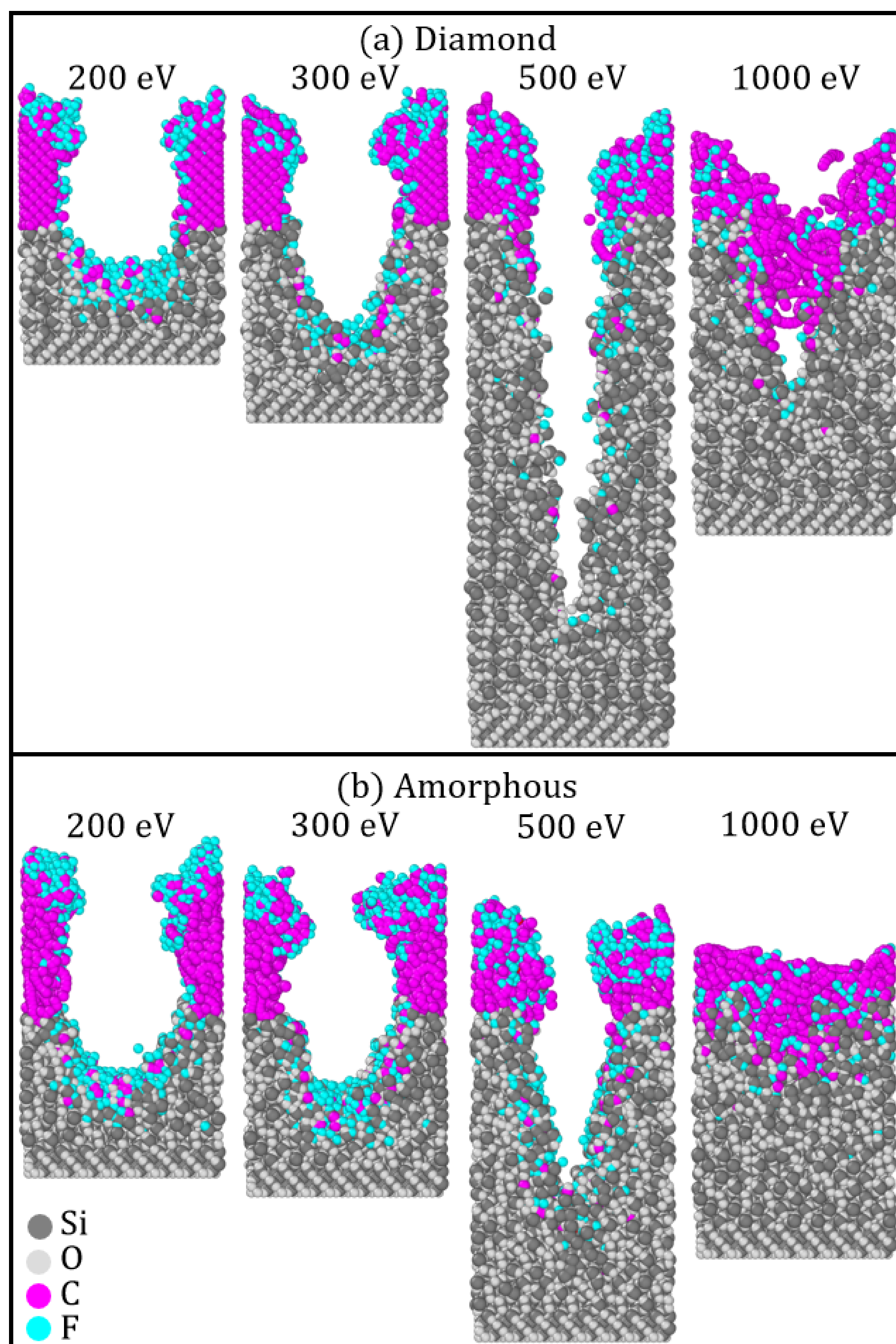

FIGURE 5.3: Centered cross-section slabs of SiO_2 films with the (a) 3.7nm-thick diamond mask and (b) 5.1nm-thick $a-$C mask after CF_3^+ ion incidence with kinetic energy ranging from 200eV to 1,000 eV at normal incidence. The ion dose for the 200, 300, and 500eV cases is 6.42×10^{15} cm^{-2} (2,000 injections) and that for the 1,000 eV case is 3.21×10^{15} cm^{-2} (1,000 injections). The cross-section slab depicted here is a thin vertical layer with a thickness of 0.558nm that passes through the central axis of each model material given Fig. 5.1. The lateral width of each cross section is 5.58nm.

and deformation of the a−C mask hole pattern, as shown in both Fig. 5.3 and Fig. 5.4, which resulted in a smaller SiO_2 surface area exposed to incident ions.

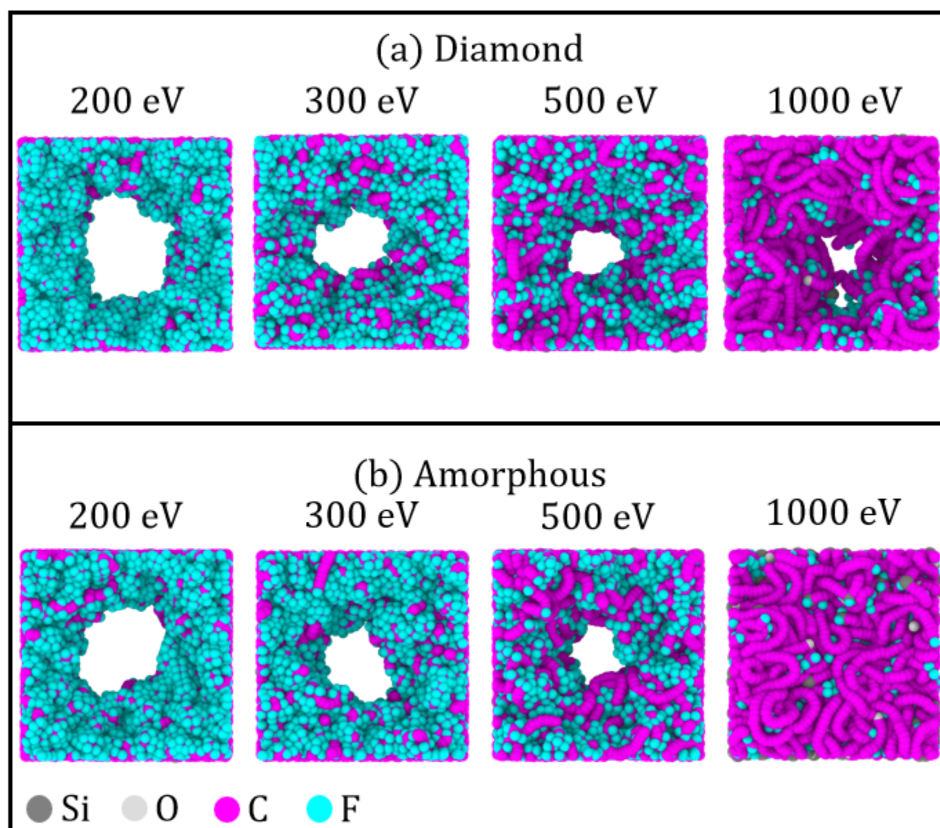

FIGURE 5.4: Top-down perspectives of the SiO_2 films with (a) diamond and (b) a−C masks after $CF_3{}^+$ ion incidence with kinetic energy ranging from 200eV to 1,000 eV at normal incidence. The ion dose for the 200, 300, and 500eV cases is 6.42×10^{15} cm^{-2} (2,000 injections) and that for the 1,000 eV case is 3.21×10^{15} cm^{-2} (1,000 injections). The top-down perspective depicted here is only down to the interface between the mask and the SiO_2 film. Atoms below the interface (i.e., SiO_2) are not shown.

The radial profiles of atomic densities of the SiO_2 film with carbon masks etched by 500eV $CF_3{}^+$ are shown in Fig. 5.5. The corresponding cross-section slabs of the radial profiles are also shown in Fig. 5.5. Here, the four horizontal dashed lines (the locations of which are 1 nm, 2 nm, 3 nm, and 4 nm below the mask- SiO_2 interface) indicate the regions where the atomic densities are calculated. Each atomic number density is calculated from a running average of the number of the corresponding atoms in a cylindrical shell volume with a radial width of 0.025 nm and a depth of 1 nm (between the two horizontal dashed lines) around the central axis of the hole and plotted as a function of the radius. We can estimate the diameter of the hole channel from the atomic density profiles. For

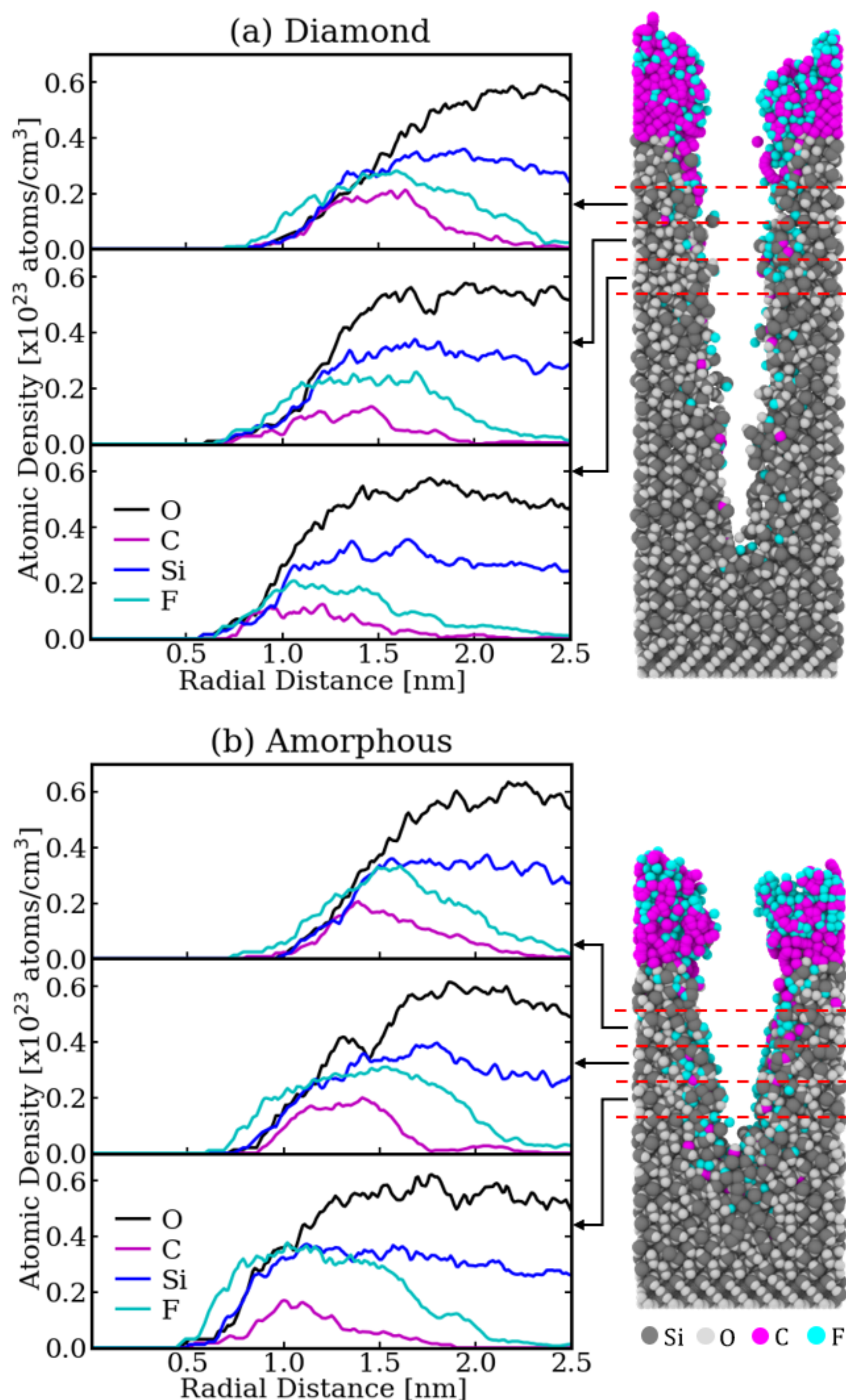

FIGURE 5.5: The radial profiles of the atomic densities of SiO_2 films with (a) diamond and (b) $a-C$ masks etched by CF_3^+ ions. The incident energy of CF_3^+ ions is 500eV and the ion dose was 6.42×10^{15} cm^{-2} (2,000 injections). The cross-section slabs of the SiO_2 films with carbon masks from Fig. 5.3 are also depicted here. The horizontal dashed lines indicate the regions where the the radial profiles are calculated. The radial distance is measured from the central axis of the initial model material.

example, if we define the radius of the etched hole channel as that at which both atomic densities of Si and O exceed 1.0×10^{21} atoms/cm^3, for the region over the depth from 1 nm to 2 nm below the mask–SiO_2 interface [i.e., the top profiles of Fig. 5.5(a) and (b)], the diameters of the etched hole channels there with a diamond and amorphous carbon masks are approximately 1.8 nm and 2.0 nm. These diameters more or less correspond to those of the hole channels seen in the cross sections. The estimated diameters are much smaller than the initial hole diameter of 4nm. This is because the mask was compressed or deformed by the ion injections and the opening diameter became smaller, as also depicted in Fig. 5.3 and Fig. 5.4.

When a clean SiO_2 film is exposed to energetic ion incidence, oxygen (O) atoms are preferentially sputtered than silicon (Si) atoms [63, 117]. This is also observed in Fig. 5.5, where the ratio of the O to Si densities is close to unity near the sidewall surface, much smaller than the stoichiometric ratio of 2 for SiO_2. O atoms are depleted on the sidewalls of the etched SiO_2 holes, which indicates the preferential sputtering of O atoms during the etching process.

The carbon (C) and fluorine (F) atomic densities are also seen to be higher for etching with the $a-C$ mask than that with the diamond mask. This may be caused by the more prominent deformation of the $a-C$ mask, as shown in Figs. 5.3 and 5.4; larger protrusions of the mask collide with incident energetic ions and retard them, making the incident ions less energetic and more prone to deposition. Sputtered C atoms from the mask can be also brought to the etched hole surface.

It is also seen that highly tapered hole channels were formed at 500eV with both mask types. The tapering may be caused by the masking effect since the opening of the hole became smaller as the etching progressed. The tapering could also be attributed to the re-deposition of sputtered/desorbed species on the sidewalls of the etched hole channel.

At 1,000eV, both masks had collapsed by the time the ion dose reached 3.21×10^{15} cm^{-2} (or 1,000 injections). Because the $a-$C mask is structurally weaker than the diamond

mask, the a−C mask was depleted much faster than the diamond mask and, consequently, the etched depth of SiO_2 before the mask collapse was much smaller with the a−C mask than the diamond mask.

5.3.2 SiO_2 Nanohole Etching with an Ideal Mask

Based on what we have observed so far, it seems that the deformation of a mask is unavoidable in the actual beam etching processes even if the incident ion energy is sufficiently low. To mitigate this effect, we may need a much thicker mask possibly with an opening wider than the diameter of the desired etched hole. In this subsection, however, to understand the beam-surface interactions in SiO_2 hole etching better, we consider etching processes with a hypothetical (i.e., ideal) mask that never deforms. To achieve this in MD simulation, we inject ions only through the circular opening of the diamond mask shown in Fig. 5.3. Some ions that enter the edge of the opening may hit some protruding atoms on the sidewall of the mask due to the natural surface roughness, but most incident ions directly reach the SiO_2 surface inside the opening.

Figure 5.6 shows the cross-section profiles of SiO_2 with the ideal masks etched by CF_3^+ ion beams with kinetic energy ranging from 200eV to 2,000 eV at normal incidence. The ion dose is 1.19×10^{16} cm^{-2} (1,500 injections).

It is seen in Fig. 5.6 that, unlike the profiles shown in Fig. 5.3, the opening of the carbon mask essentially remained to be 4 nm in diameter, as intended, because the region of ion incidence was confined to the original mask opening. The carbon mask sidewalls were etched only slightly, if any, by grazing energetic ions. However, in all cases where the hole etching proceeded, the etched hole profiles were highly tapered. Therefore, the tapering is not necessarily caused by the deformation of the mask; it can be caused by the intrinsic tapering (i.e., appearance of a sloped surface that has a high etching yield) [142] as well as the redeposition of sputtered/desorbed species. Some etched holes were

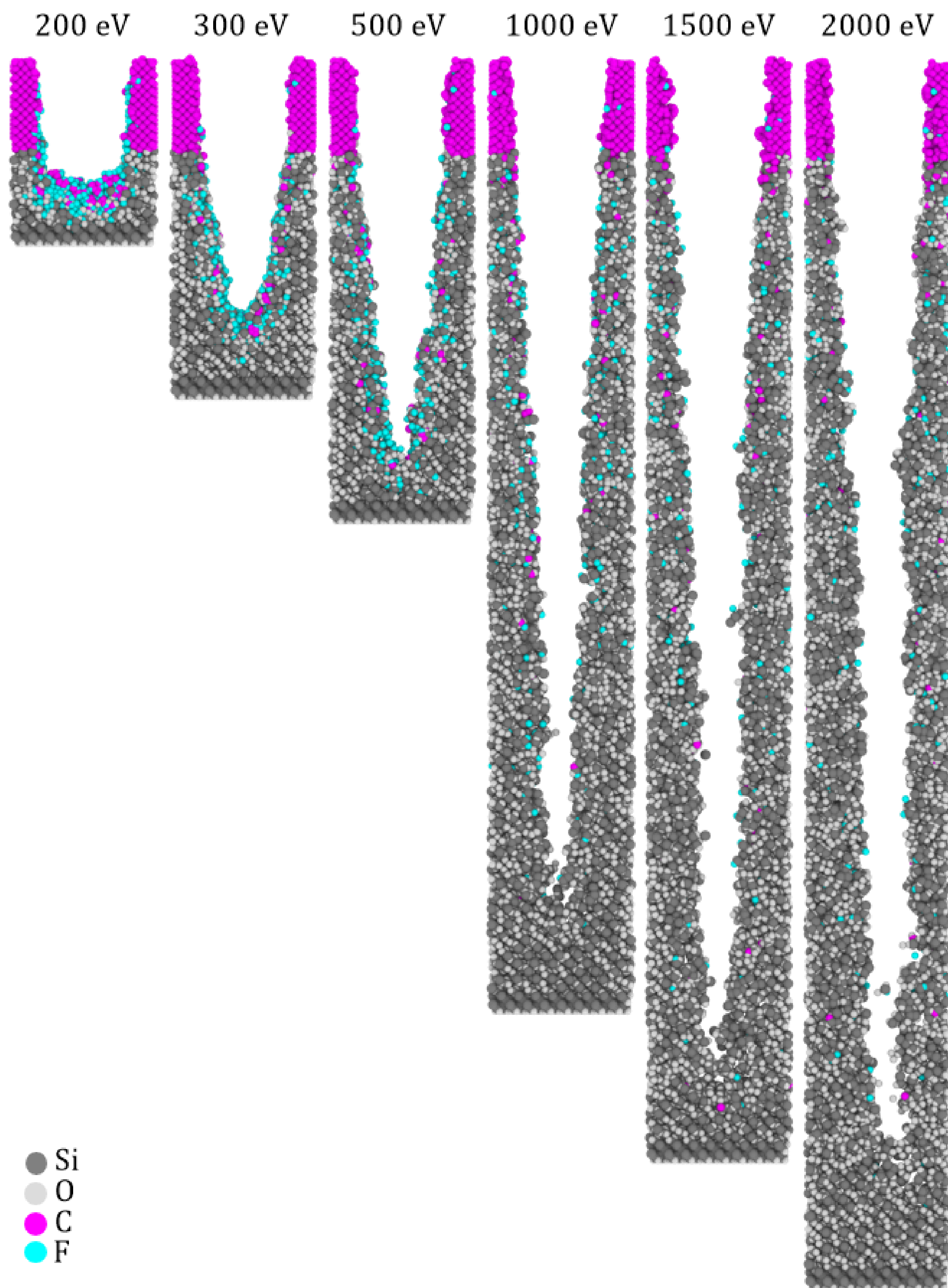

FIGURE 5.6: Centered cross-section slabs of SiO_2 with the ideal masks (as explained in the main text) after $CF_3{}^+$ ion injections with kinetic energy ranging from 200eV to 2,000 eV at normal incidence. The ion dose is 1.19×10^{16} cm^{-2} (1,500 injections).

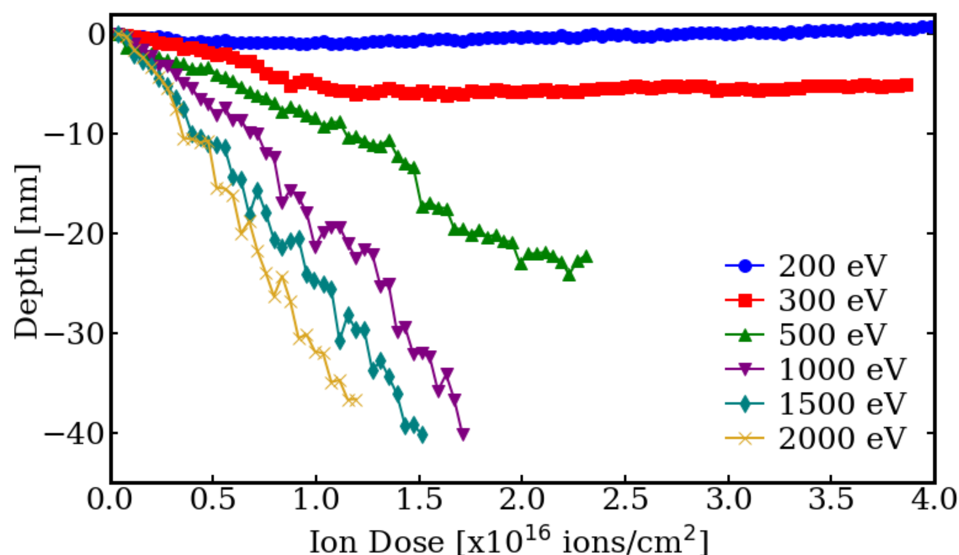

FIGURE 5.7: Depths of the etched hole channels as functions of the ion dose. The etching conditions are the same as those of Fig. 5.6. Zero denotes the initial height of the SiO_2. The lines are guides to the eyes.

somewhat twisted, which may have been caused by stochastically roughened sidewalls that deflect the impinging ions, i.e., stochastic scattering of ions.

For the hole profile at 500eV or higher energy, it is seen that fewer C and F atoms remained on the sidewall near the bottom than in the area near the mask. Therefore, the etching at the bottom must be mostly due to physical sputtering than chemical etching. As the depth increases, desorbed species in the hole channel have more difficulty in escaping upwards and may get re-adsorbed on the sidewall. Redeposited materials on the sidewall may be scraped off by the incident ions and brought back to a deeper region. In this way, at a sufficiently high AR, etched materials can hardly find a way out of the hole unless they form stable volatile species such as CO and SiF_4.

Figure 5.7 shows the dependence of the etched depth on the ion dose. It is seen that, at 200eV, the depth gradually increased as the ion dose increased, which indicates that the deposition rate of an FC layer overtook the etching yield. At 300eV, the depth of the channel remained constant at higher ion doses, i.e., an etch stop occurred. At higher ion energies, the etched depth increased linearly with the ion dose. In all cases here, the AR is less than 10, which may be too small to exhibit an AR-dependent etching yield.

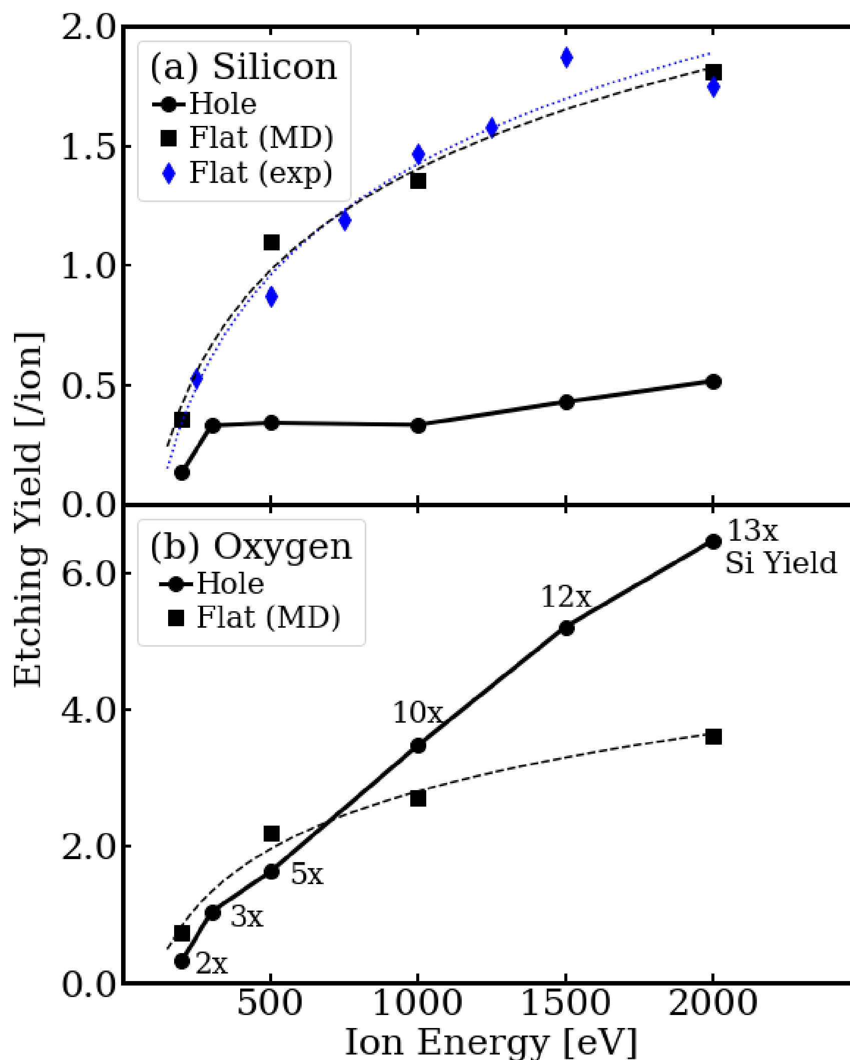

FIGURE 5.8: Nominal etching yields of (a) Si and (b) O atoms (both denoted by filled circles) during the hole etching by 2,000eV CF_3^+ ions of Fig. **??**. The "nominal etching yield" is defined in the main text. The number above each filled square in (b) indicates approximately how many times the nominal etching yield of O atoms is larger than that of Si atoms under the same etching conditions.For comparison, the etching yields of Si atoms for a flat SiO_2 surface by CF_3^+ ion beams obtained from MD simulations [denoted by filled squares] [117] and ion beam experiments [denoted by filled diamonds] [119] are also shown in (a). Similarly, in (b), the etching yield of O atoms for a flat SiO_2 surface obtained from MD simulations [117] are denoted by filled squares. The lines/curves connecting data points are guides to the eye.

Figure 5.8 shows the nominal etching yields of Si [filled circles in (a)] and O [filled circles in (b)] during the hole etching of Fig. 5.6 at 2,000eV. Here the nominal etching yield is defined as the total (i.e., accumulated) number of Si atoms removed from the SiO_2 surface over an ion dose of 1.19×10^{16} cm^{-2} (i.e., 1,500 injections) divided by the ion dose. It should be noted that the removed Si or O atoms counted in Fig. 5.8(a) are not necessarily single Si or O atoms but can be in the form of Si or O-containing molecules or moieties such as SiF_2 or CO.

For comparison, the etching yields of Si or O atoms for flat SiO_2 surfaces obtained from MD simulations [117] and experiments [119] are also shown in Fig. 5.8. The etching yields of a flat surface, i.e., the number of Si or O-containing species removed from the surface per ion injection, are those in steady state, i.e., after a sufficiently large ion dose where the surface chemical compositions no longer change as the etching proceeds. In steady state, therefore, the etching yield of O atoms from the same SiO_2 is twice the etching yield of Si atoms.

It is seen in Fig. 5.8 (a) that the nominal etching yield of Si for the hole etching is much smaller than that for a flat SiO_2 surface. This is because, in the hole etching, many sputtered/desorbed species are redeposited on the sidewall of the hole. In addition, as seen in Fig. 5.6, as the etched depth increases, more incident ions hit the tapered sidewall, rather than the flat surface. The etching yield of a sloped surface (i.e., at oblique ion incidence) is different from that at normal incidence.

It is also seen that, at 200 eV ion incident energy, the ratio of the nominal etching yield of O to that of Si is approximately 2, which is the same as the stoichiometric ratio of SiO_2. However, at 300 eV or higher, the nominal etching yield of O is much larger than twice the nominal etching yield of Si, which indicates that preferential removal of O atoms took place [63, 117]. Additionally, the nominal Si etching yields are nearly the same from 300 eV to 1,000 eV even though, with the same ion dose, the etched depths increased much in this energy range, as shown in Fig. 5.6. The increase of the etched

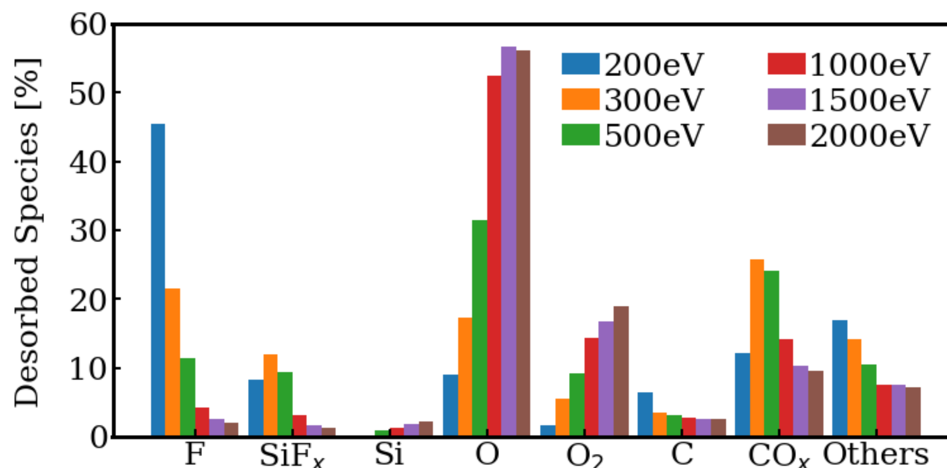

FIGURE 5.9: The percentages of desorbed species during SiO_2 etching by CF_3^+ ions for each ion incident energy. The desorbed species are listed in the horizontal axis wherein SiF_x denotes SiF, SiF_2, SiF_3, and SiF_4; CO_x denotes CO, CO_2, and CO_3; and "Others" primarily contains long carbon chains and C_xF_x species.

depth, therefore, is largely attributed to the volume loss caused by removed oxygen, as seen in Fig. 5.5.

Figure 5.9 shows the percentages of specific desorbed or reflected species among all desorbed/reflected species accumulated during the hole etching processes of Fig. 5.6. It is seen that, at low ion incident energies of 200eV and 300eV, the majority of O-containing desorbed species are CO_x whereas, as the ion incident energy increases, the percentage of single O atoms increases. The high amount of F and C atoms removed at 200 eV is attributed to deposited FC layer. Since an FC layer has formed on the surface, the injected ions are just etching the FC film. At high ion energies, the etching becomes more physical, causing a high percentage of monoatomic O atoms to be removed.

5.3.3 SiO_2 Etching by Simultaneous FC Radical and Ion Irradiation

Figure 5.6 shows that, if the ion incident energy is sufficiently high, the accumulation of FC hardly occurs at the bottom of the etched deep hole by CF_3^+ ion beam etching, and therefore, the nature of etching is essentially physical sputtering and strong tapering

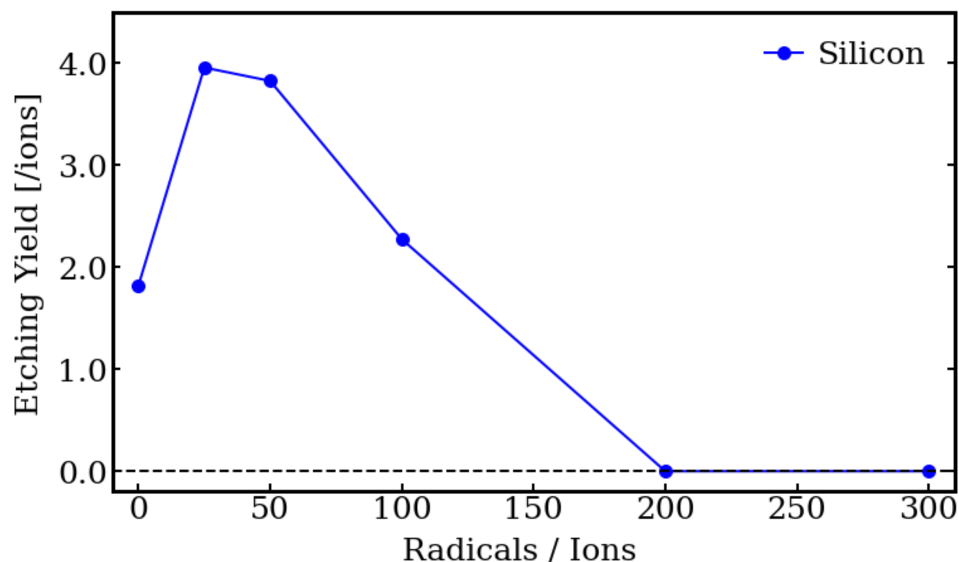

FIGURE 5.10: Etching yield of Si for a flat SiO_2 surface as a function of the radical-to-ion flux ratio. The incident ions are $CF_3{}^+$ at 2,000 eV and the angle of incidence is normal to the surface. Radical species are CF_3. At 200 and 300 radical-to-ion ratios, after the initial etching of the SiO_2 surface, the etching stopped and deposition of an FC layer occurred. The solid lines connecting the data points are the guide to the eye.

occurs. Even in FC plasma etching, where FC radicals are abundant, FC radicals hardly reach the bottom of a deep hole because radicals travel isotropically in the gas phase and tend to stick near the mask opening when they approach the hole channel. However, part of the deposited FC layer may be scraped off and pushed down to a deeper region by incident ions. With such additional FC species, the etching of the bottom surface may become more chemical in nature and the etching yield may increase.

In this section, we examine the etching yield enhancement by the presence of FC radicals. More specifically, we evaluate the etching yield of a flat SiO_2 surface by $CF_3{}^+$ ion injections at normal incidence in the presence of a CF_3 radical flux by MD simulation.

Unlike the nominal etching yields evaluated for Fig. 5.8, the etching yields evaluated here are those in steady state, i.e., after sufficient radical and ion doses. Therefore, the etching yield of O is twice the etching yield of Si, as the etching yield for flat surfaces [117] plotted in Fig. 5.8.

The result of the simulation was plotted in Fig. 5.10. The radical-to-ion flux ratio

was varied from 0:1, 25:1, 50:1, 100:1, 200:1, to 300:1. It is seen that the etching yield increased almost twice in the presence of CF_3 radicals at 25:1 from the etching yield by the corresponding CF_3^+ ion beam only. The etching yield is also nearly the same at 50:1 and 25:1. This was followed by a decrease in etching yield at 100:1. While the presence of a larger number of F and C atoms promotes the formation of volatile silicon fluorides and carbon oxides during ion injection, an excessive accumulation of FC at a larger radical-to-ion ratio retards the surface etching.

It is likely that, in the presence of an optimal amount of CF_3 radicals, the etching becomes more chemical in nature. Although the authors have not confirmed yet, under such conditions, the etching may become more isotropic and could contribute to the lateral etching at the bottom of an etched hole profile, alleviating the tapered etched profile. MD simulation of hole etching by simultaneous FC radical and ion irradiation (i.e., under conditions similar to plasma etching, rather than a beam etching) is beyond the scope of the present study and deferred to future work.

5.4 Conclusions

In this study, MD simulations were performed to simulate etching processes to form nanoholes in SiO_2 by CF_3^+ ion beams. The ions are injected at normal incidence. When relatively thin carbon masks (i.e., 3.7nm-thick diamond and 5.1nm-thick $a{-}$C masks) were used, it is found the masks were notably deformed or even collapsed for incident ions whose kinetic energy was 300eV or higher. Although the use of diamond as a mask is unrealistic for actual processes, the simulation results show that a denser mask is less prone to deformation. Because the periodic boundary conditions were imposed in the horizontal directions over a 5.58nm x 5.58nm square mask model with a 4nm-diameter hole in its center, the shortest distance between the two mask holes was only 1.58 nm. The fact that some mask walls were so thin might have also contributed to the observed deformation or collapse of the mask.

Even with a hypothetical ideal mask that would not deform, it was found that tapered etched holes were formed by CF_3^+ ion beams at sufficiently high ion incident energy. It indicates that tapered etched holes can be formed without the mask deformation. The hole etching with such high ion incident energy is mostly due to physical sputtering. Therefore, the tapered etched holes were likely to be caused by intrinsic tapering [142] (i.e., the appearance of sloped surfaces having high etching yields) and redeposition of sputtered Si-containing species on sidewalls. Furthermore, the preferential removal of oxygen from the sidewalls caused the formation of Si-rich sidewall surfaces.

To form a less tapered, more straight hole, beam etching is thus not sufficient. One needs more lateral etching, which could mitigate the formation of a tapered sidewalls. Although highly reactive charge-neutral radicals are unlikely to reach the bottom of a HAR-etched hole, reactive species deposited near the mask opening may be scraped off by grazing energetic ions and transported to the bottom. Considering such possibilities, we also examined synergetic effects of simultaneous incidence of radicals on ion beam etching of a flat SiO_2 surface by MD simulations. It is found that, with an appropriate flux of CF_3 radicals, the etching yield of a flat SiO_2 surface by CF_3^+ ion injection can double, but excessive exposure to CF_3 radicals causes etch stop. MD simulation of hole etching by simultaneous radical and ion irradiation is beyond the scope of the current study and deferred to future work.

Chapter 6

General Conclusion

In this research, classical MD simulations supported by ion beam experiments has been done to provide insights in HAR etching in the fabrication process of 3D NAND flash memory devices.

In Chapter 2, MD simulations for the scattering of Ne^+, Ar^+, and Xe^+ ions with ion energy of 1,000eV injected at grazing-angle ($\leq 20^\circ$) ion incidence on smooth and rough Si and SiO_2 surfaces were performed. This was done to understand the effect of atomic-scale roughness on the scattering properties of energetic ions at the sidewall of HAR channels. The results showed that surface roughness broadens the reflection-angle and the azimuthal-angle distribution. Though regardless of the surface morphology, the reflection-angle distribution showed that the majority of the ions were reflected specularly while the azimuthal-angle distribution showed minimal deflection when $\theta_i \leq 10^\circ$. Additionally, the surface roughness reduced the mean kinetic energy of the ions upon scattering. From the scattering simulations in this chapter, it was found out that the reflection probabilities were near unity when $\theta_i = 5^\circ$. Additionally, it was observed that for a crystalline surface, ions with low ion energy (i.e. 100eV) could channel through the crystal structure, and reduce the reflection probability. The reflection probabilities obtained from the MD simulation were also compared to SRIM simulation. From the comparison, it was observed

that SRIM simulations underestimate the reflection probabilities in comparison to MD simulations, especially at lower ion energy. The difference was attributed to the fact that SRIM is a binary collision model. Unlike in MD simulations, the ions in SRIM simulations only interact with one atom from the material surface. As such, it was determined that MD has higher accuracy than SRIM.

In Chapter 3, MD simulations of SiO_2, SiN, and ON bilayer model etched by ${CF_3}^+$ ions injected at normal incidence were performed. Etching yields of SiO_2 and SiN obtained from MD simulations were compared to experimental etching yields wherein good agreement was attained. In the etching of ON bilayer by low energy ions, the thickness of the mixing layer was less than the initial thickness of the oxide layer. As such, the etch rates of oxide and nitride layers could be observed separately. At high ion energies, a mixing layer thicker than the initial thickness of the oxide film would be formed. As such, a single etch rate was observed. From the MD simulations, it was inferred that in the etching of ONON multilayer, the overall etch rate would be dependent on the thickness of the films, as well as the ion incident energy. It is possible that in ONON multilayer etching in 3D NAND devices, the non-uniformity of the deposited films could lead to varying etch rates across the horizontal surface. Due to this, the etch front could be deflected as it passes the interface of the films resulting to the bending observed in actual HAR etched channels. Additionally, the desorbed species obtained from the simulations showed that physically sputtered species increases with increasing ion energy. Opposing trend on the Si-containing desorbed species was also observed between 200eV and 2,000eV ion energies. In HAR etching, as the aspect-ratio increases, there is higher possibility of the desorbed species to be redeposited on the sidewalls of the hole channels resulting to the tapering of the etched channels.

In Chapter 4, MD simulations to study the etching of SiO_2 and SiN by chlorine-containing fluorocarbon plasmas were performed. This was done by comparing the simulations of SiO_2 and SiN etched by ${CF_3}^+$ ions with and without Cl^+ ions injected at 0° and 60°. Interatomic potential models describing F–C–Cl interactions were first developed.

To validate the models, etching yields from the MD simulations per ion type were compared to experimental etching yields wherein good agreement was attained. Comparing the MD simulations of SiO_2 etched by CF_3^+ ions with and without Cl^+ ions, minimal change in the etch rate was observed when the ions are injected at 0°. For SiN, similar trend was only observed when the ion injected at normal incidence has an ion energy $\geq 1,000eV$. When the ion energy is 500eV, the etch rate was reduced due to the deposition of a passivating FC film that inhibited the etching. In contrast, when the ions are injected at 60°, a 1.6x increase in the etch rate was observed upon addition of Cl^+ ions to the etching both SiO_2 and SiN by CF_3^+ ions. Based from the results, it was concluded when thick mixing layer is formed on the material surface, the kinetic energy of the Cl^+ ions are spent on etching the C and F from this layer. It is not that Cl^+ has no effect to the etching when injected at 0°. Since an optimum mixing layer is needed in the etching by fluorocarbon plasmas, the etching by Cl^+ ions is negated by the deposition of the C and F atoms to form the mixing layer. When the ions are injected at 60°, the etching becomes favourable to physical sputtering, thus the need to deposit the C and F atoms to facilitate fluorocarbon etching is lessened. Consequently, an increase in the etch rate would be observed. To further support the findings from the MD simulations, additional simulation were performed wherein Cl^+ ions were replaced with Ar^+. Based from the results, it was concluded that Cl^+ ions primarily etch the C and F atoms by physical sputtering even at normal incidence except for SiN at 500eV. This was also evidenced by the apparent increase in the monoatomic C and F desorbed species when the films were etched by CF_3^+ ions with Cl^+ ions. From the results, a mechanism to smoothen tapered structure in HAR etched channels was proposed in this chapter.

In Chapter 5, MD simulations to form nano-hole channels in SiO_2 film with a diamond carbon mask and an $a-$carbon mask by CF_3^+ ions were performed. Based from the comparison of the etching with a diamond carbon mask and an $a-$ carbon mask, a less dense mask have a higher probability of collapsing. As such, it was concluded that the use of a denser mask would be more advantageous in the etching of hole channels with high

aspect-ratio. Due to this, etching simulations of SiO_2 film with a diamond carbon mask wherein the CF_3^+ ions were constrained within the defined hole pattern of the mask were performed. The results showed that even when the deformation of the mask was greatly lessened, tapered hole channels would still form. As such, it was concluded that the redeposition of the sputtered atoms contribute significantly to the tapering phenomenon which was also exacerbated by the nanometer-scale size of the hole pattern. Additionally, the sidewalls of the tapered channels were observed to be Si-rich due to the preferential removal of oxygen. Based on the desorbed species, it was also concluded that the HAR etching process predicted in the simulation is dominated by physical sputtering. The effect of the carbon and fluorine flux at the bottom of the hole channel was also studied by bombarding a flat SiO_2 substrate with CF_3 radicals and CF_3^+ ions. It was concluded that there exists a process window from 25:1 and 50:1 radical-ion ratio where etching yields of Si and O atoms were doubled. It was concluded that the main effect of the radicals in etching is to promote chemical sputtering and to balance out the physical sputtering.

To summarize, this research was done to study the HAR etching in the the fabrication of 3D NAND devices. Chapter 2 provided insight on the effect of atomic scale roughness on the scattering of ions as it hit the HAR sidewalls at grazing angle. In Chapter 3, the etching of oxide-nitride bilayer representing the alternating ONON layers in actual 3D devices showed how the thickness of the mixing layer affects the etch rate. In Chapter 4, other plasma chemistry that can be used in HAR etching was explored. Though MD simulation of hole channel etching was also done as shown in Chapter 5, the findings of this research could be incorporated in profile simulation that can simulate the macroscopic evolution of HAR profiles. In general, this research has shown that MD simulation supported by ion beam experiment could provide insights in understanding the ion scattering and etching process in semiconductor device fabrication. Since the feature size in semiconductor devices continues to shrink, the use of MD simulations is becoming more relevant due to the possibility of direct comparison between simulation and experiment.

Appendix A

Inert-gas Ion Scattering at Grazing Angle Incidence on Si and SiO_2 Surfaces – Supporting Results

In Chapter 2, MD simulations of the scattering of Ne^+, Ar^+, and Xe^+ ions on smooth and rough Si and SiO_2 surfaces were discussed. The reflection-angle distributions and the azimuthal-angle distributions of the ions injected with 1,000 eV ion energy were shown in Figs. 2.3 and 2.3 respectively. In Ch. 2, the scattering of ions with 100eV energy was also explored. In this appendix, the reflection-angle distributions and the azimuthal-angle distributions of the ions injected with 100 eV ion energy are shown in Figs. A.1 and A.2 respectively.

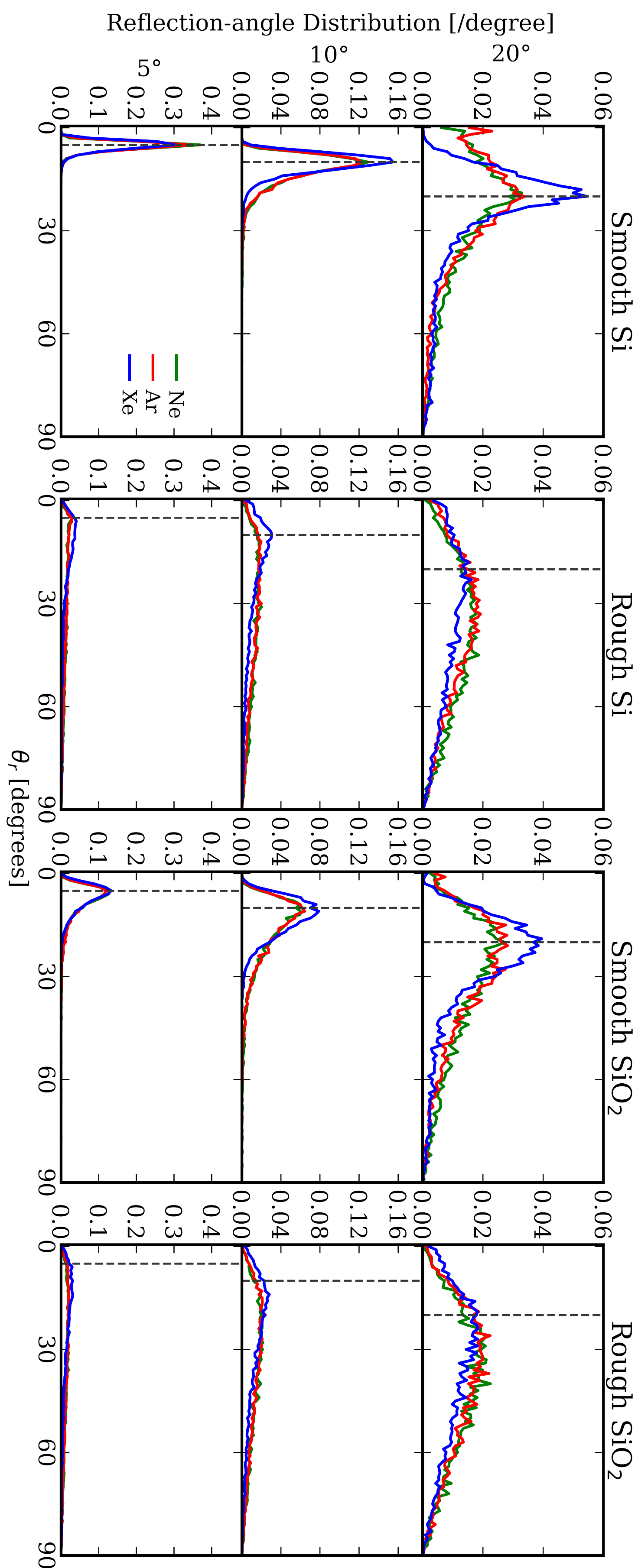

FIGURE A.1: Reflection-angle distributions $F(\theta_r)$ of Ne^+ (green), Ar^+ (red) and Xe^+ (blue) ions reflected on the smooth and rough Si and SiO_2 surfaces defined in Fig. 2.1. The ion incident energy is 100 eV and angles of incidence are 5°, 10° and 20°. The vertical black dashed line indicates the specular angle in θ_r. Note that incident ions may be trapped in the material.

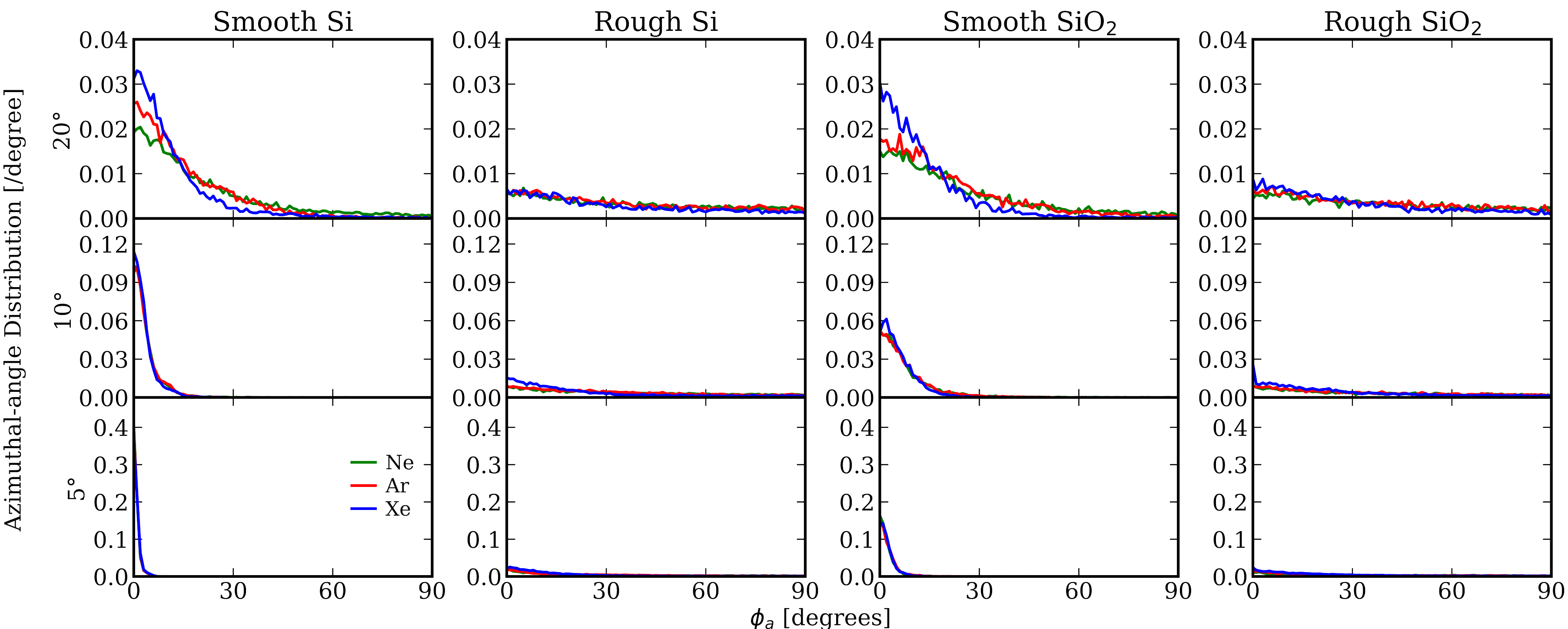

FIGURE A.2: Azimuthal-angle distributions $G(\phi_a)$ of Ne^+ (green), Ar^+ (red) and Xe^+ (blue) ions reflected on the smooth and rough Si and SiO_2 surfaces defined in Fig. A.2. The ion incident energy is 100 eV and angles of incidence are 5°, 10° and 20°. Because of the symmetry $G(\phi_a) = G(-\phi_a)$, $G(\phi_a)$ is plotted only for positive ϕ_a. The angle of $\phi_a = 0$ is the direction of specular reflection and $|\phi_a| < 90°$ indicates the forward scattering. It is seen that, at an incident angle of 20°, Ne^+ and Ar^+ ion incidence may result in backward scattering (i.e., $|\phi_a| > 90°$). Note that incident ions may be trapped in the material.

Appendix B

Etching of ONON Multilayer by CF_3^+ Ions

In Chapter 3, MD simulation of the etching ON bilayer by CF_3^+ ions injected at normal incidence with ion energy from 200eV to 2,000eV were discussed. To study the etching of an actual ONON multilayer, MD simulation of an ONON multilayer etched by CF_3^+ ions injected at normal incidence with ion energies from 200eV to 6,000eV were performed. The change in depth as a function of ion dose is plotted in Fig. B.1. Until an ion energy of 3,000eV, change in the etch rate as the material transitions from oxide to nitride and vice versa can be observed in Fig. B.1. Since a much thicker oxide film was used in these simulations unlike in Ch. 3, a single etch rate was only observed at much higher energies ($>$ 3,000eV). Note that the results from 3,000eV to 6,000eV are preliminary data that requires further studies and verification with experiment. Nonetheless, this observation supports the conclusion in Ch. 3 wherein the change in etch rate is dependent on the thickness of the films and the ion energy used. The thickness of the films used in the simulations are similar to the thickness of ONON films deposited on Si wafers provided by Lam Research Corp. This was done to have a direct comparison between MD simulation and experiment.

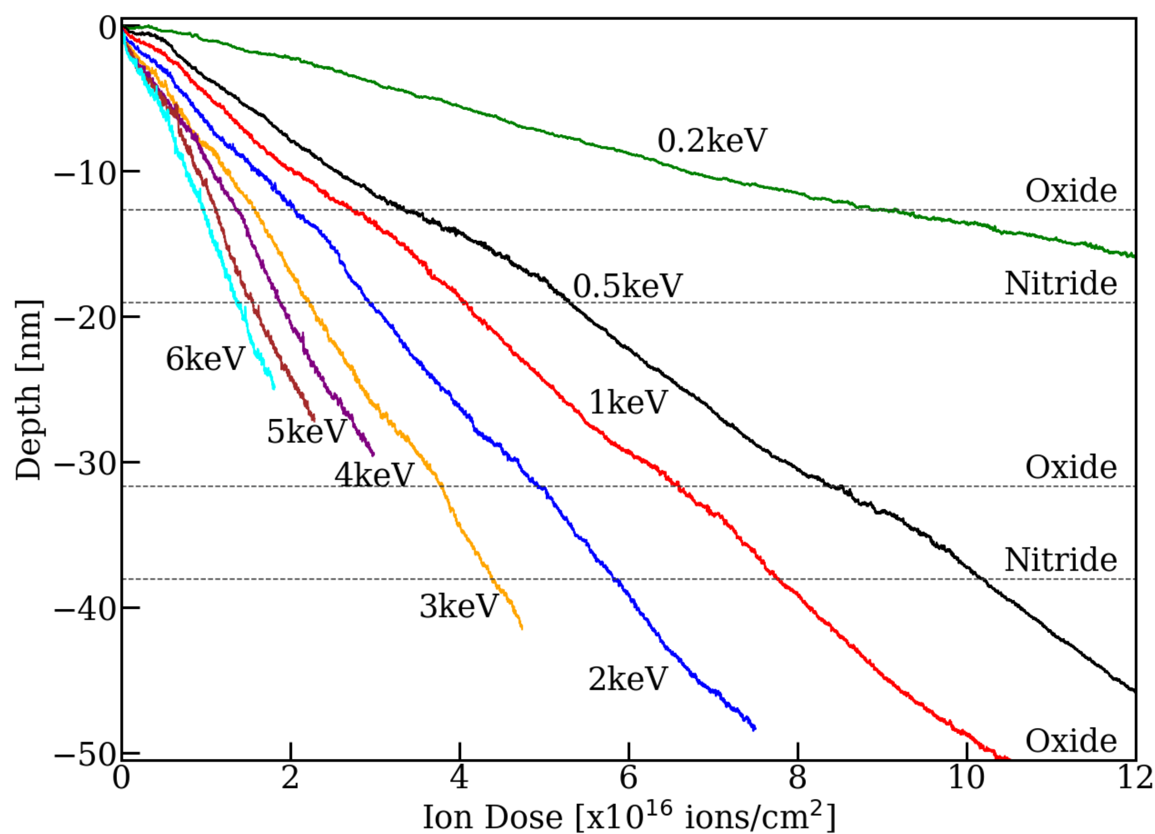

FIGURE B.1: The change of the surface height (i.e., depth) as a function of ion dose with ion incident energies from 200eV to 6,000eV, obtained from MD simulation. The dashed lines indicate the interface of the oxide and nitride.

Appendix C

MD Simulation of Oxide and Nitride Etching by CF_3^+ and Cl^+ – Supporting Results

C.1 Fluorocarbon and Chlorine Interatomic Potential Model

The three-body V_3 potential models for all possible combinations of chlorine interacting with the system containing Si, O, N, C, and F are summarized in this appendix. Details of the calculations had already been discussed in Chapter 4.

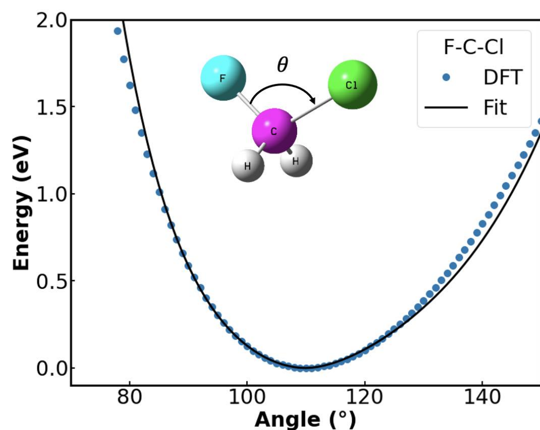

(a)

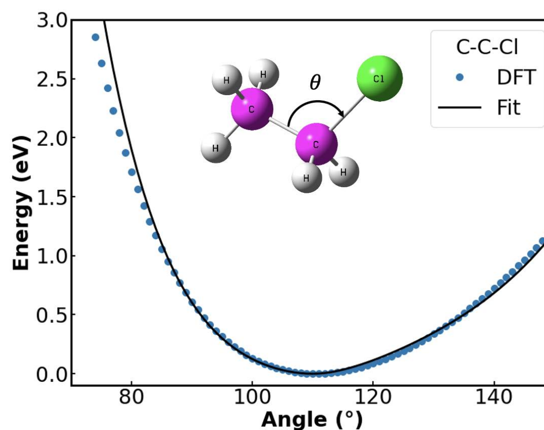

(b)

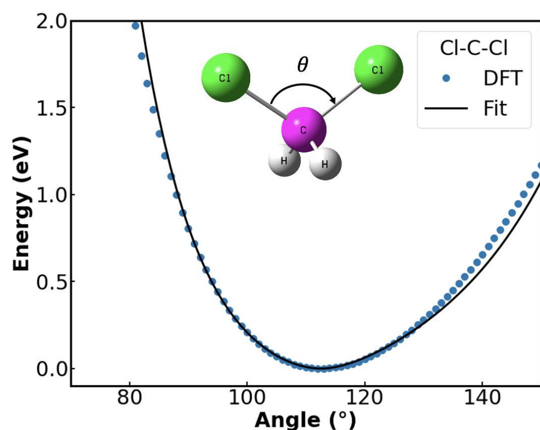

(c)

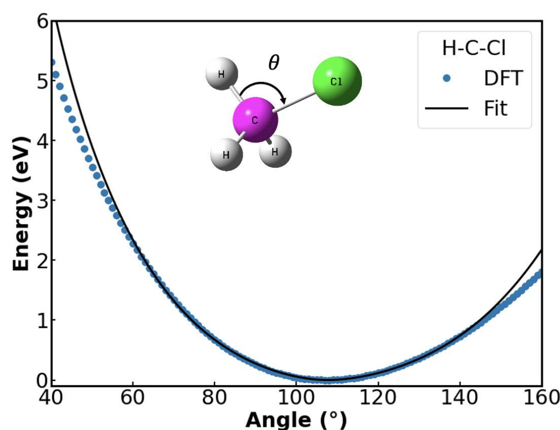

(d)

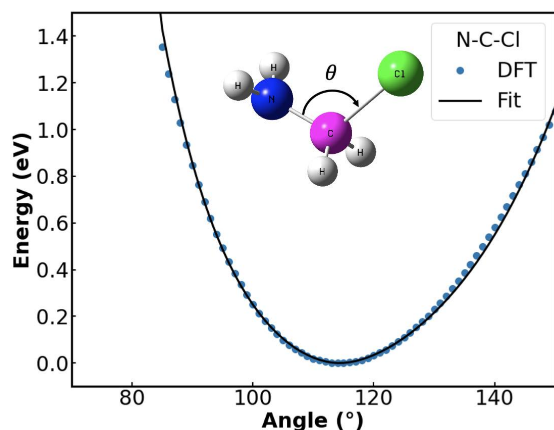

(e)

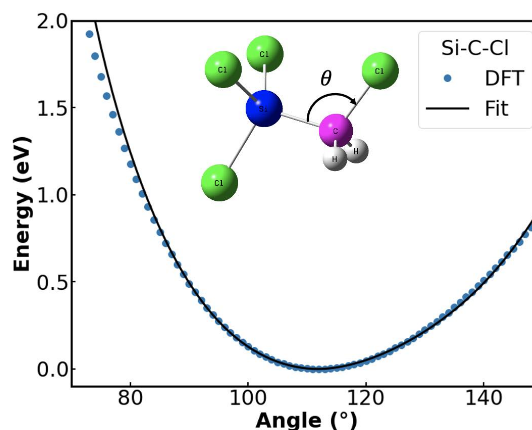

(f)

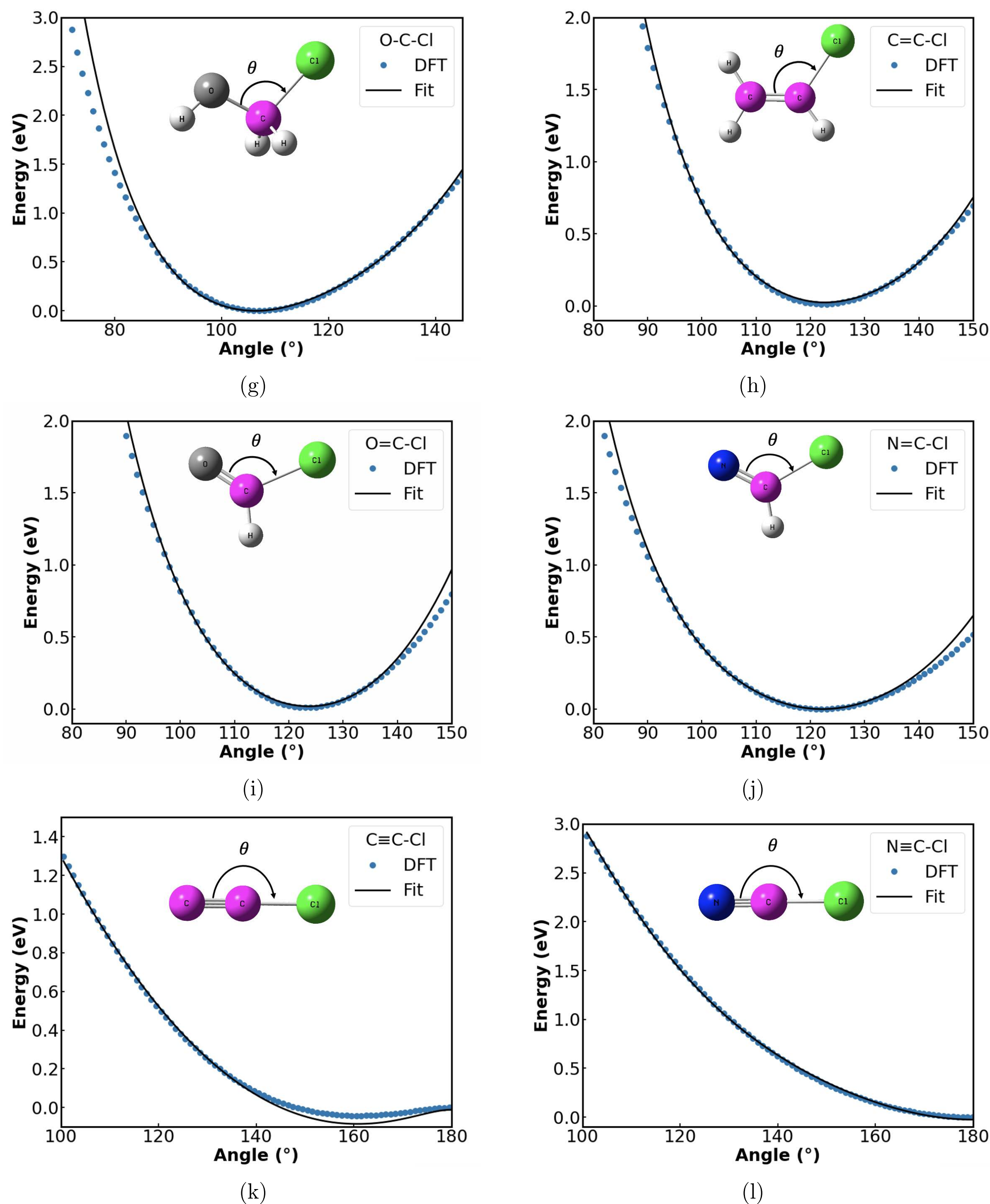

FIGURE C.2: The three-body V_3 potential energies are plotted as a function of the angle θ for various configurations of Cl with C as the center atom. The data points are obtained from DFT calculations, and the curves are obtained from fitting V_3 interaction described by Eq. 1.8. The DFT calculations were done on (a) chlorofluoromethane CH_2ClF; (b) chloroethane CH_3CH_2Cl; (c) dichloromethane CH_2Cl_2; (d) chloromethane CH_3Cl; (e) chloromethylazanide CH_2NH_2Cl; (f) trichloro(chloromethyl)silane $Si(CH_2Cl)Cl_3$; (g) hydroxychloromethyl-radical CH_2ClOH; (h) vinyl chloride C_2H_3Cl; (i) formyl chloride $CHClO$; (j) chloromethylideneazanide $CHClN^-$; (k) 2-chloroethynyl C_2Cl; and (l) cyanogen chloride CNCl. The bond lengths of all atoms are maintained. Only the angle θ was varied without changing the azimuthal angle.

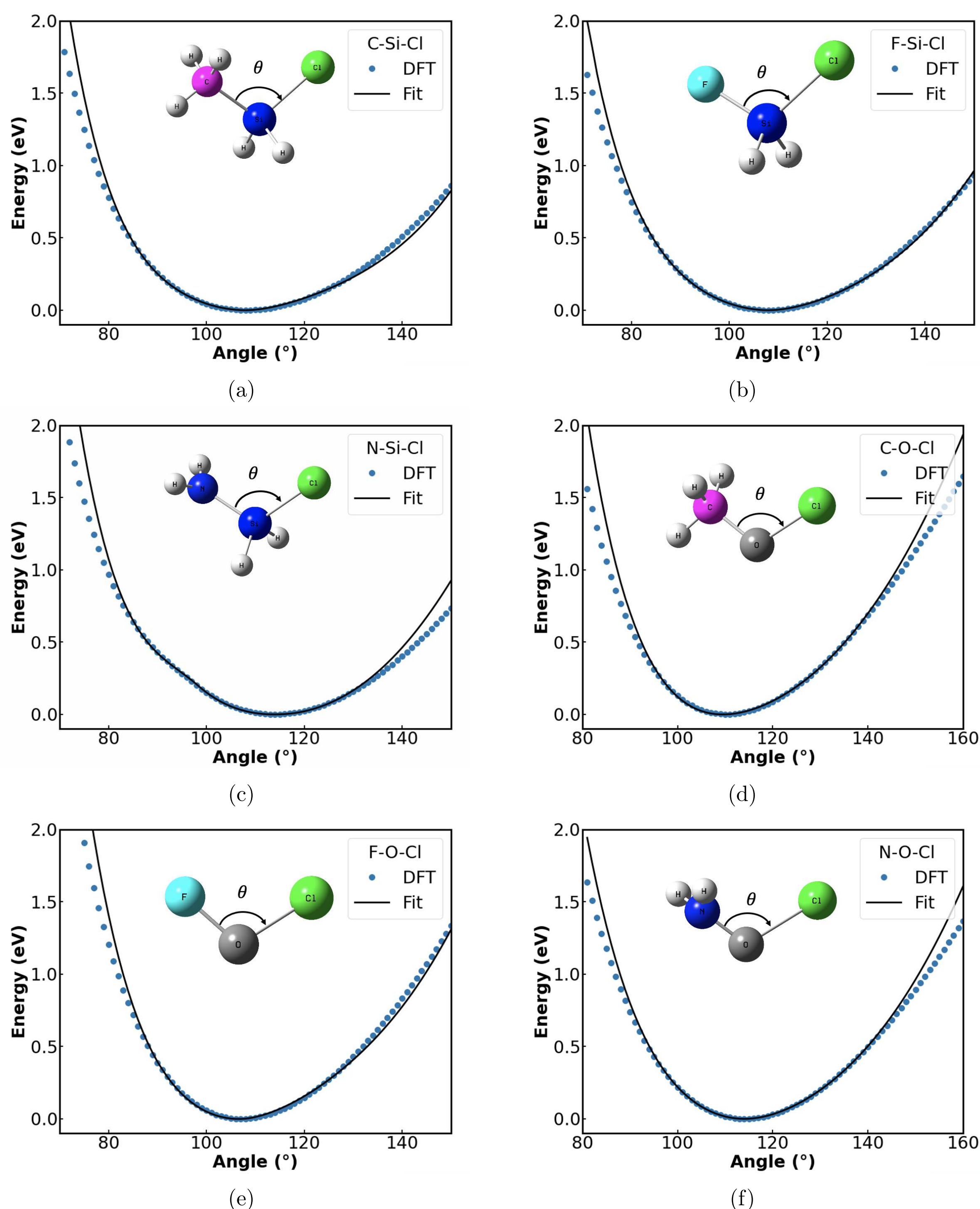

FIGURE C.3: The three-body V_3 potential energies are plotted as a function of the angle θ for various configurations of Cl with (a)–(c) Si and (d)–(f) O as the center atom. The data points are obtained from DFT calculations, and the curves are obtained from fitting V_3 interaction described by Eq. 1.8. The DFT calculation were done on the following molecules: (a) chloro(methyl)silane $ClCH_3SiH_2$; (b) chlorofluorosilane $ClFSiH_2$; (c) alpha-Chlorosilanamine ClH_4NSi; (d) methyl hypochlorite CH_3ClO; (e) chloro hypofluorite ClFO; and (f) amino hypochlorite ClH_2NO. The bond lengths of all atoms are maintained. Only the angle θ was varied without changing the azimuthal angle.

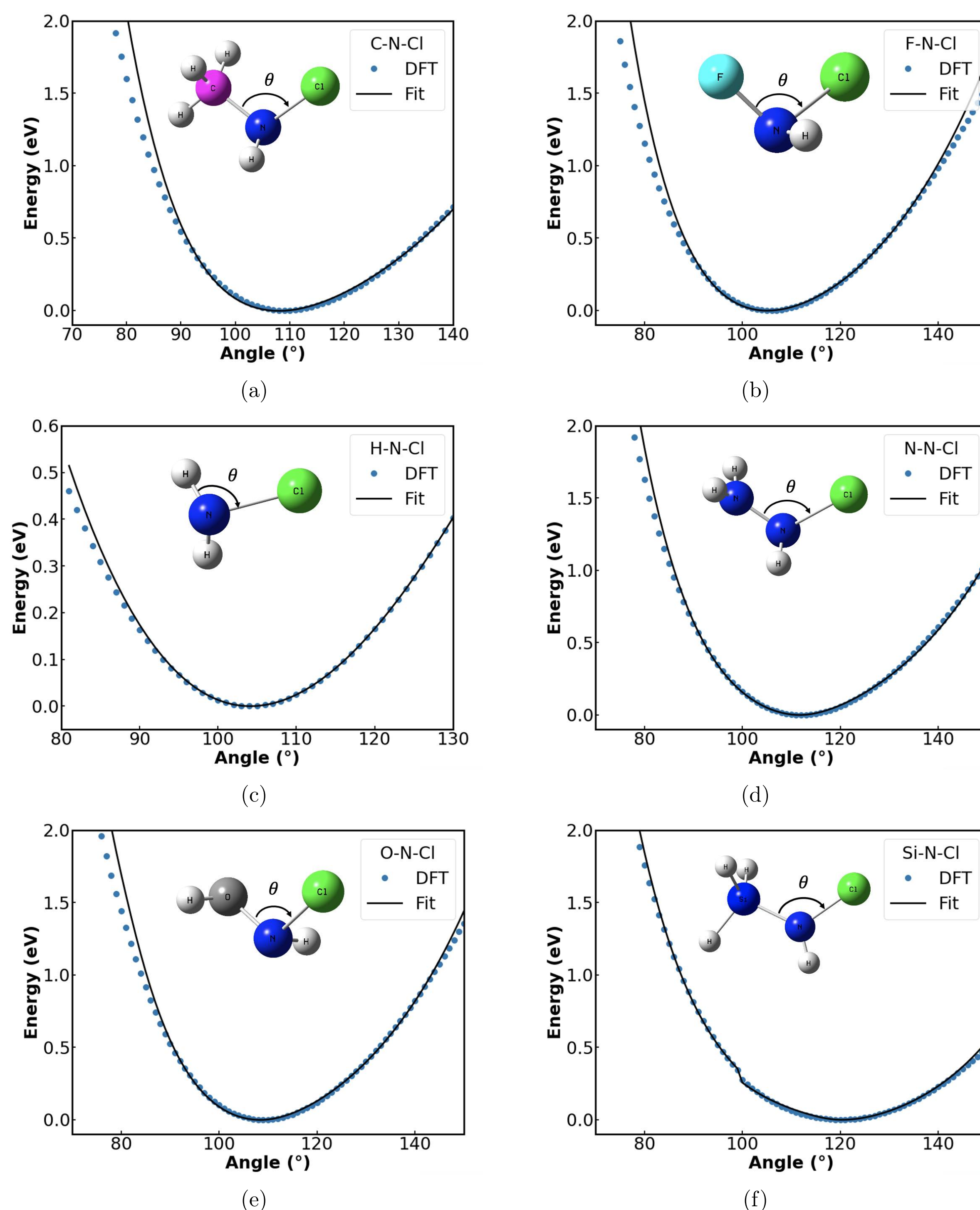

FIGURE C.4: The three-body V_3 potential energies are plotted as a function of the angle θ for various configurations of Cl with N as the center atom (single bonds). The data points are obtained from DFT calculations, and the curves are obtained from fitting V_3 interaction described by Eq. 1.8. The DFT calculation were done on the following molecules: (a) methylchloroamine CH_4ClN; (b) ClFHN; (c) chloramine NH_2Cl; (d) 1-chlorohydrazine ClH_3N_2; (e) hydroxylamine ClH_2NO; and (f) SiH_4ClN. The bond lengths of all atoms are maintained. Only the angle θ was varied without changing the azimuthal angle.

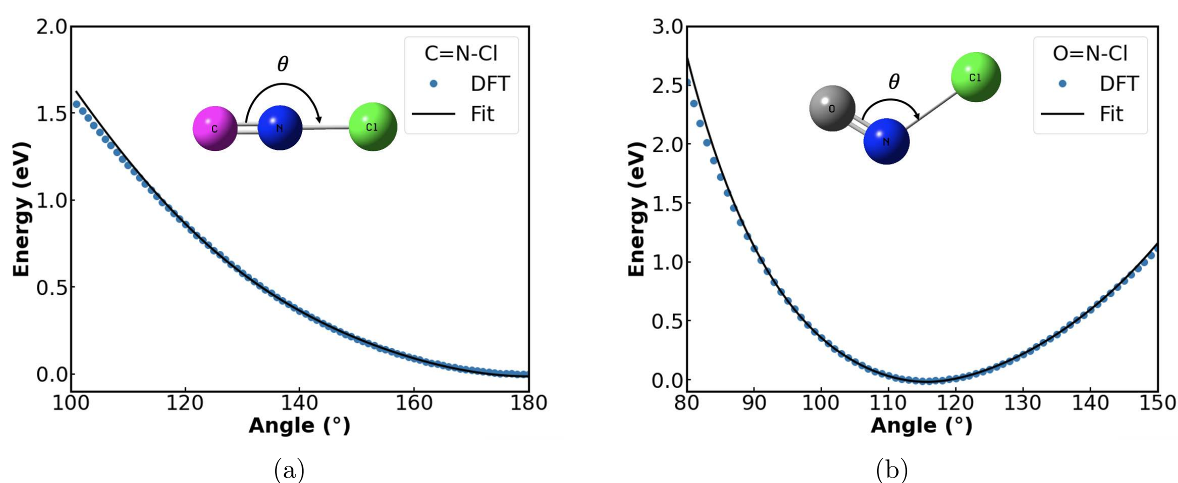

(a) (b)

FIGURE C.5: The three-body V_3 potential energies are plotted as a function of the angle θ for various configurations of Cl with N as the center atom (double bonds). The data points are obtained from DFT calculations, and the curves are obtained from fitting V_3 interaction described by Eq. 1.8. The DFT calculation were done on the following molecules: (a) chlorine isocyanide CClN; and (b) nitrosyl chloride NOCl. The bond lengths of all atoms are maintained. Only the angle θ was varied without changing the azimuthal angle.

C.2 Depth Profiles of SiO_2 and SiN Etched by CF_3^+ and Cl^+

The depth profiles of atomic densities for both SiO_2 and SiN etched by CF_3^+ ions with Cl^+ ions and just CF_3^+ ions injected at 0° and 60° are summarized in this appendix.

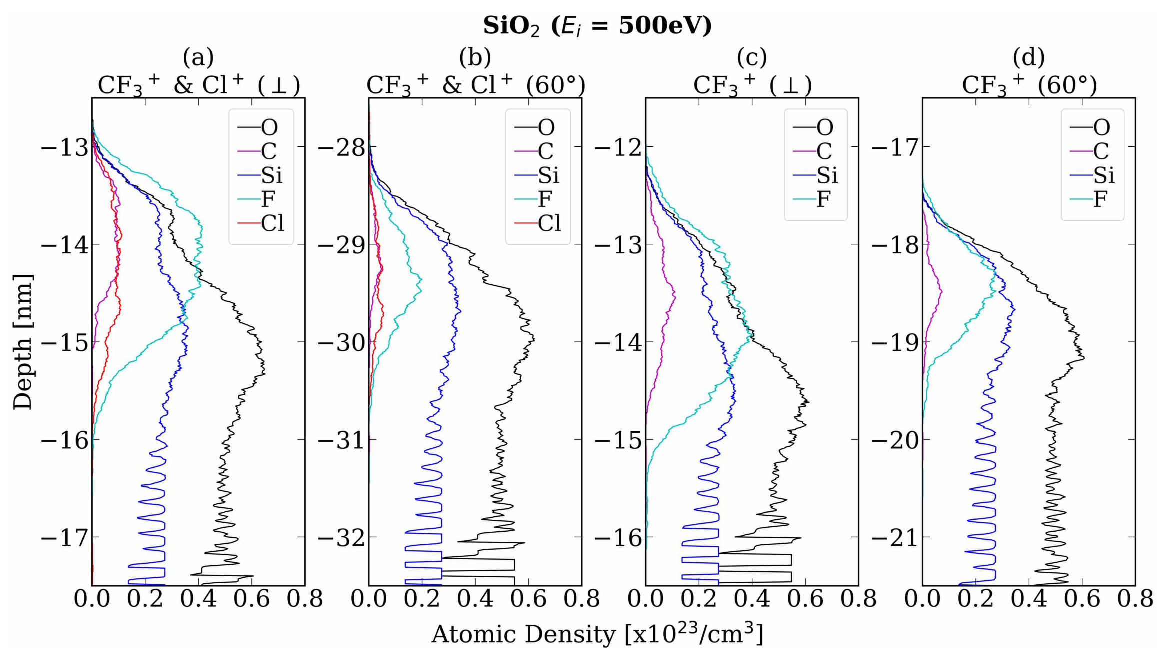

FIGURE C.6: The depth profiles of the atomic densities for SiO_2 etched by 500eV CF_3^+ & Cl^+ injected at (a) 0° and (b) 60°, compared to SiO_2 etched by 500eV CF_3^+ ions injected at (c) 0° and (d) 60°. The depth profiles were taken at the same ion dose of 2.85×10^{16} CF_3^+ ions/cm^2. The origin of the vertical axis is the position of the material's top surface prior to etching. The vertical axes have different ranges but same increment.

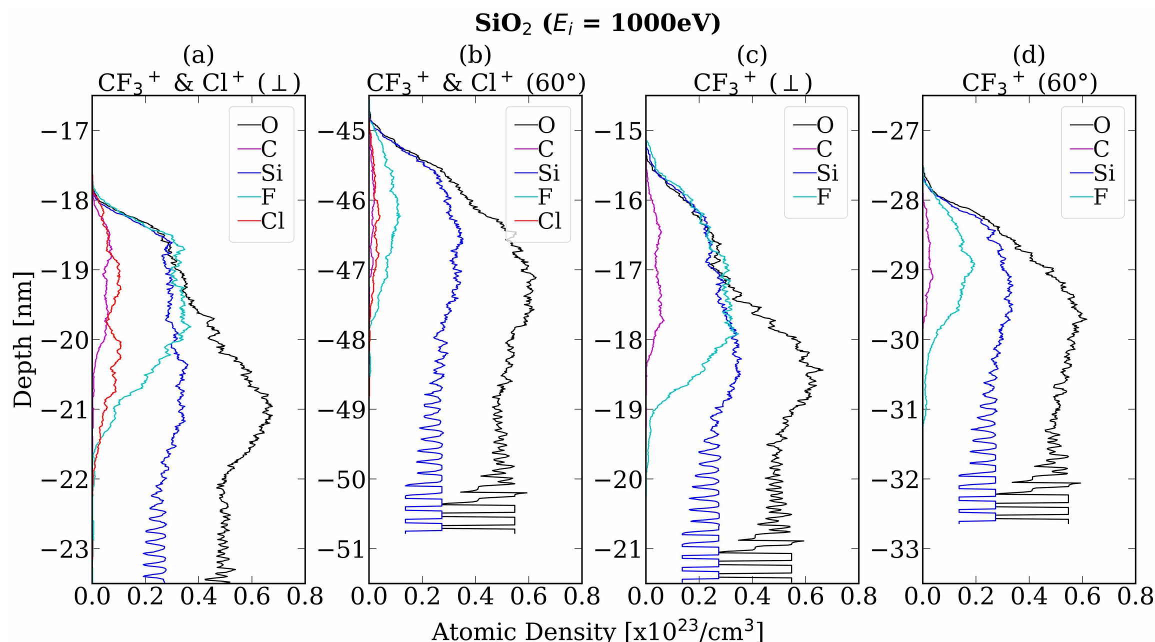

FIGURE C.7: The depth profiles of the atomic densities for SiO_2 etched by 1,000eV CF_3^+ & Cl^+ injected at (a) 0° and (b) 60°, compared to SiO_2 etched by 1,000eV CF_3^+ ions injected at (c) 0° and (d) 60°. The depth profiles were taken at the same ion dose of 2.79×10^{16} CF_3^+ ions/cm^2. The origin of the vertical axis is the position of the material's top surface prior to etching. The vertical axes have different ranges but same increment.

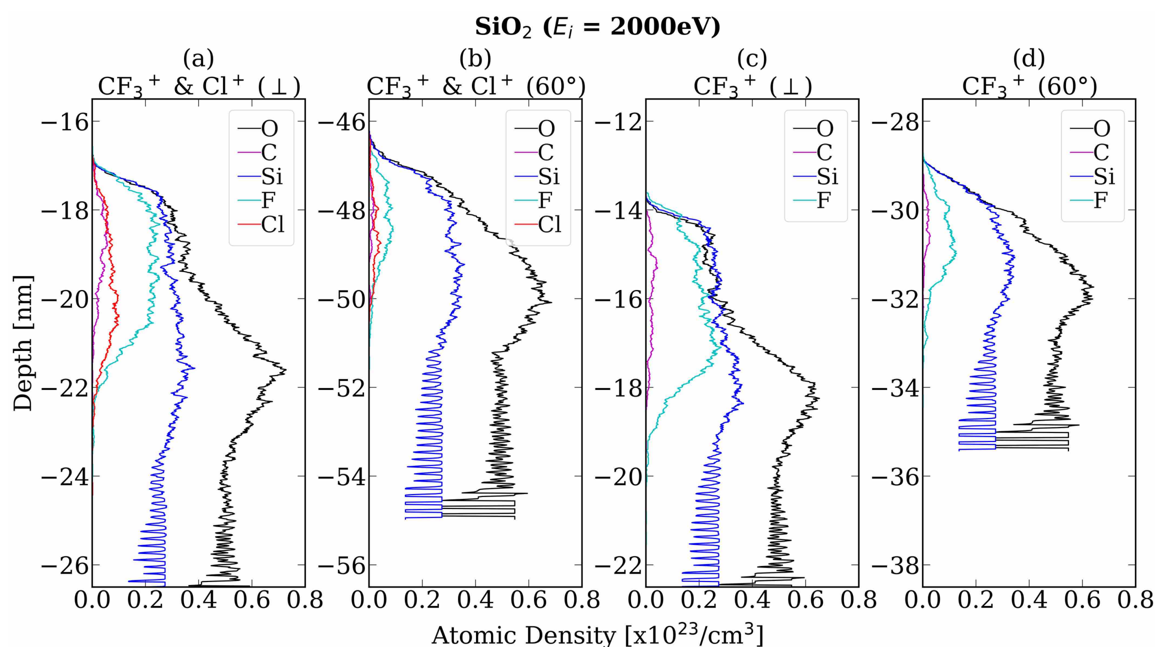

FIGURE C.8: The depth profiles of the atomic densities for SiO_2 etched by 2,000eV CF_3^+ & Cl^+ injected at (a) 0° and (b) 60°, compared to SiO_2 etched by 2,000eV CF_3^+ ions injected at (c) 0° and (d) 60°. The depth profiles were taken at the same ion dose of 1.87×10^{16} CF_3^+ ions/cm^2. The origin of the vertical axis is the position of the material's top surface prior to etching. The vertical axes have different ranges but same increment.

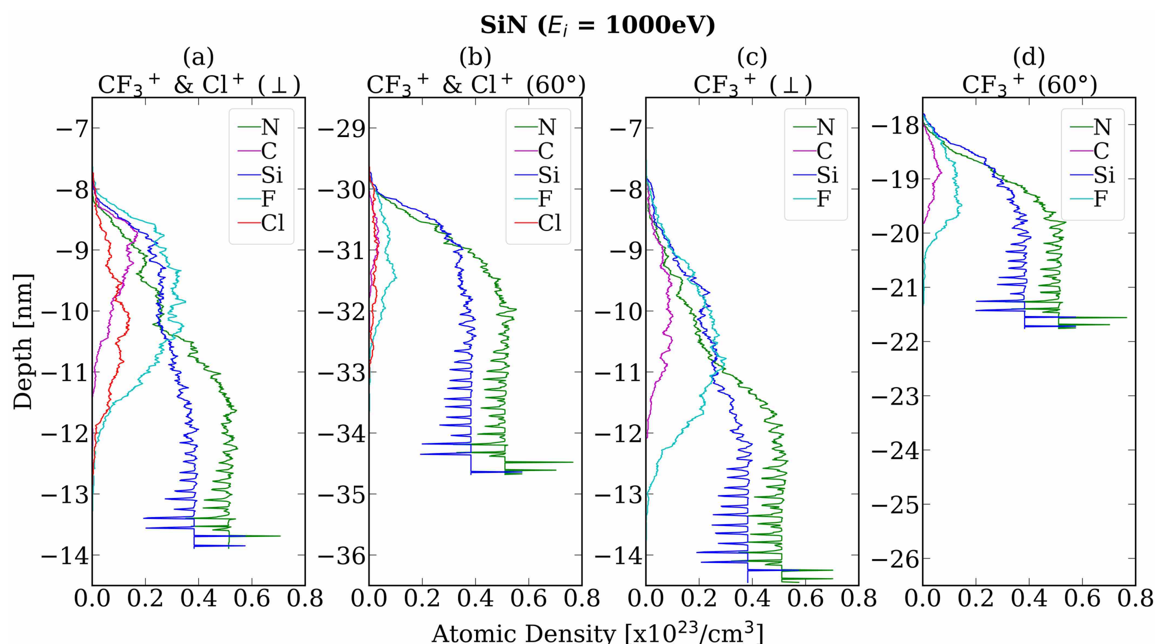

FIGURE C.9: The depth profiles of the atomic densities for SiN etched by 1,000eV CF_3^+ & Cl^+ injected at (a) 0° and (b) 60°, compared to SiN etched by 1,000eV CF_3^+ ions injected at (c) 0° and (d) 60°. The depth profiles were taken at the same ion dose of 2.98x10^{16} CF_3^+ ions/cm^2. The origin of the vertical axis is the position of the material's top surface prior to etching. The vertical axes have different ranges but same increment.

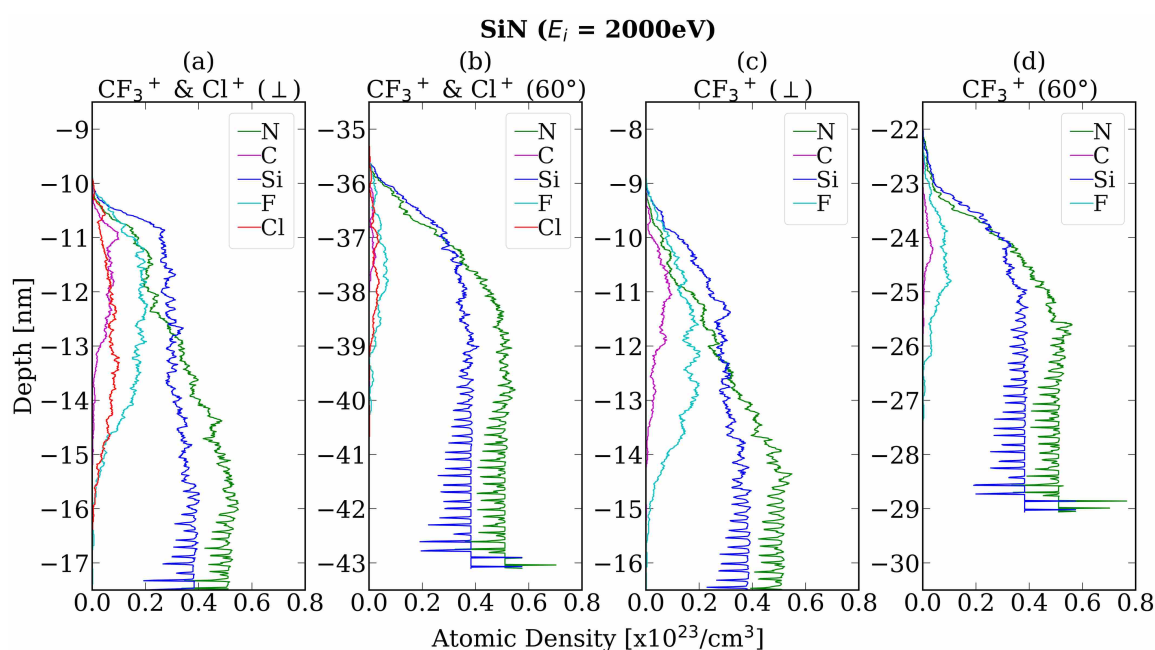

FIGURE C.10: The depth profiles of the atomic densities for SiN etched by 2,000eV CF_3^+ & Cl^+ injected at (a) 0° and (b) 60°, compared to SiN etched by 2,000eV CF_3^+ ions injected at (c) 0° and (d) 60°. The depth profiles were taken at the same ion dose of 2.23x10^{16} CF_3^+ ions/cm^2. The origin of the vertical axis is the position of the material's top surface prior to etching. The vertical axes have different ranges but same increment.

C.3 Etch Rate of SiO_2 and SiN Etched by CF_3^+ and Ar^+

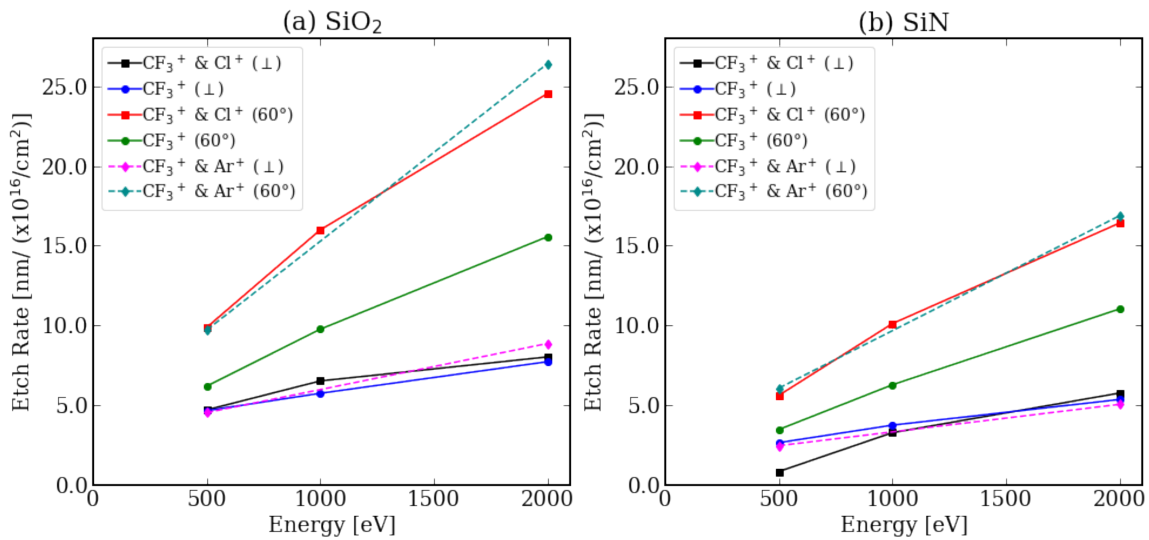

FIGURE C.11: Etch rate as a function of ion energy for (a) SiO_2 and (b) SiN etched by CF_3^+ ions with Cl^+ ions denoted by square markers, by CF_3^+ ions only denoted by circle markers, and by CF_3^+ ions with Ar^+ ions denoted by diamond markers. The ions are injected at 0° and 60° incident angles. The lines are just guides to the eyes.

C.4 Desorbed Species from the Etching of SiN by CF_3^+ and Cl^+

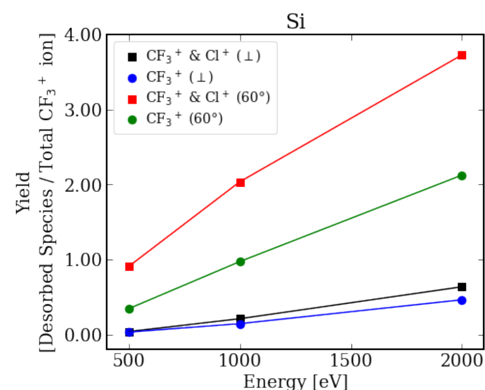

(a)

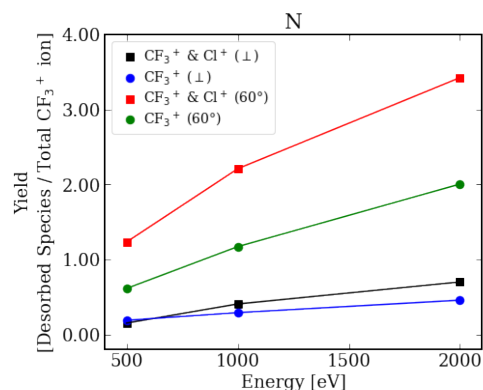

(b)

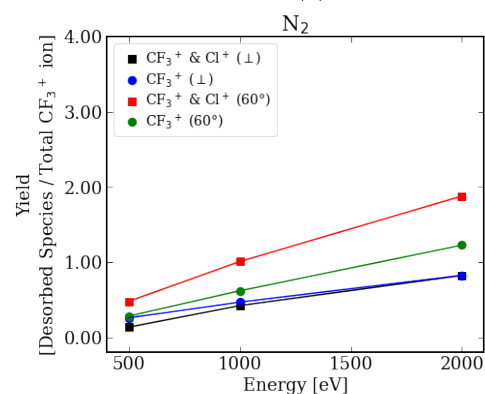

(c)

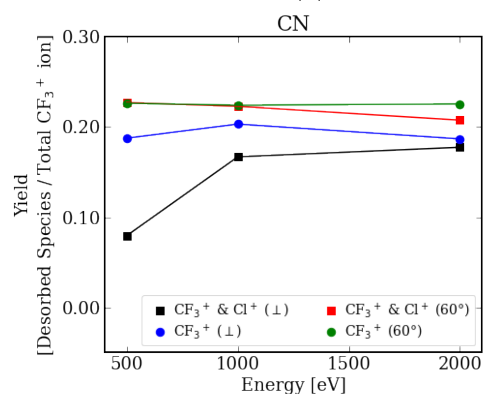

(d)

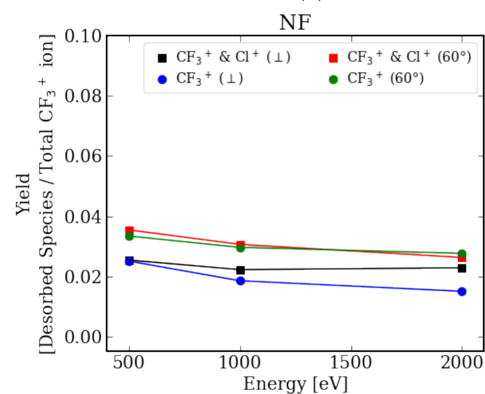

(e)

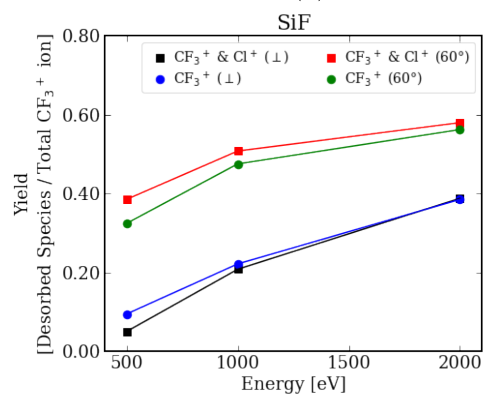

(f)

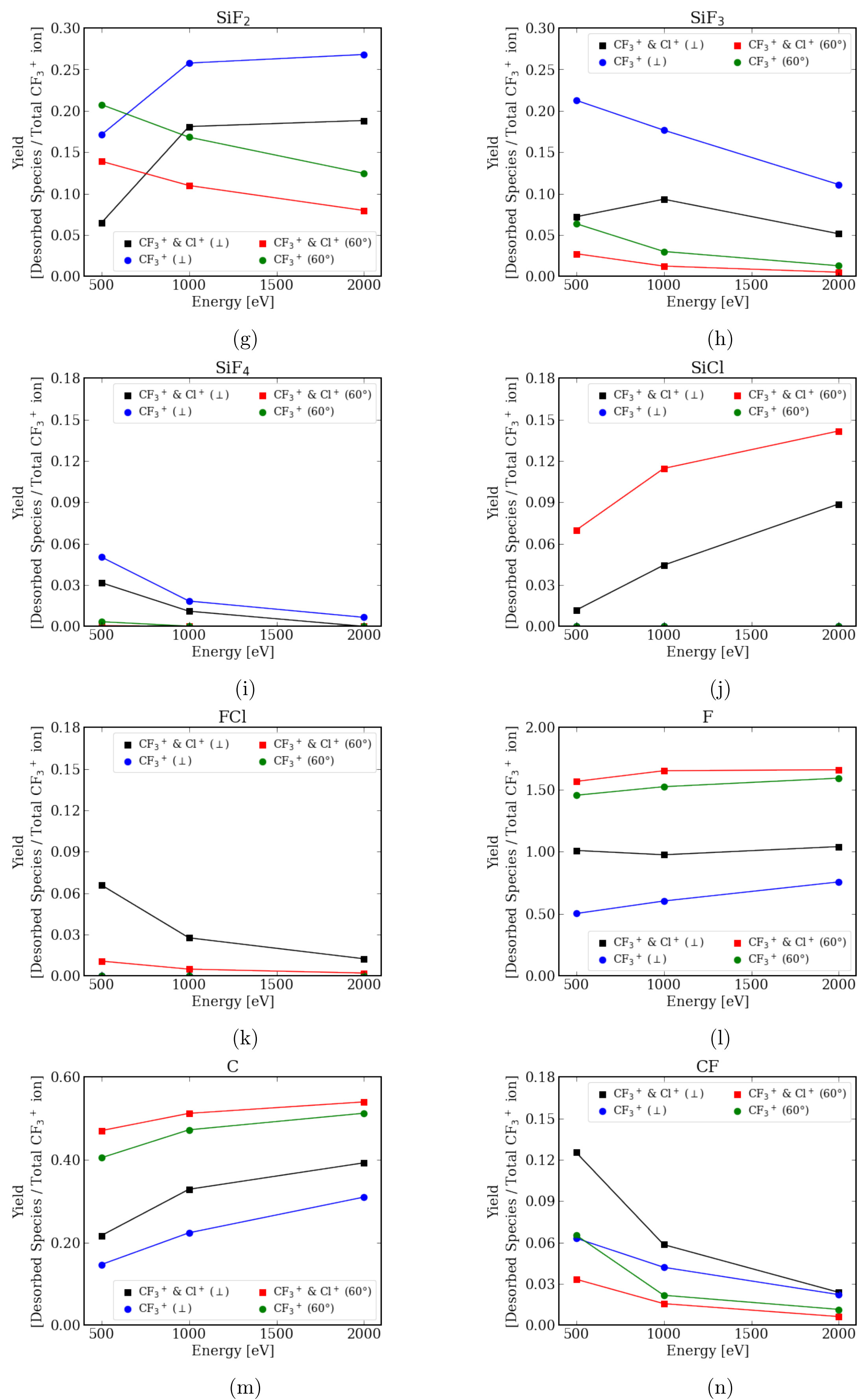

FIGURE C.12: The yield of the desorbed species as a function of ion energy for SiN etched by CF_3^+ ions with and without addition of Cl^+ ions. The yield is calculated as the number of specified desorbed species over the total number of injected CF_3^+ ions.

Appendix D

MD Study of SiO_2 Nanohole Etching by FC Plasmas – Supplementary Material

D.1 Interatomic Potential Functions

The interatomic potential functions introduced in Sec.II are discussed briefly in this supplementary document. The interatomic potential model for the Si–O–C–F system is based on SW-type [48, 49, 108] potential where the total potential energy Φ is the summation of the two-body V_2 and three-body V_3 interactions given by

$$\Phi = \sum_{i<j} V_2(i,j) + \sum_{i<j<k} V_3(i,j,k).$$

In this SW-type potential model, all atoms are considered to be charge-neutral. Based on previous studies [45, 50, 74, 110, 115], the two-body V_2 interaction between the ith and j^{th} atoms would be dependent on their interatomic distance r_{ij}, and is given by

$$V_2(i,j) = ar^{-2q}\exp\left(\frac{2d}{r_{ij}-r_c}\right) - br^{-q}\exp\left(\frac{d}{r_{ij}-r_c}\right), \text{ if } r_{ij} < r_c \tag{D.1}$$

where a, b, d, q, and r_c are parameters with r_c being the interatomic cutoff distance. The two-body V_2 interaction would be zero if $r_{ij} \geq r_c$.

The three-body V_3 interaction describes the angular dependencies of the ith, j^{th}, and k^{th} atoms given by

$$V_3(i,j,k) = h_{jik}(r_{ij}, r_{ik}, \theta_{jik}) + h_{ijk}(r_{ji}, r_{jk}, \theta_{ijk}) + h_{ikj}(r_{ki}, r_{kj}, \theta_{ikj}). \tag{D.2}$$

The h function in Eq. D.2 is dependent on the angle between three atoms θ (the vertex atom is denoted by the center subscript), and the distances r of the two atoms from the vertex atom given by

$$h_{ijk}(r_{ji}, r_{jk}, \theta_{ijk}) = k_{ijk}|\cos\theta_{ijk} - \Theta_{ijk}|^{\gamma_{ijk}} f_{ij}(r_{ij}) f_{jk}(r_{jk}). \tag{D.3}$$

where k, Θ, and γ are parameters. The f function in Eq. D.3 prevents the overestimation of the angular dependency, and is dependent on V_2 given by

$$f_{ij}(r) = \begin{cases} 1, & r \leq r_{min}, \\ \frac{V_2(r)}{V_{2min}}, & r_{min} < r < r_c, \\ 0, & r > r_c, \end{cases}$$

where r_{min} is the distance between the ith and j^{th} at the minimum two-body interaction energy V_{2min}.

The parameters for two-body V_2 and three-body V_3 potential functions are determined by Levenberg-Marquardt nonlinear fitting of the potential energy curve of various atomic

Table D.1: Parameters for two-body V_2 potential functions.

	a	b	d	q	r_c
Si–Si	170.0	38.3	0.614	1.89	3.6
Si–O	122.0	44.6	0.453	2.52	2.5
Si–C	122.0	44.9	0.176	2.86	2.8
Si–F	75.6	41.7	0.269	2.21	2.6
C–C	90.1	36.4	0.972	1.30	2.5
*C=C		41.9	0.678	1.73	
*C≡C		103.0	1.82	1.02	
C–O	35.1	23.1	0.302	2.16	2.3
*C=O		45.7	0.616	2.18	
*C≡O		51.8	0.652	2.04	
C–F	20.2	20.2	0.113	2.39	2.3
O–O	20.7	11.0	0.481	2.06	2.4
*O=O		69.6	2.34	0.209	
O–F	47.4	20.8	0.659	2.33	2.2
F–F	13.8	9.59	0.137	2.58	2.2

[1]

configurations. The potential energy curves are obtained from *ab initio* quantum mechanical calculations based on density functional theory (DFT) using the software *Gaussian* with B3LYP/6-311G basis set [52]. The DFT data for two-body V_2 are obtained by scanning the distance between two atoms. For three-body V_3, the DFT data are obtained by scanning the angle between three atoms. The parameters obtained for the two-body V_2 and three-body V_3 potential functions are summarized in Table D.1 and Table D.2 respectively.

Table D.2: Parameters for three-body V_3 potential functions.

j–i–k	k	Θ	γ
Si–Si–Si	2.14	-0.333	2.00
Si–Si–O	1.72	-0.333	2.00
Si–Si–C	2.60	-0.333	2.00
Si–Si–F	2.08	-0.333	2.00
O–Si–O	3.07	-0.333	2.00
O–Si–C	2.81	-0.333	2.00
O–Si–F	2.26	-0.333	2.00
C–Si–C	3.42	-0.333	2.00
C–Si–F	2.62	-0.333	2.00
F–Si–F	2.75	-0.333	2.00
O–O–O	5.00	0.000	0.00
O–O–Si	5.00	0.000	0.00

Continuation of Table ??

j–i–k		k	Θ	γ
O–O–C		2.21	-0.494	2.00
O–O–F		3.53	-0.214	2.00
Si–O–Si		1.31	-0.721	2.00
Si–O–C		2.86	-0.524	2.00
Si–O–F		2.98	-0.400	2.00
C–O–C		4.78	-0.413	2.00
C–O–F		2.08	-0.468	2.00
F–O–F		6.22	-0.273	2.00
C–C–C		4.76	-0.333	2.00
C–C–Si		2.96	-0.333	2.00
C–C–O		3.66	-0.333	2.00
C–C–F		4.28	-0.333	2.00
Si–C–Si		2.17	-0.332	2.00
Si–C–O		2.72	-0.333	2.00
Si–C–F		3.09	-0.330	2.00
O–C–O		3.67	-0.333	2.00
O–C–F		4.54	-0.333	2.00
F–C–F		6.39	-0.333	2.00
C–C=C		4.62	-0.469	2.00
Si–C=C		3.57	-0.976	2.00
O–C=C	(O=C–C)	4.59	-0.447	2.00
F–C=C		5.40	-0.461	2.00
O–C=O		5.68	-0.460	2.00
F–C=O		7.48	-0.575	2.00
C=C=C	(C–C≡C)	2.56	-1.000	1.73
O=C=C	(O–C≡C)	2.44	-1.000	1.33
Si-C≡C		1.67	-1.000	1.13
F-C≡C		2.74	-1.000	1.20
O=C=O		6.62	-1.000	1.20

The Van der Waals (vdW) interactions among the atoms are also considered in the simulations and is given by

$$V_{vdW}(r) = 4\epsilon\left\{ \left(\frac{\sigma}{r}\right)^{12} - \left(\frac{\sigma}{r}\right)^{6} \right\} \exp\left(\frac{d_1}{r-c_1} - \frac{d_2}{r-c_2}\right) \text{ if } c_2 < r < c_1, \quad \text{otherwise } V_{vdW}(r) = 0, \tag{D.4}$$

where $\epsilon = 0.0108$ eV, $\sigma = 3.5$ Å, $d_1 = d_2 = 0.1$ Å, $c_1 = 8.0$ Åand $c_2 = 3.5$ Å. The repulsive interaction of the Van der Waals is not included since the repulsive interaction of the atoms is already accounted by the two-body V_2 potential that describes covalent

bonding. Also, the minimum bond energy in Van der Waals interactions is extremely small ($\simeq 10^{-2}$ eV) in comparison to typical covalent bonds (several eV) [53]

D.2 Deposition of CF_3 Radicals

The deposition simulation of FC layers on SiO_2 films by CF_3 radicals is briefly discussed here. As discussed in Sec.II of the main manuscript, the average kinetic energy of radicals at 300K should be 0.026eV. However, to reduce the traveling time of the CF_3 radicals to reach the surface, we used 0.5eV in our simulations. We also stated there that the nature of radical deposition on the surface was not affected. To support this, we have irradiated a 4.19nm $\times$ 4.19nm SiO_2 film surface with CF_3 radicals with energies of 0.026eV and 0.5eV. The injection cycle is essentially the same as the one discussed in Sec. II but with a shortened cooling time of 300fs. As such, the total injection cycle is 1,000 fs. Since the energy of the impact particles is quite low, we have shortened the cooling time to achieve faster simulations.

The simulation results, i.e., snapshots of SiO_2 films with FC layers deposited by 0.026eV and 0.5eV CF_3 radicals are shown in Fig. D.1. After 1,000 injections (5.7×10^{15} cm^{-2} dose), similar ≈2nm-thick FC layers with an F/C ratio of 3.0 were obtained for both cases.

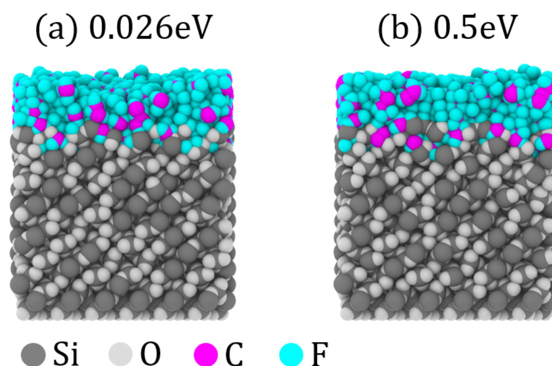

FIGURE D.1: Snapshots of SiO_2 film injected with (a) 0.026eV and (b) 0.5eV CF_3 radicals (1,000 injections).

Bibliography

[1] F. Masuoka, M. Asano, H. Iwahashi, T. Komuro, and S. Tanaka, "A new flash e^{2}prom cell using triple polysilicon technology," in *1984 International Electron Devices Meeting*, pp. 464–467, 1984.

[2] R. Micheloni, L. Crippa, and A. Marelli, *Inside NAND flash memories*. Springer, 2010.

[3] Toshiba America Electronic Components Inc., "Nand vs. nor flash memory technology overview."

[4] F. Masuoka, M. Momodomi, Y. Iwata, and R. Shirota, "New ultra high density eprom and flash eeprom with nand structure cell," in *1987 International Electron Devices Meeting*, pp. 552–555, 1987.

[5] A. S. Spinelli, C. M. Compagnoni, and A. L. Lacaita, "Reliability of nand flash memories: Planar cells and emerging issues in 3d devices," *Computers*, vol. 6, no. 2, 2017.

[6] R. Micheloni, L. Crippa, C. Zambelli, and P. Olivo, "Architectural and Integration Options for 3D NAND Flash Memories," *Computers*, vol. 6, no. 27, 2017.

[7] M. Helm, J.-K. Park, A. Ghalam, J. Guo, C. wan Ha, C. Hu, H. Kim, K. Kavalipurapu, E. Lee, A. Mohammadzadeh, D. Nguyen, V. Patel, T. Pekny, B. Saiki, D. Song, J. Tsai, V. Viajedor, L. Vu, T. Wong, J. H. Yun, R. Ghodsi, A. D'Alessandro, D. Di Cicco, and V. Moschiano, "19.1 a 128gb mlc nand-flash

device using 16nm planar cell," in *2014 IEEE International Solid-State Circuits Conference Digest of Technical Papers (ISSCC)*, pp. 326–327, 2014.

[8] S. Choi, D. Kim, S. Choi, B. Kim, S. Jung, K. Chun, N. Kim, W. Lee, T. Shin, H. Jin, H. Cho, S. Ahn, Y. Hong, I. Yang, B. Kim, P. Yoo, Y. Jung, J. Lee, J. Shin, T. Kim, K. Park, and J. Kim, "19.2 a 93.4mm^2 64gb mlc nand-flash memory with 16nm cmos technology," in *2014 IEEE International Solid-State Circuits Conference Digest of Technical Papers (ISSCC)*, pp. 328–329, 2014.

[9] S. Lee, J.-y. Lee, I.-h. Park, J. Park, S.-w. Yun, M.-s. Kim, J.-h. Lee, M. Kim, K. Lee, T. Kim, B. Cho, D. Cho, S. Yun, J.-n. Im, H. Yim, K.-h. Kang, S. Jeon, S. Jo, Y.-l. Ahn, S.-M. Joe, S. Kim, D.-k. Woo, J. Park, H.-w. Park, Y. Kim, J. Park, Y. Choi, M. Hirano, J.-D. Ihm, B. Jeong, S.-K. Lee, M. Kim, H. Lee, S. Seo, H. Jeon, C.-h. Kim, H. Kim, J. Kim, Y. Yim, H. Kim, D.-S. Byeon, H.-J. Yang, K.-T. Park, K.-h. Kyung, and J.-H. Choi, "7.5 a 128gb 2b/cell nand flash memory in 14nm technology with tprog=640µs and 800mb/s i/o rate," in *2016 IEEE International Solid-State Circuits Conference (ISSCC)*, pp. 138–139, 2016.

[10] Entegris, "White paper: Considerations for improving 3d nand performance, reliability, and yield."

[11] A. Silvagni, "3d nand flash based on planar cells," *Computers*, vol. 6, no. 4, 2017.

[12] T. Endoh, K. Kinoshita, T. Tanigami, Y. Wada, K. Sato, K. Yamada, T. Yokoyama, N. Takeuchi, K. Tanaka, N. Awaya, K. Sakiyama, and F. Masuoka, "Novel ultra high density flash memory with a stacked-surrounding gate transistor (s-sgt) structured cell," in *International Electron Devices Meeting. Technical Digest (Cat. No.01CH37224)*, pp. 2.3.1–2.3.4, 2001.

[13] H. Tanaka, M. Kido, K. Yahashi, M. Oomura, R. Katsumata, M. Kito, Y. Fukuzumi, M. Sato, Y. Nagata, Y. Matsuoka, Y. Iwata, H. Aochi, and A. Nitayama, "Bit cost scalable technology with punch and plug process for ultra high density flash memory," in *2007 IEEE Symposium on VLSI Technology*, pp. 14–15, 2007.

[14] A. Goda, "3-D NAND Technology Achievements and Future Scaling Perspectives," *IEEE Trans. Electron Devices*, vol. 67, no. 4, pp. 1373–1381, 2020.

[15] K. Kim and S. Lee, "Memory technology in the future," *Microelectron. Eng.*, vol. 84, no. 9, pp. 1976–1981, 2007. INFOS 2007.

[16] K. Parat and A. Goda, "Scaling trends in nand flash," in *2018 IEEE International Electron Devices Meeting (IEDM)*, pp. 2.1.1–2.1.4, 2018.

[17] A. Nitayama and H. Aochi, "Vertical 3D NAND Flash Memory Technology," *ECS Trans.*, vol. 41, no. 7, pp. 15–25, 2011.

[18] Y. Fukuzumi, R. Katsumata, M. Kito, M. Kido, M. Sato, H. Tanaka, Y. Nagata, Y. Matsuoka, Y. Iwata, H. Aochi, and A. Nitayama, "Optimal integration and characteristics of vertical array devices for ultra-high density, bit-cost scalable flash memory," in *2007 IEEE International Electron Devices Meeting*, pp. 449–452, 2007.

[19] J.-W. Im, W.-P. Jeong, D.-H. Kim, S.-W. Nam, D.-K. Shim, M.-H. Choi, H.-J. Yoon, D.-H. Kim, Y.-S. Kim, H.-W. Park, D.-H. Kwak, S.-W. Park, S.-M. Yoon, W.-G. Hahn, J.-H. Ryu, S.-W. Shim, K.-T. Kang, S.-H. Choi, J.-D. Ihm, Y.-S. Min, I.-M. Kim, D.-S. Lee, J.-H. Cho, O.-S. Kwon, J.-S. Lee, M.-S. Kim, S.-H. Joo, J.-H. Jang, S.-W. Hwang, D.-S. Byeon, H.-J. Yang, K.-T. Park, K.-H. Kyung, and J.-H. Choi, "7.2 a 128gb 3b/cell v-nand flash memory with 1gb/s i/o rate," in *2015 IEEE International Solid-State Circuits Conference - (ISSCC) Digest of Technical Papers*, pp. 1–3, 2015.

[20] K. Nojiri, *Dry Etching Technology for Semiconductors.* Springer, 2015.

[21] G. S. May and C. J. Spanos, *Fundamentals of Semiconductor Manufacturing and Process Control.* IEEE, 2006.

[22] MEMS and Nanotechnology Exchange, "Etching processes."

[23] F. Chen, *Introduction to Plasma Physics and Controlled Fusion*. Springer, third ed., 2018.

[24] B. Wu, A. Kumar, and S. Pamarthy, “High aspect ratio silicon etch: A review,” *J. Appl. Phys.*, vol. 108, no. 5, p. 51101, 2010.

[25] C. Cardinaud, M.-C. Peignon, and P.-Y. Tessier, “Plasma etching: principles, mechanisms, application to micro- and nano-technologies,” *Appl. Surf. Sci.*, vol. 164, no. 1, pp. 72–83, 2000. Surface Science in Micro & Nanotechnology.

[26] Y.-Y. Tu, T. J. Chuang, and H. F. Winters, “Chemical sputtering of fluorinated silicon,” *Phys. Rev. B*, vol. 23, pp. 823–835, Jan 1981.

[27] M. A. Lieberman and A. J. Lichtenberg, *Principles of Plasma Discharges and Materials Processing*. John Wiley & Sons, 2nd ed., 2005.

[28] I. Adamovich, S. D. Baalrud, A. Bogaerts, P. J. Bruggeman, M. Cappelli, V. Colombo, U. Czarnetzki, U. Ebert, J. G. Eden, P. Favia, D. B. Graves, S. Hamaguchi, G. Hieftje, M. Hori, I. D. Kaganovich, U. Kortshagen, M. J. Kushner, N. J. Mason, S. Mazouffre, S. M. Thagard, H.-R. Metelmann, A. Mizuno, E. Moreau, A. B. Murphy, B. A. Niemira, G. S. Oehrlein, Z. L. Petrovic, L. C. Pitchford, Y.-K. Pu, S. Rauf, O. Sakai, S. Samukawa, S. Starikovskaia, J. Tennyson, K. Terashima, M. M. Turner, M. C. M. van de Sanden, and A. Vardelle, “The 2017 Plasma Roadmap: Low Temperature Plasma Science and Technology,” *J. Phys. D: Appl. Phys.*, vol. 50, p. 323001, 7 2017.

[29] H. F. Winters, J. W. Coburn, and E. Kay, “Plasma etching a "pseudo-black-box" approach,” *J. Appl. Phys.*, vol. 48, no. 12, pp. 4973–4983, 1977.

[30] J. W. Coburn, H. F. Winters, and T. J. Chuang, “Ion-surface interactions in plasma etching,” *J. Appl. Phys.*, vol. 48, no. 8, pp. 3532–3540, 1977.

[31] H. F. Winters, “The role of chemisorption in plasma etching,” *J. Appl. Phys.*, vol. 49, no. 10, pp. 5165–5170, 1978.

[32] J. W. Coburn and H. F. Winters, "Plasma etching—a discussion of mechanisms," *J. Vac. Sci. Technol.*, vol. 16, no. 2, pp. 391–403, 1979.

[33] M. J. Kushner, "A kinetic study of the plasma-etching process. i. a model for the etching of si and sio_2 in c_nf_m/h_2 and c_nf_m/o_2 plasmas," *J. Appl. Phys.*, vol. 53, no. 4, pp. 2923–2938, 1982.

[34] R. A. Heinecke, "Control of relative etch rates of sio_2 and si in plasma etching," *Solid State Electron.*, vol. 18, no. 12, pp. 1146–1147, 1975.

[35] M. Izawa, N. Negishi, K. Yokogawa, and Y. Momonoi, "Investigation of bowing reduction in SiO_2 etching taking into account radical sticking in a hole," *Jpn. J. Appl. Phys.*, vol. 46, pp. 7870–7874, Dec 2007.

[36] M. Miyake, N. Negishi, M. Izawa, K. Yokogawa, M. Oyama, and T. Kanekiyo, "Effects of mask and necking deformation on bowing and twisting in high-aspect-ratio contact hole etching," *Jpn. J. Appl. Phys.*, vol. 48, p. 08HE01, aug 2009.

[37] J. K. Kim, S. H. Lee, S. I. Cho, and G. Y. Yeom, "Study on contact distortion during high aspect ratio contact sio2 etching," *J. Vac. Sci. Technol. A*, vol. 33, no. 2, p. 021303, 2015.

[38] K. Karahashi and S. Hamaguchi, "Ion beam experiments for the study of plasma–surface interactions," *J. Phys. D: Appl. Phys.*, vol. 47, no. 22, p. 224008, 2014.

[39] D. Frenkel and B. Smit, *Understanding molecular simulation: From algorithms to applications.* Academic Press, 2002.

[40] B. J. Alder and T. E. Wainwright, "Studies in molecular dynamics. i. general method," *J. Chem. Phys.*, vol. 31, no. 2, pp. 459–466, 1959.

[41] N. Brambilla, G. a. Krein, J. Tarrús Castellà, and A. Vairo, "Born-Oppenheimer approximation in an effective field theory language," *Phys. Rev. D*, vol. 97, no. 1, p. 016016, 2018.

[42] I. M. Torrens, *Interatomic Potentials.* Academic Press, 1972.

[43] M. P. Allen and D. J. Tildesley, *Computer simulation of liquids.* Oxford University Press, 2017.

[44] S. Hug, *Chapter 6 Classical Molecular Dynamics in a Nutshell*, p. 127–152. Humana Press, 2013.

[45] H. Ohta and S. Hamaguchi, "Classical interatomic potentials for Si–O–F and Si–O–Cl systems," *J. Chem. Phys.*, vol. 115, pp. 6679–6690, 9 2001.

[46] R. LeSar, *Introduction to Computational Materials Science: Fundamentals to Applications.* Cambridge University Press, 2016.

[47] C. M. Cagomoc, *Molecular Dynamics Simulation of Deep-Hole Etching for Flash Memory Applications.* MS dissertation, Osaka University, 2019.

[48] F. H. Stillinger and T. A. Weber, "Computer simulation of local order in condensed phases of silicon," *Phys. Rev. B*, vol. 31, pp. 5262–5271, 4 1985.

[49] F. H. Stillinger and T. A. Weber, "Molecular dynamics simulation for chemically reactive substances. Fluorine," *J. Chem. Phys.*, vol. 88, pp. 5123–5133, 4 1988.

[50] H. Ohta, *Molecular dynamics simulation of the plasma-surface interaction during plasma etching processes.* PhD dissertation, Kyoto University, 2004.

[51] E. J. C. Tinacba, *Molecular dynamics simulation study of Si-based materials etching processes.* PhD dissertation, Osaka University, 2021.

[52] M. J. Frisch, G. W. Trucks, H. B. Schlegel, G. E. Scuseria, M. A. Robb, J. R. Cheeseman, G. Scalmani, V. Barone, B. Mennucci, G. A. Petersson, H. Nakatsuji, M. Caricato, X. Li, H. P. Hratchian, A. F. Izmaylov, J. Bloino, G. Zheng, J. L. Sonnenberg, M. Hada, M. Ehara, K. Toyota, R. Fukuda, J. Hasegawa, M. Ishida, T. Nakajima, Y. Honda, O. Kitao, H. Nakai, T. Vreven, J. A. Montgomery, J. E. Peralta, F. Ogliaro, M. Bearpark, J. J. Heyd, E. Brothers, K. N. Kudin, V. N.

Staroverov, R. Kobayashi, J. Normand, K. Raghavachari, A. Rendell, J. C. Burant, S. S. Iyengar, J. Tomasi, M. Cossi, N. Rega, J. M. Millam, M. Klene, J. E. Knox, J. B. Cross, V. Bakken, C. Adamo, J. Jaramillo, R. Gomperts, R. E. Stratmann, O. Yazyev, A. J. Austin, R. Cammi, C. Pomelli, J. W. Ochterski, R. L. Martin, K. Morokuma, V. G. Zakrzewski, G. A. Voth, P. Salvador, J. J. Dannenberg, S. Dapprich, A. D. Daniels, Farkas, J. B. Foresman, J. V. Ortiz, J. Cioslowski, and D. J. Fox, "Gaussian 09," 2009. Gaussian Inc. Wallingford CT.

[53] S. Hamaguchi and H. Ohta, "Effects of Van der Waals Interactions on SiO_2 Etching by CF_x Plasmas," *J. Plasma Fusion Res. SERIES*, vol. 6, pp. 399–401, 2004.

[54] L. Verlet, "Computer "experiments" on classical fluids. i. thermodynamical properties of lennard-jones molecules," *Phys. Rev.*, vol. 159, pp. 98–103, Jul 1967.

[55] S. Nosé, "A molecular dynamics method for simulations in the canonical ensemble," *Mol. Phys.*, vol. 52, no. 2, pp. 255–268, 1984.

[56] W. G. Hoover, "Canonical dynamics: Equilibrium phase-space distributions," *Phys. Rev. A*, vol. 31, pp. 1695–1697, Mar 1985.

[57] T. Schneider and E. Stoll, "Molecular-dynamics study of a three-dimensional one-component model for distortive phase transitions," *Phys. Rev. B*, vol. 17, pp. 1302–1322, 2 1978.

[58] H. J. Berendsen, J. P. Postma, W. F. Van Gunsteren, A. Dinola, and J. R. Haak, "Molecular dynamics with coupling to an external bath," *J. Chem. Phys.*, vol. 81, no. 8, pp. 3684–3690, 1984.

[59] S. C. Harvey, R. K.-Z. Tan, and T. E. Cheatham III, "The Flying Ice Cube: Velocity Rescaling in Molecular Dynamics Leads to Violation of Energy Equipartition," *J. Comput. Chem.*, vol. 19, no. 7, 1998.

[60] K. Miyake, T. Ito, M. Isobe, K. Karahashi, M. Fukasawa, K. Nagahata, T. Tatsumi, and S. Hamaguchi, "Characterization of polymer layer formation during SiO_2/SiN

etching by fluoro/hydrofluorocarbon plasmas," *Jpn. J. Appl. Phys.*, vol. 53, no. 3S2, p. 03DD02, 2014.

[61] K. Mizotani, M. Isobe, and S. Hamaguchi, "Molecular dynamic simulation of damage formation at Si vertical walls by grazing incidence of energetic ions in gate etching processes," *J. Vac. Sci. Technol. A*, vol. 33, no. 2, p. 21313, 2015.

[62] S. Numazawa, K. Machida, M. Isobe, and S. Hamaguchi, "Molecular dynamics study on fluorine radical multilayer adsorption mechanism during Si, SiO_2, and Si_3N_4 etching processes," *Jpn. J. Appl. Phys.*, vol. 55, p. 116204, 10 2016.

[63] E. J. Capdos Tinacba, M. Isobe, K. Karahashi, and S. Hamaguchi, "Molecular dynamics simulation of Si and SiO_2 reactive ion etching by fluorine-rich ion species," *Surf. Coat. Technol.*, vol. 380, p. 125032, 12 2019.

[64] H. Yamada and S. Hamaguchi, "Molecular-dynamics simulations of organic polymer etching by hydrocarbon beams," *J. Appl. Phys.*, vol. 96, pp. 6147–6152, 11 2004.

[65] H. Yamada and S. Hamaguchi, "Numerical analyses of surface interactions between radical beams and organic polymer surfaces," *Plasma Phys. Control. Fusion*, vol. 47, p. A11–A18, 4 2005.

[66] T. Kawase and S. Hamaguchi, "Molecular dynamics simulation analyses on injection angle dependence of SiO_2 sputtering yields by fluorocarbon beams," *Thin Solid Films*, vol. 515, no. 12, pp. 4883–4886, 2007.

[67] M. Yamashiro, H. Yamada, and S. Hamaguchi, "Molecular dynamics simulation study on substrate temperature dependence of sputtering yields for an organic polymer under ion bombardment," *J. Appl. Phys.*, vol. 101, no. 4, p. 46108, 2007.

[68] M. Taguchi and S. Hamaguchi, "MD simulations of amorphous SiO_2 thin film formation in reactive sputtering deposition processes," *Thin Solid Films*, vol. 515, no. 12, pp. 4879–4882, 2007.

[69] M. Yamashiro, H. Yamada, and S. Hamaguchi, "Molecular Dynamics Simulations of Organic Polymer Dry Etching at High Substrate Temperatures," *Jpn. J. Appl. Phys.*, vol. 46, pp. 1692–1699, 4 2007.

[70] M. Yamashiro, H. Yamada, and S. Hamaguchi, "Molecular dynamics simulations for nitridation of organic polymer surfaces due to hydrogen–nitrogen ion beam injections," *Thin Solid Films*, vol. 516, no. 11, pp. 3449–3453, 2008.

[71] Y. Murakami, S. Horiguchi, and S. Hamaguchi, "Molecular dynamics simulation of the formation of sp^3 hybridized bonds in hydrogenated diamondlike carbon deposition processes," *Phys. Rev. E*, vol. 81, p. 41602, 4 2010.

[72] E. J. C. Tinacba, M. Isobe, and S. Hamaguchi, "Surface damage formation during atomic layer etching of silicon with chlorine adsorption," *J. Vac. Sci. Technol. A*, vol. 39, p. 042603, 6 2021.

[73] D. W. Hess, "Plasma–material interactions," *J. Vac. Sci. Technol. A.*, vol. 8, no. 3, pp. 1677–1684, 1990.

[74] H. Ohta and S. Hamaguchi, "Molecular dynamics simulation of silicon and silicon dioxide etching by energetic halogen beams," *J. Vac. Sci. Technol. A*, vol. 19, pp. 2373–2381, 9 2001.

[75] G. H. Lee, S. Hwang, J. Yu, and H. Kim, "Architecture and process integration overview of 3d nand flash technologies," *Appl. Sci.*, vol. 11, no. 15, 2021.

[76] B. N. Chapman, *Glow Discharge Processes: Sputtering and Plasma Etching.* Wiley, 1980.

[77] S. Hamaguchi, "Modeling and simulation methods for plasma processing," *IBM J. Res. Dev.*, vol. 43, no. 1.2, pp. 199–215, 1999.

[78] T. Makabe and Z. L. Petrović, *Plasma Electronics: Applications in Microelectronic Device Fabrication.* CRC Press, 2nd ed., 2016.

[79] I. Adamovich, S. Agarwal, E. Ahedo, L. L. Alves, S. Baalrud, N. Babaeva, A. Bogaerts, A. Bourdon, P. J. Bruggeman, C. Canal, E. H. Choi, S. Coulombe, Z. Donkó, D. B. Graves, S. Hamaguchi, D. Hegemann, M. Hori, H.-H. Kim, G. M. W. Kroesen, M. J. Kushner, A. Laricchiuta, X. Li, T. E. Magin, S. M. Thagard, V. Miller, A. B. Murphy, G. S. Oehrlein, N. Puac, R. M. Sankaran, S. Samukawa, M. Shiratani, M. Šimek, N. Tarasenko, K. Terashima, E. T. Jr, J. Trieschmann, S. Tsikata, M. M. Turner, I. J. van der Walt, M. C. M. van de Sanden, and T. von Woedtke, "The 2022 Plasma Roadmap: low temperature plasma science and technology," *J. Phys. D: Appl. Phys.*, vol. 55, p. 373001, 7 2022.

[80] G. S. Oehrlein and S. Hamaguchi, "Foundations of low-temperature plasma enhanced materials synthesis and etching," *Plasma Sources Sci. Technol.*, vol. 27, no. 2, p. 023001, 2018.

[81] T. Iwase, K. Yokogawa, and M. Mori, "Eliminating dependence of hole depth on aspect ratio by forming ammonium bromide during plasma etching of deep holes in silicon nitride and silicon dioxide," *Jpn. J. Appl. Phys.*, vol. 57, p. 06JC03, may 2018.

[82] T. Iwase, Y. Kamaji, S. Y. Kang, K. Koga, N. Kuboi, M. Nakamura, N. Negishi, T. Nozaki, S. Nunomura, D. Ogawa, M. Omura, T. Shimizu, K. Shinoda, Y. Sonoda, H. Suzuki, K. Takahashi, T. Tsutsumi, K. Yoshikawa, T. Ishijima, and K. Ishikawa, "Progress and perspectives in dry processes for nanoscale feature fabrication: fine pattern transfer and high-aspect-ratio feature formation," *Jpn. J. Appl. Phys.*, vol. 58, p. SE0802, may 2019.

[83] M. Omura, J. Hashimoto, T. Adachi, Y. Kondo, M. Ishikawa, J. Abe, I. Sakai, H. Hayashi, M. Sekine, and M. Hori, "Formation mechanism of sidewall striation in high-aspect-ratio hole etching," *Jpn. J. Appl. Phys.*, vol. 58, p. SEEB02, may 2019.

[84] K. Arts, S. Hamaguchi, T. Ito, K. Karahashi, H. Knoops, A. Mackus, and W. M. Kessels, "Foundations of atomic-level plasma processing in nanoelectronics," *Plasma Sources Sci. Technol.*, 2022.

[85] T. Ito, K. Karahashi, K. Mizotani, M. Isobe, S.-Y. Kang, M. Honda, and S. Hamaguchi, "Si damage due to oblique-angle ion impact relevant for vertical gate etching processes," *Jpn. J. Appl. Phys.*, vol. 51, p. 08HB01, aug 2012.

[86] Y. Du, F. Kruger, S. K. Nam, H. Lee, S. Yoo, J. Eapen, M. J. Kushner, and S. Shannon, "Comparison of glancing-angle scatterings on different materials in a high aspect ratio plasma etching process using molecular dynamics simulation," *J. Vac. Sci. Technol. A.*, vol. 40, no. 5, p. 053007, 2022.

[87] S. V. Nguyen, D. Dobuzinsky, S. R. Stiffler, and G. Chrisman, "Substrate trenching mechanism during plasma and magnetically enhanced polysilicon etching," *J. Electrochem. Soc.*, vol. 138, pp. 1112–1117, apr 1991.

[88] T. J. Dalton, J. C. Arnold, H. H. Sawin, S. Swan, and D. Corliss, "Microtrench formation in polysilicon plasma etching over thin gate oxide," *J. Electrochem. Soc.*, vol. 140, pp. 2395–2401, aug 1993.

[89] C. F. Abrams and D. B. Graves, "Energetic ion bombardment of sio2 surfaces: Molecular dynamics simulations," *J. Vac. Sci. Technol. A.*, vol. 16, no. 5, pp. 3006–3019, 1998.

[90] C. M. D. Cagomoc, M. Isobe, and S. Hamaguchi *J. Vac. Sci. Technol. A, to appear*, 2023.

[91] M. J. Romney and J. B. Anderson, "Scattering of 0.05–5-ev argon from the (111) plane of silver," *J. Chem. Phys.*, vol. 51, no. 6, pp. 2490–2496, 1969.

[92] W. J. Hays, W. E. Rodgers, and E. L. Knuth, "Scattering of argon beams with incident energies up to 20 ev from a (111) silver surface," *J. Chem. Phys.*, vol. 56, no. 4, pp. 1652–1657, 1972.

[93] R. Pfandzelter, T. Hecht, and H. Winter, "Angular distributions of fast noble gas atoms and ions after grazing scattering from a cu(111) surface," *Nucl. Instrum. Methods Phys. Res. B*, vol. 182, no. 1, pp. 213–217, 2001.

[94] J. M. Haile, *Molecular Dynamics Simulation: Elementary Methods.* John Wiley & Sons, Inc., 1997.

[95] D. B. Graves and P. Brault, "Molecular dynamics for low temperature plasma surface interaction studies," *J. Phys. D: Appl. Phys.*, vol. 42, p. 194011, 9 2009.

[96] S. Hamaguchi, M. Dalvie, R. T. Farouki, and S. Sethuraman, "A shock-tracking algorithm for surface evolution under reactive ion etching," *J. Appl. Phys*, vol. 74, no. 8, pp. 5172–5184, 1993.

[97] S. Hamaguchi and M. Dalvie, "Microprofile simulations for plasma etching with surface passivation," *J. Vac. Sci. Technol. A*, vol. 12, no. 5, pp. 2745–2753, 1994.

[98] S. Hamaguchi and M. Dalvie, "Intrinsic and passivation-induced trench tapering during plasma etching," *J. Electrochem. Soc.*, vol. 141, no. 7, pp. 1964–1972, 1994.

[99] A. A. Mayo, S. Hamaguchi, J. H. Joo, and S. M. Rossnagel, "Across-wafer nonuniformity of long throw sputter deposition," *J. Vac. Sci. Technol. B*, vol. 15, no. 5, pp. 1788–1793, 1997.

[100] R. J. Hoekstra, M. J. Grapperhaus, and M. J. Kushner, "Integrated plasma equipment model for polysilicon etch profiles in an inductively coupled plasma reactor with subwafer and superwafer topography," *J. Vac. Sci. Technol. A*, vol. 15, no. 4, pp. 1913–1921, 1997.

[101] J. Hoang, C.-C. Hsu, and J. P. Chang, "Feature profile evolution during shallow trench isolation etch in chlorine-based plasmas. i. feature scale modeling," *J. Vac. Sci. Technol. B*, vol. 26, no. 6, pp. 1911–1918, 2008.

[102] B. Radjenović and M. Radmilović-Radjenović, "Top down nano technologies in surface modification of materials," *Cent. Eur. J. Phys.*, vol. 9, no. 2, pp. 265–275, 2011.

[103] Y. Zhang, C. Huard, S. Sriraman, J. Belen, A. Paterson, and M. J. Kushner, "Investigation of feature orientation and consequences of ion tilting during plasma etching with a three-dimensional feature profile simulator," *J. Vac. Sci. Technol. A*, vol. 35, no. 2, p. 021303, 2017.

[104] C. M. Huard, Y. Zhang, S. Sriraman, A. Paterson, and M. J. Kushner, "Role of neutral transport in aspect ratio dependent plasma etching of three-dimensional features," *J. Vac. Sci. Technol. A*, vol. 35, no. 5, p. 05C301, 2017.

[105] S. Huang, S. Shim, S. K. Nam, and M. J. Kushner, "Pattern dependent profile distortion during plasma etching of high aspect ratio features in sio2," *J. Vac. Sci. Technol. A*, vol. 38, no. 2, p. 023001, 2020.

[106] Y. G. Yook, H. S. You, J. H. Park, W. S. Chang, D. C. Kwon, J. S. Yoon, K. H. Yoon, S. S. Shin, D. H. Yu, and Y. H. Im, "Fast and realistic 3d feature profile simulation platform for plasma etching process," *J. Phys. D: Appl. Phys.*, vol. 55, no. 25, p. 255202, 2022.

[107] D. J. Dixit, S. O'Mullane, S. Sunkoju, A. Gottipati, E. R. Hosler, V. K. Kamineni, M. E. Preil, N. Keller, J. Race, G. R. Muthinti, and A. C. Diebold, "Sensitivity analysis and line edge roughness determination of 28-nm pitch silicon fins using Mueller matrix spectroscopic ellipsometry-based optical critical dimension metrology," *Journal of Micro/Nanolithography, MEMS, and MOEMS*, vol. 14, no. 3, p. 031208, 2015.

[108] T. A. Weber and F. H. Stillinger, "Dynamical branching during fluorination of the dimerized si(100) surface: A molecular dynamics study," *J. Chem. Phys.*, vol. 92, no. 10, pp. 6239–6245, 1990.

[109] S. Hamaguchi and H. Ohta, "Surface molecular dynamics of Si/SiO_2 reactive ion etching," *Vacuum*, vol. 66, pp. 189–195, 08 2002.

[110] S. Hamaguchi, H. Ohta, and H. Yamada, "On interatomic potential functions for molecular dynamics (MD) simulations of plasma-wall interactions," *J. Plasma Fusion Res. SERIES*, vol. 6, pp. 80–83, 2004.

[111] H. Yamada and S. Hamaguchi, "Molecular-dynamics simulations of organic polymer etching by hydrocarbon beams," *J. Appl. Phys.*, vol. 96, no. 11, pp. 6147–6152, 2004.

[112] M. Taguchi and S. Hamaguchi, "Molecular dynamics study on ar ion bombardment effects in amorphous SiO_2 deposition processes," *J. Appl. Phys*, vol. 100, no. 12, p. 123305, 2006.

[113] T. Kawase and S. Hamaguchi, "Molecular dynamics simulation analyses on injection angle dependence of sio2 sputtering yields by fluorocarbon beams," *Thin Solid Films*, vol. 515, no. 12, pp. 4883–4886, 2007. The Third International Symposium on Dry Process (DPS 2005).

[114] M. Taguchi and S. Hamaguchi, "Md simulations of amorphous sio_2 thin film formation in reactive sputtering deposition processes," *Thin Solid Films*, vol. 515, no. 12, pp. 4879–4882, 2007. The Third International Symposium on Dry Process (DPS 2005).

[115] E. J. C. Tinacba, T. Ito, K. Karahashi, M. Isobe, and S. Hamaguchi, "Molecular dynamics simulation for reactive ion etching of Si and SiO_2 by SF_5^+ ions," *J. Vac. Sci. Technol. B*, vol. 39, no. 4, p. 043203, 2021.

[116] N. A. Mauchamp and S. Hamaguchi, "Molecular dynamics simulation of si trench etching with sio2 hard masks," *J. Vac. Sci. Technol. A*, vol. 40, no. 5, p. 053004, 2022.

[117] C. M. D. Cagomoc, M. Isobe, E. A. Hudson, and S. Hamaguchi, "Molecular dynamics simulation of oxide-nitride bilayer etching with energetic fluorocarbon ions," *J. Vac. Sci. Technol. A.*, vol. 40, no. 6, p. 063006, 2022.

[118] K. Ishikawa, K. Karahashi, H. Tsuboi, K. Yanai, and M. Nakamura, "Transitional change to amorphous fluorinated carbon film deposition under energetic irradiation of mass-analyzed carbon monofluoride ions on silicon dioxide surfaces," *J. Vac. Sci. Technol. A.*, vol. 21, no. 4, pp. L1–L3, 2003.

[119] K. Karahashi, K. Yanai, K. Ishikawa, H. Tsuboi, K. Kurihara, and M. Nakamura, "Etching yield of SiO_2 irradiated by F^+, ${CF_x}^+$ (x=1,2,3) ion with energies from 250 to 2000 eV," *J. Vac. Sci. Technol. A*, vol. 22, no. 4, pp. 1166–1168, 2004.

[120] K. Yanai, K. Karahashi, K. Ishikawa, and M. Nakamura, "Mass-analyzed ${CF_x}^+$ (x=1,2,3) ion beam study on selectivity of SiO_2-to-SiN etching and a-C:F film deposition," *J. Appl. Phys.*, vol. 97, no. 5, p. 53302, 2005.

[121] T. Ito, K. Karahashi, M. Fukasawa, T. Tatsumi, and S. Hamaguchi, "Hydrogen effects in hydrofluorocarbon plasma etching of silicon nitride: Beam study with CF^+, ${CF_2}^+$, ${CHF_2}^+$, and CH_2F^+ ions," *J. Vac. Sci. Technol. A*, vol. 29, p. 050601, 7 2011.

[122] K. Karahashi, H. Li, K. Yamada, T. Ito, S. Numazawa, K. Machida, K. Ishikawa, and S. Hamaguchi, "Etching yields and surface reactions of amorphous carbon by fluorocarbon ion irradiation," *Jpn. J. Appl. Phys.*, vol. 56, p. 06HB09, may 2017.

[123] J. Biersack and L. Haggmark, "A monte carlo computer program for the transport of energetic ions in amorphous targets," *Nucl. Instrum. Methods*, vol. 174, no. 1, pp. 257–269, 1980.

[124] J. F. Ziegler and J. P. Biersack, *The Stopping and Range of Ions in Matter*, pp. 93–129. Boston, MA: Springer US, 1985.

[125] J. Biersack, S. Berg, and C. Nender, "T-dyn monte carlo simulations applied to ion assisted thin film processes," *Nucl. Instrum. Methods Phys. Res. B: Beam Interactions with Materials and Atoms*, vol. 59-60, pp. 21–27, 1991.

[126] J. F. Ziegler, *Handbook of Ion Implantation Technology.* Amsterdam: North-Holland, 1992.

[127] D. C. Rapaport, *The Art of Molecular Dynamics Simulation.* Cambridge University Press, 2nd ed., 2004.

[128] C. F. Abrams and D. B. Graves, "On the active surface layer in CF_x^+ etching of Si: Atomistic simulation and a simple mass balance model," *J. Vac. Sci. Technol. A*, vol. 18, no. 2, pp. 411–416, 2000.

[129] V. V. Smirnov, A. V. Stengach, K. G. Gaynullin, V. A. Pavlovsky, S. Rauf, P. Stout, and P. L. G. Ventzek, "Molecular-dynamics model of energetic fluorocarbon-ion bombardment on SiO_2. II. CF_x^+ (x=1, 2, 3) ion etch characterization," *J. Appl. Phys.*, vol. 97, p. 093303, 4 2005.

[130] S. Rauf, T. Sparks, P. L. G. Ventzek, V. V. Smirnov, A. V. Stengach, K. G. Gaynullin, and V. A. Pavlovsky, "A molecular dynamics investigation of fluorocarbon based layer-by-layer etching of silicon and SiO_2," *J. Appl. Phys.*, vol. 101, no. 3, p. 33308, 2007.

[131] L. Verlet, "Computer "Experiments" on Classical Fluids. I. Thermodynamical Properties of Lennard-Jones Molecules," *Phys. Rev.*, vol. 159, pp. 98–103, 7 1967.

[132] W. C. Swope, H. C. Andersen, P. H. Berens, and K. R. Wilson, "A computer simulation method for the calculation of equilibrium constants for the formation of physical clusters of molecules: Application to small water clusters," *J. Chem. Phys.*, vol. 76, no. 1, pp. 637–649, 1982.

[133] H. Toyoda, H. Morishima, R. Fukute, Y. Hori, I. Murakami, and H. Sugai, "Beam study of the Si and SiO_2 etching processes by energetic fluorocarbon ions," *J. Appl. Phys.*, vol. 95, pp. 5172–5179, 4 2004.

[134] *Bond Energies*, pp. 442–445. John Wiley & Sons, Ltd, 2006.

[135] T. Ito, K. Karahashi, S.-Y. Kang, and S. Hamaguchi, "Evaluation of si etching yields by cl^+ br^+ and hbr^+ ion irradiation," *J. Phys. Conf. Ser.*, vol. 232, p. 012021, jun 2010.

[136] S. Tachi and S. Okudaira, "Chemical sputtering of silicon by f+, cl+, and br+ ions: Reactive spot model for reactive ion etching," *J. Vac. Sci. Technol. B*, vol. 4, no. 2, pp. 459–467, 1986.

[137] Y. Kim, S. Lee, T. Jung, B. Lee, N. Kwak, and S. Park, "Challenges in high-aspect ratio contact (HARC) etching for DRAM capacitor formation," in *Advanced Etch Technology for Nanopatterning IV* (Q. Lin, S. U. Engelmann, and Y. Zhang, eds.), vol. 9428, pp. 9–14, International Society for Optics and Photonics, SPIE, 2015.

[138] S. Park, J. Lee, J. Jang, J. K. Lim, H. Kim, J. J. Shim, M. tai Yu, J.-K. Kang, S. J. Ahn, and J. Song, "Highly-reliable cell characteristics with 128-layer single-stack 3d-nand flash memory," in *2021 Symposium on VLSI Technology Digest of Technical Papers*, pp. T8–3, 2021.

[139] N. Ikegami, A. Yabata, T. Matsui, J. Kanamori, and Y. Horiike, "Characteristics of very high-aspect-ratio contact hole etching," *Jpn. J. Appl. Phys.*, vol. 36, pp. 2470–2476, Apr 1997.

[140] S. Huang, C. Huard, S. Shim, S. K. Nam, I.-C. Song, S. Lu, and M. J. Kushner, "Plasma etching of high aspect ratio features in sio2 using ar/c4f8/o2 mixtures: A computational investigation," *J. Vac. Sci. Technol. A.*, vol. 37, no. 3, p. 031304, 2019.

[141] A. Stukowski, "Visualization and analysis of atomistic simulation data with OVITO-the Open Visualization Tool," *Model. Simul. Mater. Sci. Eng.*, vol. 18, JAN 2010.

[142] S. Hamaguchi and M. Dalvie, "Intrinsic and passivation-induced trench tapering during plasma etching," *J. Electrochem. Soc.*, vol. 141, p. 1964, jul 1994.

Research Achievements

Publications

– Doctoral Degree –

- **C. M. D. Cagomoc**, M. Isobe, E. A. Hudson, and S. Hamaguchi, *Molecular Dynamics Simulation of Oxide-Nitride Bilayer Etching with Energetic Fluorocarbon Ions*, J. Vac. Sci. Technol. A **40** 063006 (2022).
- **C. M. D. Cagomoc**, M. Isobe, E. A. Hudson, and S. Hamaguchi, *Inert-gas Ion Scattering at Grazing Angle Incidence on Si and SiO_2 Surfaces*, J. Vac. Sci. Technol. A (2023). *to appear*
- **C. M. D. Cagomoc**, M. Isobe, and S. Hamaguchi, *Molecular Dynamics Study of SiO_2 Nano-hole Etching by Fluorocarbon Plasmas*, J. Vac. Sci. Technol. A (2023). *to appear*
- **C. M. D. Cagomoc**, S. Taira, M. Isobe, T. Ito, K. Karahashi, L. Belau, E. A. Hudson, and S. Hamaguchi, *Molecular Dynamics Simulation of Oxide and Nitride Etching by CF_3^+ and Cl^+*, (to be submitted).

– Master's Degree –

- **C. M. D. Cagomoc**, M. Isobe, and S. Hamaguchi, *Atomic-Scale Numerical Simulation of a Nanometer-Scale Hole Etching of SiO_2 with a Carbon Mask*, in the

proceedings of Japan Society of Applied Physics / Silicon Technology Subcommittee 215th Meeting, pp. 25-27 (2019).

– Bachelor's Degree –

- **C. M. D. Cagomoc**, M. J. D. De Leon, A. S. M. Ebuen, M. N. R. Gilos, and M. R. Vasquez Jr., *RF Plasma Cleaning of Silicon Substrates with High-Density Polyethylene Contamination*, Jpn. J. Appl. Phys. 57, 01AB04 1-5 (2017).
- **C. M. D. Cagomoc**, and M. R. Vasquez Jr., *Enhanced Chromium Adsorption Capacity via Plasma Modification of Natural Zeolites*, Jpn. J. Appl. Phys. 56, 01AF02 1–4 (2016).

Conferences (International and Local)

– Doctoral Degree –

- **C. M. D. Cagomoc**, S. Taira, M. Isobe, T. Ito, K. Karahashi, L. Belau, E. A. Hudson, and S. Hamaguchi, *Molecular Dynamics Simulation of Oxide and Nitride Etching by* CF_3^+ *and* Cl^+, American Vacuum Society 68th International Symposium & Exhibition, David L. Lawrence Convention Center, Pittsburgh, Pennsylvania, USA, November 2022.
- **C. M. D. Cagomoc**, M. Isobe, E. A. Hudson, and S. Hamaguchi, *Molecular Dynamics Simulation of Oxide-Nitride Stacked Layer Etching by Energetic Fluorocarbon Ions*, 65th Annual SVC Technical Conference, Long Beach Convention Center, Long Beach, California, USA, May 2-5, 2022.
- **C. M. D. Cagomoc**, M. Isobe, E. A. Hudson, and S. Hamaguchi, *Molecular Dynamics Simulation of Oxide-Nitride Layer Etching by Fluorocarbon Plasmas*, American Vacuum Society 67th Virtual Symposium, October 2021 (presented online).

- **C. M. D. Cagomoc**, M. Isobe, E. A. Hudson, and S. Hamaguchi, *Molecular Dynamics Study of Oxide-Nitride Etching by CF_3^+ Ions*, 82nd Japan Society of Applied Physics Autumn Meeting, September 2021 (presented online).

- **C. M. D. Cagomoc**, M. Isobe, E. A. Hudson, and S. Hamaguchi, *Molecular Dynamics Study of Ion Scattering on Silicon and Silicon Dioxide*, 23rd Symposium on Application of Plasma Process SAPP XXIII, February 2021 (presented online).

– Master's Degree –

- **C. M. D. Cagomoc**, M. Isobe and S. Hamaguchi, *Molecular Dynamics Simulation of SiO2 Etching with Fluorocarbon Ions and Radicals*, Joint Conference of XXXIV International Conference on Phenomena in Ionized Gases and the 10th International Conference on Reactive Plasmas, Hokkaido, Japan, July 2019.

- **C. M. D. Cagomoc**, M. Isobe and S. Hamaguchi, *Molecular Dynamics Simulation: Nanometer-scale Hole Etching of SiO2 with Carbon Mask*, 24th International Symposium on Plasma Chemistry, Naples, Italy, June 2019.

- **C. M. D. Cagomoc**, M. Isobe and S. Hamaguchi, *Molecular Dynamics Simulation of SiO_2 Etching by Energetic Fluorcarbon Ions*, 66th Japan Society of Applied Physics Spring Meeting, Tokyo, March 2019.

- **C. M. D. Cagomoc**, M. Isobe and S. Hamaguchi, *Atomic-Scale Numerical Simulation of a Nanometer-Scale Hole Etching of SiO_2 with a Carbon Mask*, Japan Society of Applied Physics / Silicon Technology Subcommittee 215th Meeting, Tokyo, February 2019. **[invited speaker]**

- **C. M. D. Cagomoc**, M. Isobe, K. Karahashi, T. Hirohashi, J. Hashimoto, M. Omura, H. Hayashi and S. Hamaguchi, *Molecular Dynamics Simulation of Nanometer-scale Hole Etching of SiO_2 with Carbon Masks*, 40th International Symposium on Dry Process, Nagoya, Japan, November 2018.

- **C. M. D. Cagomoc**, M. Isobe and S. Hamaguchi, *Atomic-Scale Numerical Simulation of a Nanometer-Scale Hole Etching of SiO_2 with a Carbon Mask*, 65th International Symposium Exhibition, California, USA, October 2018.

- **C. M. D. Cagomoc**, M. Isobe, K. Karahashi, T. Hirohashi, J. Hashimoto, M. Omura, H. Hayashi and S. Hamaguchi, *Molecular Dynamics Simulation of Hole Etching in SiO_2 by Energetic Fluorocarbon Ion Injection*, 79th Japan Society of Applied Physics Autumn Meeting, Nagoya, September 2018.

- **C. M. D. Cagomoc**, M. Isobe and S. Hamaguchi, *Molecular Dynamics Simulation of Nanometer-Scale Hole Etching*, 7th International Conference on Microelectronics and Plasma Technology, Incheon, South Korea, July 2018.

- **C. M. D. Cagomoc**, and M. R. Vasquez Jr., *Surface Conditioning via RF Plasma Irradiation of Natural Zeolite for Chromium Adsorption*, 10th EU-Japan Joint Symposium on Plasma Processing, Okinawa, Japan, December 2017.

– Bachelor's Degree –

- **C. M. D. Cagomoc**, and M. R. Vasquez Jr., *Enhanced Chromium Adsorption Capacity via Plasma Modification of Natural Zeolites*, 8th International Symposium on Advanced Plasma Science and its Application for Nitrides and Nanomaterials, Nagoya, Japan, March 2016.

- **C. M. D. Cagomoc**, and M. R. Vasquez Jr., *Plasma Modification of Natural Zeolite for Chromium Adsorption*, 1st International Symposium of the Vacuum Society of the Philippines, Quezon City, Philippines, January 2016.

Awards

– Doctoral Degree –

- **Finalist** of the **2022 Coburn and Winters (C&W) Student Award** in Plasma Science and Technology Division (PSTD) of the American Vacuum Society (AVS)
- **Recipient** of the **2022 Encouragement Prize** (second half) by the Association for the Advancement of Manufacturing & Technology
- **Recipient** of the **Student Sponsorship Program** by the Society of Vacuum Coaters (May 2022)
- **Recipient** of the Japan Society for the Promotion of Science (JSPS) Research Fellowship for Young Scientists (April 2020 – March 2023)
- **Recipient** of the Japanese Government Ministry of Education, Culture, Sports, Science and Technology (MEXT) Scholarship (declined)

– Master's Degree –

- **Recipient** of the **Best Poster Award** at the 7th International Conference on Microelectronics and Plasma Technology, Incheon, South Korea (July 2018)
- **Recipient** of the Japan International Cooperation Agency (JICA) Innovative Asia Scholarship (October 2017 – September 2019).